Force–distance curves by atomic force microscopy

B. Cappella, G. Dietler

Institut de Physique de la Matière Condersée, Université de Lausanne, CH-1015 Lausanne, Switzerland

ELSEVIER

Amsterdam–Lausanne–New York–Oxford–Shannon–Tokyo

Contents

ELSEVIER

Surface Science Reports 34 (1999) 1–104

surface science reports

www.elsevier.nl/locate/surfrep

Force–distance curves by atomic force microscopy

B. Cappella, G. Dietler

Institut de Physique de la Matière Condersée, Université de Lausanne, CH-1015 Lausanne, Switzerland

Abstract

Atomic force microscopy (AFM) force–distance curves have become a fundamental tool in several fields of research, such as surface science, materials engineering, biochemistry and biology. Furthermore, they have great importance for the study of surface interactions from a theoretical point of view.

Force–distance curves have been employed for the study of numerous materials properties and for the characterization of all the known kinds of surface forces. Since 1989, several techniques of acquisition and analysis have arisen. An increasing number of systems, presenting new kinds of forces, have been analyzed. AFM force–distance curves are routinely used in several kinds of measurement, for the determination of elasticity, Hamaker constants, surface charge densities, and degrees of hydrophobicity.

The present review is designed to indicate the theoretical background of AFM force–distance curves as well as to present the great variety of measurements that can be performed with this tool.

Section 1 is a general introduction to AFM force–distance curves. In Sections 2–4 the fundamentals of the theories concerning the three regions of force–distance curves are summarized. In particular, Section 2 contains a review of the techniques employed for the characterization of the elastic properties of materials. After an overview of calibration problems (Section 5), the different forces that can be measured with AFM force–distance curves are discussed. Capillary, Coulomb, Van der Waals, double-layer, solvation, hydration, hydrophobic, specific and steric forces are considered. For each force the available theoretical aspects necessary for the comprehension of the experiments are provided. The main experiments concerning the measurements of such forces are listed, pointing out the experimental problems, the artifacts that are likely to affect the measurement, and the main established results. Experiments up to June 1998 are reviewed. Finally, in Section 7, techniques to acquire force–distance curves sequentially and to draw bidimensional maps of different parameters are listed.

1. Introduction

1.1. General overview: AFM and force–distance curves

Since 1989, the atomic force microscope (AFM) [1] has emerged as a useful tool for studying surface interactions by means of force–distance curves. A great deal of work has been performed on both its theoretical and experimental aspects. The heart of the AFM is a cantilever with a microfabricated tip that deflects when interacting with the sample surface. Provided the sample can be scanned by means of a piezoactuator, the cantilever deflection may be measured in different ways in order to reproduce the sample topography. A controller regulates, collects, and processes the data, and drives the piezo

0167-5729/99/$ – see front matter
PII: S0167-5729(99)00003-5

scanner. The controller consists of a variable number of A/D converters that receive data from the detection system of cantilever deflections, some D/A converters that give signals to the piezo, and an interface with a computer that stores data.

AFM cantilevers are usually made out of silicon or silicon nitride. They have two shapes: rectangular and "V"-shaped. The cantilever back face (the face that is not in contact with the sample) is usually coated with a metallic thin layer (often gold) in order to enhance reflectivity. This is necessary in liquids, where the reflectivity of silicon nitride is much reduced.

The most common methods to detect cantilever deflections are the optical lever method, the interferometric method, and the electronic tunneling method. The optical lever method is the most used one, since it is the most simple to implement. It consists in focusing a laser beam on the back side of the cantilever and in detecting the reflected beam by means of a position sensor, that is usually a quartered photodiode. Both cantilever deflection and torsion signals may be collected. In the interferometric method, a laser beam focused on the cantilever interferes with a reference beam and the deflections are revealed by the variation of the interfering beam intensity. Finally, in the electronic tunneling method, the tunneling current between a metallic tip and the side of the cantilever that does not face the sample is revealed. Hence, the cantilever has to be conductive or coated with a conductive material. This method, employed in the early AFM, has several problems. First, the interactions with the metallic tip next to the cantilever are comparable to those with the sample. Furthermore this method does not work in liquids, and when used in air, contaminants accumulate between the cantilever and the tip, rendering the tunneling unstable.

The sample is scanned by means of a piezoactuator, that is able to perform minimal displacements of the order of 1 Å with high precision up to displacements of the order of 100 μm. The piezoelectric actuators employed for atomic force microscopy are cylindrical tubes of different dimensions with an inside electrode, usually grounded, and an outside electrode, usually segmented in four quadrants. Unfortunately, the dependence of the displacement of piezo on the applied voltage is hysteretic and affected by creep, that is a delay effect depending on temperature. Because of creep, almost the entire displacement is performed at the beginning, but a little fraction is done later with a logarithmic time dependence. Efforts to eliminate these non-linearities follow four different approaches:

1. *A posteriori* calculation of non-linear deformations due to hysteresis and creep [2].
2. Independent measurement of piezo displacements with two different techniques, e.g., *capacitive technique* (the two plates of a capacitor are mounted one on the piezo and the other fixed on the support and the displacements can be calculated on the basis of capacitance variations) [3,4] and *interferometric technique* (the displacement of the interference fringes between a laser beam reflected by the piezo and a reference beam is measured) [5,6].
3. Use of electrostrictive transducers [7].
4. *Charge-drive technique*, which consists in driving the piezo by controlling the charge instead of the potential [8]. This may be achieved by inserting a capacitor between the amplifier and the piezo [9, 10].

AFM is able to acquire force–distance curves on every kind of surface and in every kind of environment, with high lateral (25 nm) [11], vertical (0.1 Å) and force (1 pN) [12] resolution. The entire force–distance curve can be collected. Moreover, force measurements can be correlated with topography measurements. Interacting surfaces can be reduced to 10×10 nm. The AFM is the only

tool able to measure the interactions between nanometer sized surfaces, allowing local forces and sample properties to be compared.

When acquiring force–distance curves, the piezo must be ramped along the Z axis, i.e., the axis perpendicular to the surface. There are two principal modes of acquisition of force–distance curves. In the first mode, called the static mode, the sample is displaced along the Z axis in discrete steps and the variations in cantilever deflection are collected, as indicated in Section 1.2. In the second mode, called the non-contact mode, the cantilever is vibrated by an extra piezoelectric transducer while the sample is approached and withdrawn, and the amplitude or the resonance frequency of the cantilever oscillations are collected as a function of tip–sample distance. The principles of this mode of acquisition are introduced in Section 1.5.

The study of surface interactions can be performed with several other tools [13, 14]. Between all these tools the surface force apparatus (SFA), invented by Israelachvili [15] in 1978, is the leading instrument in surface force measurements. It contains two curved molecularly smooth surfaces of mica whose separation can be measured by use of interferometric techniques. The distance between the two surfaces is controlled by means of a piezoelectric tube and the force is measured by expanding or contracting the piezotube by a known amount while measuring optically the movement of the surfaces. Any difference between the two values, when multiplied by the stiffness of the spring separating the surfaces, gives the force difference between the initial and final position. Measurements may be carried out in liquid. The SFA has a vertical resolution of 0.1 nm and a force resolution of 10 nN [15]. The SFA employs only surfaces of known geometry, thus leading to precise measurements of surface forces and energies. Although there is a considerable overlap in the force measuring capabilities of the AFM and the SFA, we would like to point out several differences.

1. Interacting surfaces in AFM are 10^4–10^6 times smaller than those employed in SFA, but in AFM the shape of the surfaces is unknown.
2. When the substrates to be employed are not transparent, the interferometric technique cannot be used to measure forces (see Ref. [16]).
3. The SFA needs molecularly smooth samples, and therefore it can deal only with mica surfaces or thin layers of materials adsorbed on mica.
4. The SFA cannot characterize indentation or topography.
5. The viscous force on a spherical particle scales with the square of the particle radius. Therefore with an AFM, measurements can be performed at speeds 10^4 times greater while maintaining the same viscous force to surface force ratio [17].
6. Since the interacting surfaces are smaller, and the probability of trapping a contaminant particle is proportional to the square root of the interacting surfaces, the AFM is less subject to contamination [17].

The first study on force–distance curves acquired with an AFM, concerning the characterization of surface forces on LiF and graphite, dates back to 1988 [18]. The first works trying to interpret force–distance curves and related information appeared in 1989–1990. Since the first experiments, it has become clear that, when force–distance curves are acquired in air, meniscus forces exerted by thin layers of water vapor dominate any other interactions. Such forces can be eliminated by working in a controlled atmosphere or in a liquid environment.

In 1991 several studies of force–distance curves in liquids were performed, both theoretically and experimentally. Moreover, Mizes et al. [19] performed the first direct measurement of the spatial variation of adhesion.

Since then, two different research lines have characterized the research on force–distance curves: on one hand, the study of different interactions in several environments, on the other, the "mapping" of such interactions, drawn from force–distance curves, in order to distinguish materials with different physico-chemical properties (a kind of "surface spectroscopy").

In 1994, a further technique was introduced [20]. This technique employs functionalized tips, i.e., tips covered with particular molecules that selectively adhere to other, in order to study specific forces by means of force–distance curves.

1.2. Relation between AFM force–distance curves and tip–sample interaction force

An AFM force–distance curve is a plot of tip–sample interaction forces vs. tip–sample distance. In order to obtain such a plot, the sample (or the tip) is ramped along the vertical axis (Z axis) and the cantilever deflection δ_c is acquired. The tip–sample force is given by Hooke's law:

$$F = -k_c\delta_c. \tag{1.1}$$

The distance controlled during the measurement is not the actual tip–sample distance D (Fig. 1), but the distance Z between sample surface and the rest position of the cantilever. These two distances differ because of cantilever deflection δ_c and because of the sample deformation δ_s. These four quantities are related as follows:

$$D = Z - (\delta_c + \delta_s). \tag{1.2}$$

Since one does not know in advance the cantilever deflections and the sample deformations, the only distance that one can control is the Z distance, i.e., the displacement of the piezo. Therefore, the raw curve obtained by AFM should be called "force–displacement curve" rather than "force–distance curve". This latter term should be employed only for curves in which the force is plotted versus the true tip–sample distance, that has been previously calculated from raw data. Such a distinction is used in this review. When not referring to the specific type of plot employed, the term "force–distance curve" is used.

An AFM force–displacement curve does not reproduce tip–sample interactions, but is the result of two contributions: the tip–sample interaction $F(D)$ and the elastic force of the cantilever, Eq. (1.1). Such a result can be intuitively understood by means of the graphical construction shown in Fig. 2.

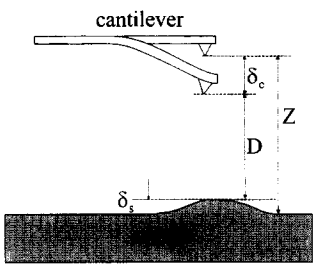

Fig. 1. The tip–sample system. D is the actual tip–sample distance, whereas Z is the distance between the sample and the cantilever rest position. These two distances differ because of the cantilever deflection δ_c and because of the sample deformation δ_s.

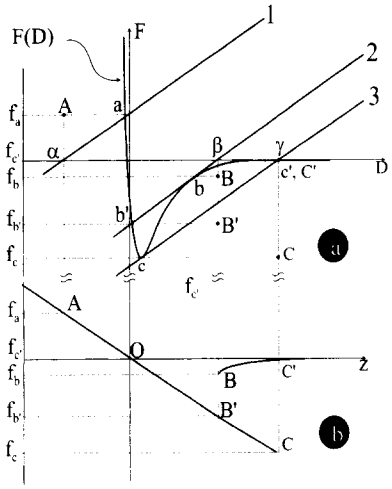

Fig. 2. Graphical construction of an AFM force–displacement curve. In panel (a) the curve $F(D)$ represents the tip–sample interaction and the lines 1, 2, and 3 represent the elastic force of the cantilever. At each distance the cantilever deflects until the elastic force equals the tip–sample force and the system is in equilibrium. The force values f_a, f_b, and f_c at equilibrium are given by the intersections a, b, and c between lines 1, 2, and 3 and the curve $F(D)$. These force values must be assigned to the distances Z between the sample and the cantilever rest positions, i.e., the distances α, β, and γ given by the intersections between lines 1, 2, and 3 and the horizontal axis. This graphical construction has to be made going both from right to left and from left to right. The result is shown in panel (b). The points A, B, B', C, and C' correspond to the points a, b, b', c, and c' respectively. BB' and CC' are two discontinuities. The origin O of axis in panel (b) is usually put at the intersection between the prolongation of the zero line and the contact line of the approach curve. The force $f_{c'}$ eventually coincides with the zero force.

In Fig. 2(a) the curve $F(D)$ represents the tip–sample interaction force. For the present, since no surface force has been introduced yet and for the sake of simplicity, $F(D)$ was chosen to be the interatomic Lennard–Jones force, i.e., $F(D) = -\mathbf{A}/D^7 + \mathbf{B}/D^{13}$. By expressing tip–sample forces by means of an interatomic Lennard-Jones force, only a simple qualitative description of the mechanisms involved in force–displacement curves acquisition can be provided. In particular, the attractive force between surfaces actually follows a force law $-D^{-n}$ with $n \leq 3$ (and not $n = 7$) and the repulsive part of the force is much more complex than the one modeled by the Lennard–Jones force. In Section 2 we treat this in detail. The lines 1–3 represent the elastic force of the cantilever, Eq. (1.1). In panel (b) of Fig. 2 the resulting AFM force–displacement curve is shown. At each distance the cantilever deflects until the elastic force of the cantilever equals the tip–sample interaction force, so that the system is in equilibrium. The force values at equilibrium f_a, f_b, f_c are given by the intersections a, b and c between lines 1–3 and the curve $F(D)$, respectively. These force values must not be assigned to the distances D at which the lines intersect the curve $F(D)$, but to the distances Z between the sample and the cantilever rest positions, that are the distances α, β, and γ given by the intersections between lines 1–3 and the horizontal axis (zero force axis). Going from right to left, i.e., approaching to the sample, the approach curve is obtained. Making the same graphical construction from left to right, i.e., withdrawing from the sample, gives the withdrawal curve. The result is shown in panel (b) of Fig. 2. The points A, B, B', C, and C' correspond to the points a, b, b', c, and c', respectively.

Let us now give an analytical expression for the force–displacement curves, following the derivation of Hao et al. [21]. The cantilever–sample system can be described by means of a potential U_{tot} that is

the sum of three potentials: $U_{cs}(D)$, $U_c(\delta_c)$, and $U_s(\delta_s)$. $U_{cs}(D)$ is the interaction potential between the tip and the sample, e.g., the Lennard-Jones potential. $U_c(\delta_c)$ is Hooke's elastic potential of the cantilever. $U_s(\delta_s)$ is the potential that describes the sample deformation. Sample deformations are discussed in detail in Section 2. For the present derivation, the sample deformation is described by the Hooke's law:

$$\begin{aligned} U_c(\delta_c) &= \tfrac{1}{2}k_c(\delta_c)^2, \\ U_s(\delta_s) &= \tfrac{1}{2}k_s(\delta_s)^2, \end{aligned} \tag{1.3}$$

in which k_c and k_s are the cantilever and sample elastic constants. Usually the interaction force can be written as

$$F = -\frac{\partial U_{cs}}{\partial D} = -\frac{C}{D^n}, \tag{1.4}$$

in which C and n depend on the type of forces acting between the tip and sample. The force expressed in Eq. (1.4) takes into account only the attractive part of the interaction, i.e., only the interaction prior to contact.

The relation between Z and δ_c can be obtained by forcing the system to be stationary:

$$\frac{\partial U_{tot}}{\partial(\delta_s)} = \frac{\partial U_{tot}}{\partial(\delta_c)} = 0. \tag{1.5}$$

Since $\partial U_{cs}/\partial(\delta_s) = -\partial U_{cs}/\partial(D)$ (see Eq. (1.2)), we obtain

$$\begin{aligned} \delta_s &= \frac{k_c}{k_s}\delta_c, \\ k_c\delta_c &= \frac{C}{(Z-\delta_c-\delta_s)^n}. \end{aligned} \tag{1.6}$$

Hence

$$k_c\delta_c = \frac{C}{(Z-\beta\delta_c)^n}, \tag{1.7}$$

in which $\beta = (1 + k_c/k_s)$. From Eqs. (1.6) and (1.7) both δ_s and Z can be determined from the measured value of δ_c as functions of the elastic constants k_c and k_s. Hence the measured force–displacement curve (panel (b), Fig. 2) can be converted into the force–distance curve (panel (a), Fig. 2), subject to the assumptions embodied in Eqs. (1.3) and (1.4).

1.3. Differences between approach and withdrawal curve

In panel (b) of Fig. 2 two characteristic features of force–displacement curves can be noted: the discontinuities BB' and CC' and the hysteresis between approach and withdrawal curve. These features are due to the fact that in the region between b' and c' (panel (a), Fig. 2) each line has three intersections and hence three equilibrium positions. Two of these positions (between c' and b and between b' and c) are stable, while the third position (between c and b) is unstable. During the approach phase, the tip follows the trajectory from c' to b and then "jumps" from b to b' (i.e., from the force value f_b to $f_{b'}$).

During retraction, the tip follows the trajectory from b' to c and then jumps from c to c' (i.e., from f_c to $f_{c'}$). These jumps correspond to the discontinuities BB' and CC' in panel (b) of Fig. 2, respectively. Thus, the region between b and c is not sampled. The difference in path between approach and withdrawal curves is usually called "force–displacement curve hysteresis". The two discontinuities in force values are called "jump-to-contact" in the approach curve (BB' in panel (b) of Fig. 2) and "jump-off-contact" in the withdrawal curve (CC' in panel (b) of Fig. 2).

Let us return to Eq. (1.5), that is the condition for U_{tot} to be stationary. For the system to be in stable equilibrium, we must have $\partial^2 U_{tot}/\partial(\delta_c)^2 > 0$, i.e.,

$$\frac{k_c}{\beta} > nC\frac{1}{(Z-\beta\delta_c)^{n-1}}, \tag{1.8}$$

in which k_c/β is referred to as the effective elastic constant.

If the force gradient is larger than the effective elastic constant, the cantilever becomes unstable and "jumps" onto the surface. This is the jump-to-contact discontinuity. From Eqs. (1.7) and (1.8) the cantilever deflection $(\delta_c)_{jtc}$ and the tip–sample distance D_{jtc} at which the jump-to-contact occurs can be determined:

$$(\delta_c)_{jtc} = \sqrt[n+1]{\frac{C}{(n\beta)^n k_c}}, \tag{1.9}$$

$$D_{jtc} = \beta n(\delta_c)_{jtc}.$$

These are the deflection and the distance of the point b in panel (a) of Fig. 2 and depend only on the attractive part of the interaction, Eq. (1.4). Since the repulsive part of the interaction has not been modeled yet, it is not possible to give the deflection and the distance of the point b' in the same figure. From Eq. (1.9) it is possible to calculate C and β once $(\delta_c)_{jtc}$ and D_{jtc} are known. These equations are valid for any kind of attractive force and are adapted to the two main attractive forces, i.e., Van der Waals and hydrophobic (see Sections 6.2 and 6.6). No similar expression can be found for the jump-off-contact, since, in this case, sample deformations and contact elastic theories reviewed in Section 2 actually determine both the distance and the force.

The slope of the lines 1–3 in panel (a) of Fig. 2 is the elastic constant of the cantilever k_c. Therefore, using cantilevers with high k_c, the unsampled stretch b–c becomes smaller, the jump-to-contact first increases with k_c and then, for high k_c, disappears. The jump-off-contact always decreases, so that the total hysteresis diminishes with k_c. When k_c is greater than the greatest value of the tip–sample force gradient, hysteresis and jumps disappear and the entire curve is sampled. Fig. 3 shows the force–displacement curves that would be obtained with three different cantilevers of $k_{c1} = 0.105\,\mathrm{N/m}$, $k_{c2} = 0.06\,\mathrm{N/m}$, and $k_{c3} = 0.04\,\mathrm{N/m}$ and with an interatomic Lennard-Jones force ($\mathbf{A} = 10^{-77}\,\mathrm{Jm^6}$, $\mathbf{B} = 10^{-134}\,\mathrm{Jm^{12}}$). Once again, since a Lennard-Jones interaction is used, the presented dependence has only a qualitative meaning. The hysteresis is large for k_{c3}, decreases for k_{c2}, and finally the jumps overlap in the curve acquired with k_{c1}.

Fig. 4 shows the dependence of jump-to-contact distance and jump-off-contact distance on the elastic constant of the cantilever, and Fig. 5 shows the same dependence for the jump-to-contact and the jump-off-contact forces. Both graphs have been obtained using a Lennard-Jones interaction with $\mathbf{A} = 10^{-77}\,\mathrm{Jm^6}$, $\mathbf{B} = 10^{-134}\,\mathrm{Jm^{12}}$.

In order to obtain complete force–displacement curves one should employ stiff cantilevers which, on the other hand, have a reduced force resolution. Therefore it is necessary to reach a compromise. In

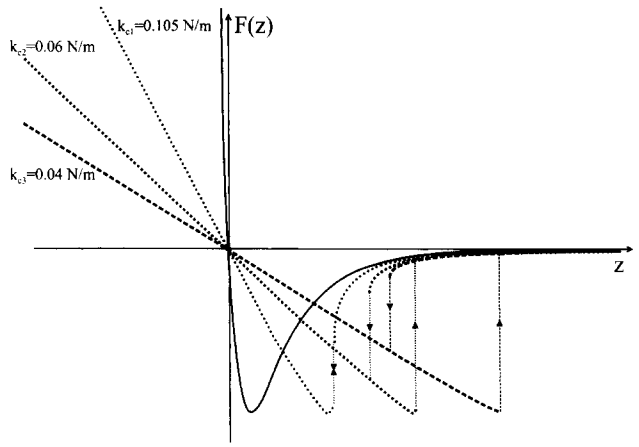

Fig. 3. Force–displacement curves (broken lines) obtained with three cantilevers of different elastic constant for $k_c \gg k_s$. The continuous line is the tip–sample interaction, modeled with a Lennard-Jones interaction with $\mathbf{A} = 10^{-77}$ Jm^6, $\mathbf{B} = 10^{-134}$ Jm^{12}.

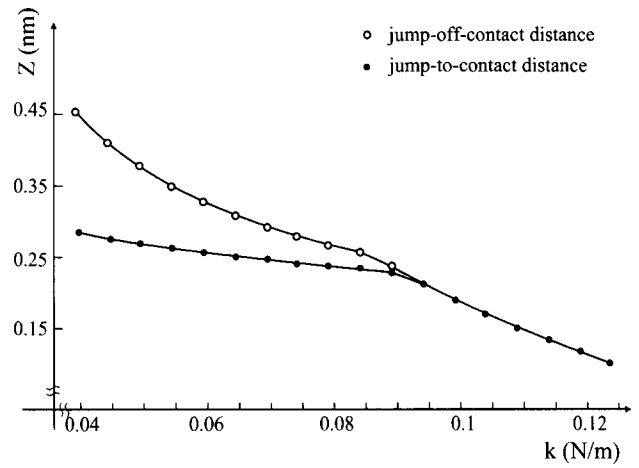

Fig. 4. Dependence of jump-to-contact and jump-off-contact distances on the elastic constant of the cantilever. The tip–sample interaction has been modeled with a Lennard-Jones interaction with $\mathbf{A} = 10^{-77}$ Jm^6, $\mathbf{B} = 10^{-134}$ Jm^{12}.

early AFMs, the cantilevers used for force–displacement curves measurements were tungsten wires, curved at one end, with high elastic constants (> 1 N/m) and with large radii of curvature (> 100 nm). The achieved force resolution was usually of the order of hundreds of pN so that the details of the tip–sample interaction could hardly be seen. Later, less stiff cantilevers with smaller radii of curvature have been employed, increasing the resolution up to nearly 10 pN.

Recently Aoki et al. [12] proved that the force resolution of the AFM can be increased to 0.1 pN. They employed home-made cantilevers with a spring constant of the order of 10^{-4} N/m. Such flexible cantilevers undergo large brownian motions and hence need to be stabilized by feedback forces. In this case, the feedback force is exerted by means of laser radiation pressure. Besides a first laser beam aimed to the deflections detection, a second laser beam is focused on the cantilever. The intensity of this

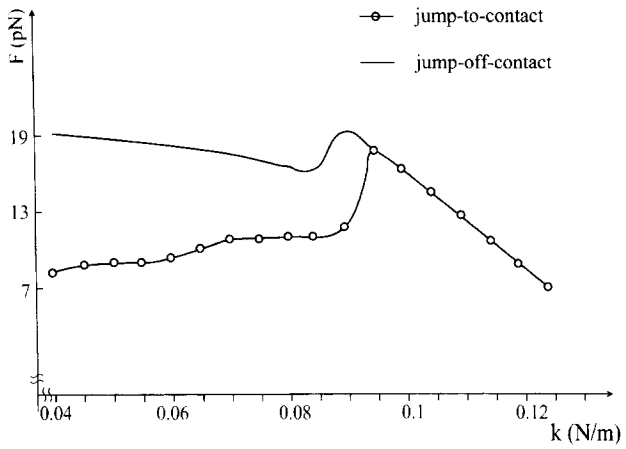

Fig. 5. Dependence of jump-to-contact and jump-off-contact forces on the elastic constant of the cantilever. The tip–sample interaction has been modeled with a Lennard-Jones interaction with $\mathbf{A} = 10^{-77}$ Jm^6, $\mathbf{B} = 10^{-134}$ Jm^{12}.

second laser beam is varied with a fast feedback loop, in order to keep constant the deflection of the cantilever.

1.4. The three regions of the force–displacement curve

Both approach and withdrawal force–displacement curves can be roughly divided in three regions: the contact line, the non-contact region and the zero line.

Zero lines are obtained when the tip is far apart from the sample and the cantilever deflection is nearly zero (on the right side of the point C' for both curves in Fig. 2). When working in liquid, these lines give information on the viscosity of the liquid.

When the sample is pressed against the cantilever the tip is in contact with the sample and $D = 0$. Therefore, from Eqs. (1.2) and (1.6), the relation between Z and δ_c can be obtained:

$$k_c\delta_c = \frac{k_c k_s}{k_c + k_s} Z. \tag{1.10}$$

The corresponding lines obtained in the force–displacement curve are called "contact lines". In panel (b) of Fig. 2 they are represented by the lines $B'A$ and CA. If the sample is much stiffer than the cantilever, the cantilever deflection δ_c equals sample movement Z, whereas if $k_s \ll k_c$, $\delta_c \cong (k_s/k_c)Z$. Thus, the contact lines provide information on sample stiffness.

The origin of force–displacement curves O is usually put at the intersection between the prolongation of the zero line and the contact line of the approach curve. Referring to panel (b) of Fig. 2, the distances $O\beta$ and $O\gamma$ are called "jump-to-contact distance" and "jump-off-contact distance". The adhesion work equals the area between the negative part of the withdrawal curve and the Z axis. The hysteresis of the curve is the difference between the adhesion work and the area between the negative part of the approach curve and the Z axis.

The most interesting regions of force–displacement curves are the two non-contact regions, containing the jump-to-contact and the jump-off-contact. The non-contact region in the approach

curves gives information about attractive or repulsive forces before contact. In particular, the maximum value of the attractive force sampled prior to contact equals the pull-on force, i.e., the product of jump-to-contact cantilever deflection and k_c.

The non-contact region in withdrawal curves contains the jump-off-contact. The pull-off force, i.e., the product of jump-off-contact cantilever deflection and k_c, equals the adhesion force, F_{ad}. In order to relate the tip and sample surface energies (γ_t and γ_s) and the adhesion force it is necessary to evaluate the deformations and the contact area of the sample. This can be done by means of different theories, reviewed in Section 2.

1.5. Non-contact mode

The non-contact mode was introduced by Martin et al. [22]. It consists of exciting the cantilever at a frequency $\nu = \omega/2\pi$ while the sample is ramped along the Z axis. The cantilever may be modeled as a harmonic oscillator with effective mass m^* and spring constant k_c. The effective mass m^* is given by $m^* = m_c + 0.24m_t$, where m_c is the mass of the cantilever and m_t is the mass of the tip. Hence, when the tip is far away from the surface, the equation of motion of the cantilever is

$$m^* \frac{d^2\delta_c(t)}{dt^2} + \gamma \frac{d\delta_c(t)}{dt} + k_c\delta_c(t) = F_0 \exp(i\omega t), \tag{1.11}$$

in which γ is the damping coefficient and $F_0 \exp(i\omega t)$ is the exciting force exerted by the driving piezo on the cantilever. Solving (1.11), the "free" amplitude of vibration as a function of frequency is obtained:

$$A(\omega) = \delta_c(t)\exp[-i(\omega t + \phi)] = \frac{F_0}{\gamma\omega_0} \frac{\omega_0/\omega}{\sqrt{1 + Q_0^2[(\omega/\omega_0) - (\omega_0/\omega)]^2}}, \tag{1.12}$$

in which $\omega_0 = \sqrt{k_c/m^*}$ is the resonance frequency and $Q_0 = m^*\omega_0/\gamma$ is the quality factor. When the cantilever is near the sample surface, surface forces modify the cantilever vibration and the force $F[D + \delta_c(t)]$, where D is the distance between the sample and the mean position of the cantilever, is to be added in the second term of Eq. (1.11). The general solution of such an equation cannot be obtained analytically, even when the force law is known. A convenient approximation is the small amplitude approximation, in which the surface force can be written in the form (we follow the derivation by Fontaine et al. [23]):

$$F[D + \delta_c(t)] = F(D) + \frac{dF}{dD}\delta_c(t). \tag{1.13}$$

Using such an approximation, Eq. (1.12) becomes

$$A(\omega, D) = \frac{F_0}{\gamma\omega_0} \frac{\omega_0'(D)/\omega}{\sqrt{1 + Q(D)^2[(\omega/\omega_0'(D)) - (\omega_0'(D)/\omega)]^2}}, \tag{1.14}$$

with

$$\omega_0'(D) = \omega_0\sqrt{1 - \frac{1}{k_c}\frac{dF}{dD}(D)} \quad \text{and} \quad Q(D) = Q_0\frac{\omega_0'(D)}{\omega_0}. \tag{1.15}$$

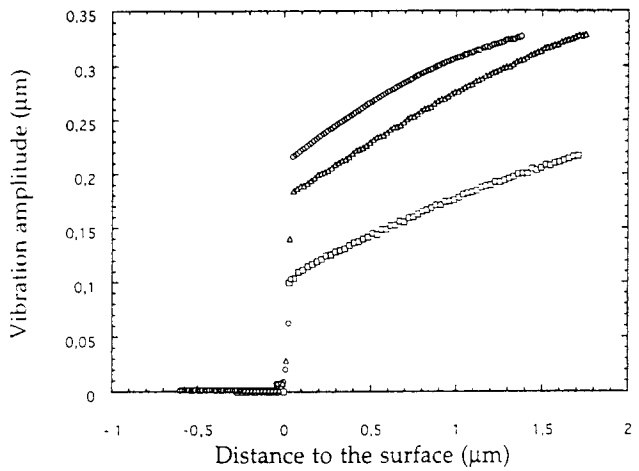

Fig. 6. Approach curves in the dynamic mode (operating frequency 328 kHz). Circles correspond to a Teflon surface and triangles to a gold surface. The squares correspond to mica and the vibration amplitude has been multiplied by 10 for the sake of comparison (reprinted with permission from [23]).

Dynamic force–distance curves are characterized by a horizontal line at the free amplitude, and a contact line at zero amplitude (when the cantilever is in contact with the sample it is no more longer to vibrate), with a region of decreasing amplitude in between, as shown in Fig. 6.

Non-contact force–distance curves are much less used than static force–distance curves. It is difficult to obtain a good quality factor in liquids. Furthermore, measurements are affected by a lot of artifacts (see Ref. [23]). Hence, in the following, only few experiments performed in this mode are presented.

2. Theories of contact region

From the contact lines of force–displacement curves it is possible to draw information about the elasto-plastic behavior of materials.

Let us first consider an ideally elastic material. As shown in panel (a) of Fig. 7, during the approach curve, i.e., from O to A, the tip goes into the sample of a depth δ, causing a deformation. During the withdrawal the tip goes back from A to O, and since the sample is elastic, it regains step by step its own shape, exerting on the tip the same force. Hence loading and unloading curves, i.e., the approach and withdrawal contact lines, overlap.

If the sample is ideally plastic (panel (b) of Fig. 7), it undergoes a deformation during the loading curve, and when the tip is withdrawn, it does not regain its own shape and the load decreases, whereas the penetration depth stays the same.

Most samples have a mixed behavior. Hence loading and unloading curves seldom overlap. In particular, at a given penetration depth, the force of the unloading curve is lesser than the force of the loading curve (see panel (c) of Fig. 7, where a force–displacement curve is shown, whereas the curves in panels (a) and (b) of Fig. 7 are deformation vs. load curves). The difference between the approach and the withdrawal contact lines is called "loading–unloading hysteresis".

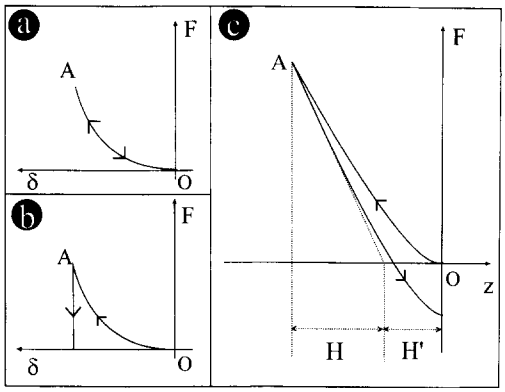

Fig. 7. Load vs. penetration depth curves for an ideally elastic material (panel (a)) and an ideally plastic material (panel (b)). The force–displacement curve for an elasto-plastic material is shown in panel (c). H' is the "zero load plastic indentation", i.e., the penetration depth at which the force of the unloading curve equals zero. H is the "zero load elastic deformation", i.e., the distance the sample regains.

The penetration depth H' at which the force of the unloading curve equals zero is called "zero load plastic indentation". The distance H the sample regains is the "zero load elastic deformation". Both distances are determined by use of the tangent to the curve in A, in order to neglect the influence of the variations of contact area during the unloading process.

In the following we neglect the plastic deformations and review the theories dealing with elastic continuum contact mechanics, in which the tip and sample are assumed to be continuous elastic media. The geometry of a spherical tip in contact with a flat surface is indicated schematically in Fig. 8. Eq. (1.10) reveals that, along the contact lines, Z and δ_c are proportional and that once the elastic constant of the cantilever is known, the elastic constant of the sample k_s can be determined from their proportionality ratio. The elastic constant of the sample k_s depends on contact area, Young modulus E and Poisson ratio ν via

$$k_s = 2a\frac{E}{1-\nu^2}, \tag{2.1}$$

in which a is the contact radius [24].

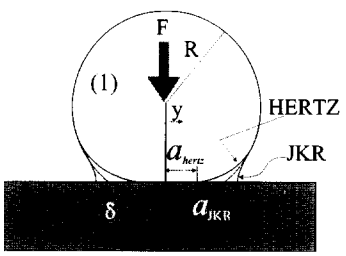

Fig. 8. Deformation of an elastic sphere on a flat surface following Hertz and JKR theory. The profile of the spherical tip in the DMT theory is the same as in the Hertz theory. F is the loading force, R the radius of the sphere, y the distance from the center of the contact area, δ the penetration depth, a_{Hertz} and a_{JKR} are the contact radius following the Hertz and the JKR theories.

In order to know the dependence of the contact radius and the force on the penetration depth it is necessary to make some assumptions. The different theories of such phenomena are summarized below.

2.1. Hertz and Sneddon

Hertz theory [25] dates back to 1881. It takes into account neither surface forces nor adhesion. The tip is considered as a smooth elastic sphere, while the sample is a rigid flat surface. For a sphere of radius R pressed onto a flat surface with a force F, the adhesion or pull-off force F_{ad}, the contact radius a, the contact radius at zero load a_0, the deformation δ of the spherical tip, and the pressure P are given by

$$F_{ad} = 0, \tag{2.2a}$$

$$a = \sqrt[3]{\frac{RF}{K}}, \tag{2.2b}$$

$$a_0 = 0, \tag{2.2c}$$

$$\delta = \frac{a^2}{R} = \frac{F}{Ka}, \tag{2.2d}$$

and

$$P(x) = \frac{3Ka\sqrt{1-x^2}}{2\pi R} = \frac{3F\sqrt{1-x^2}}{2\pi a^2}, \tag{2.2e}$$

in which $x = y/a$, y is the distance from the center of the contact circle, and the reduced Young modulus K is given by

$$\frac{1}{K} = \frac{3}{4}\left(\frac{1-\nu^2}{\mathrm{E}} + \frac{1-\nu_i^2}{\mathrm{E}_i}\right) \tag{2.3}$$

In Eq. (2.3) E, E_i, ν and ν_i are the Young modulus and the Poisson ratios of the flat surface, i.e., the sample, and of the indenter, i.e., the tip. The geometry of the deformed sphere–substrate contact is indicated in Fig. 8.

In the limit of high loads or low surface forces, an AFM experiment can follow the Hertz theory. In most cases, however, the AFM tip is stiffer than the sample, and one has to consider the deformations of the flat sample, or in other cases, those of both the tip and the sample. Hertz theory cannot be used to calculate sample deformations by assuming a rigid tip. When a rigid spherical punch on an elastic surface is considered, Sneddon analysis has to be employed [26]. In Sneddon analysis [27] the elastic deformation is given by a transcendental equation that can be computed numerically. The force F exerted by the punch on the surface and the surface deformation δ are given by

$$F = \frac{3}{8}K\left[(a^2+R^2)\ln\left(\frac{R+a}{R-a}\right) - 2aR\right], \tag{2.4a}$$

and

$$\delta = \frac{1}{2}a\ln\left(\frac{R+a}{R-a}\right). \tag{2.4b}$$

Deformation and force can be computed for a generic axisymmetric punch:

$$\delta = \int_0^1 \frac{f'(x)}{\sqrt{1-x^2}}\,dx, \tag{2.5a}$$

and

$$F = \frac{3}{2}Ka\int_0^1 \frac{x^2 f'(x)}{\sqrt{1-x^2}}\,dx, \tag{2.5b}$$

in which $f(x)$ is the function describing the profile of the punch. Solutions for common geometries can be found in [27].

Simply summing Hertz and Sneddon deformations, i.e., tip and sample deformations, whenever surface forces are negligible, one can obtain the total deformation in an AFM measurement. When surface forces must be considered, one of the four theories described in Sections 2.2 and 2.3 has to be employed.

2.2. Bradley, Derjaguin–Müller–Toporov and Johnson–Kendall–Roberts

We present here three theories that take into account the effect of surface energy on the contact deformation. The Bradley analysis [28] considers two rigid spheres interacting via a Lennard-Jones potential. The total force between the spheres is

$$F(z) = \frac{8\pi \mathrm{W} R}{3}\left[\frac{1}{4}\left(\frac{z}{z_0}\right)^{-8} - \left(\frac{z}{z_0}\right)^{-3}\right], \tag{2.6}$$

in which z_0 is the equilibrium separation, R the reduced radius of the spheres, i.e., $R = (1/R_1 + 1/R_2)^{-1}$, and W is the adhesion work at contact.

In Derjaguin–Müller–Toporov (DMT) theory [29] the elastic sphere is deformed according to Hertz theory, but in addition to the external load F, also the forces acting between the two bodies outside the contact region are taken into account. These forces alone produce a finite area of contact. If an external load is applied, the area of contact is increased. If a negative load is applied, the contact area diminishes until it reaches zero. At this point the pull-off force reaches its maximum value. The corresponding expressions for the quantities of Eqs. (2.2a)–(2.2e) are found by minimizing the sum of the elastic and of the surface energy:

$$F_{\mathrm{ad}} = 2\pi R\mathrm{W}, \tag{2.7a}$$

$$a = \sqrt[3]{(F + 2\pi R\mathrm{W})\frac{R}{K}}, \tag{2.7b}$$

$$a_0 = \sqrt[3]{\frac{2\pi \mathrm{W}}{K}R^2}, \tag{2.7c}$$

$$\delta = \frac{a^2}{R}, \tag{2.7d}$$

and

$$P(x) = \frac{3Ka\sqrt{1-x^2}}{2\pi R} = \frac{3F\sqrt{1-x^2}}{2\pi a^2}. \tag{2.7e}$$

DMT theory is applicable for systems with low adhesion and small tip radii.

Johnson–Kendall–Roberts (JKR) theory [30] neglects long range forces outside the contact area and considers only short range forces inside the contact region. With JKR assumptions, the corresponding equations of Eqs. (2.2a)–(2.2e) are:

$$F_{ad} = \frac{3}{2}\pi R\mathrm{W}, \tag{2.8a}$$

$$a = \sqrt[3]{\frac{R}{K}\left[F + 3\pi R\mathrm{W} + \sqrt{6\pi R\mathrm{W}F + (3\pi R\mathrm{W})^2}\right]}, \tag{2.8b}$$

$$a_0 = \sqrt[3]{\frac{6\pi R^2\mathrm{W}}{K}}, \tag{2.8c}$$

$$\delta = \frac{a^2}{R} - \frac{2}{3}\sqrt{\frac{6\pi \mathrm{W}a}{K}}, \tag{2.8d}$$

and

$$P(x) = \frac{3Ka}{2\pi R}\sqrt{1-x^2} - \sqrt{\frac{3K\mathrm{W}}{2\pi a}}\frac{1}{\sqrt{1-x^2}}. \tag{2.8e}$$

The JKR theory behaves hysteretically. During unloading, a neck links the tip and sample (see Fig. 8), and contact is abruptly ruptured at negative loads. When separation occurs, the contact radius has fallen to $a_s = 0.63a_0$.

The JKR theory is suitable for highly adhesive systems with low stiffness and large tip radii. One difficulty with the JKR theory is that it predicts an infinite stress for $x = 1$, i.e., at the edge of the contact area. This unphysical situation arises because JKR theory considers only the forces inside the contact area and implicitly assumes that the attractive forces act over an infinitesimally small range. These infinities disappear as soon as a finite range force law, e.g., Lennard-Jones potential, is assumed.

DMT and JKR theories have raised a number of controversial experimental as well as theoretical issues after their publication. This controversy persisted from 1971 to 1984, when it was slowly realized that the two theories apply to two very different situations. Without citing the numerous publications on the controversy, we indicate here the most important works.

Attard and Parker [31] self-consistently calculated the elastic deformation and adhesion of two convex bodies interacting via finite range surface forces, namely an exponential law for repulsive force at small separations and a 9–3 Lennard-Jones law for the attractive forces. Hertz theory is confirmed to be suitable for short ranged repulsive forces and large loads, and thus agrees well with the results of Attard and Parker for both exponential repulsive forces and Lennard-Jones repulsion. Nevertheless, in general, Hertz theory overestimates the deformation caused by a given load. When the adhesive part of the Lennard-Jones potential is considered, JKR theory turns out to predict the force–deformation

relation very well and also the stress infinities at $x = 1$ disappear. Comparing the pull-off force with the value predicted by JKR theory, when a certain parameter σ_A, which is a function of surface energies, radii of curvature and materials stiffness, is much lesser than one, i.e., for stiff bodies with small surface energies and small radii of curvature, DMT value is more accurate than JKR value.

Müller et al. [32] presented a self-consistent numerical calculation abandoning the hypothesis that adhesion forces do not alter the hertzian geometry. The result is a continuous transition from the DMT to the JKR theory when a single μ_M parameter is varied.

Pashley et al. [33] had already introduced a parameter φ_P, which is proportional to the ratio of h, i.e., the height of the neck formed when the sphere is under a negative load before detachment, and z_0, i.e., a typical atomic dimension:

$$\varphi_P = \frac{h}{z_0} \cong \sqrt[3]{\frac{RW^2}{K^2 z_0^3}}. \tag{2.9}$$

When $\varphi_P < 1$, i.e., $h < z_0$, surface forces outside the contact area become important and the behavior approaches that of the DMT theory. Following the more complete analysis of Müller et al. [32] the DMT model holds when $\varphi_P < 0.3$ (hard solids of small radius and low surface energies) and the JKR model holds when $\varphi_P > 3$ (soft bodies with large radius and surface energies).

2.3. Maugis

Maugis theory [34] is the most complete and accurate theory in that it applies to all materials, from large rigid spheres with high surface energies to small compliant bodies with low surface energies. The full range of material properties is described by a dimensionless parameter λ given by

$$\lambda = \frac{2.06}{z_0} \sqrt[3]{\frac{RW^2}{\pi K^2}}, \tag{2.10}$$

in which z_0 is again a typical atomic dimension. This parameter λ is proportional to the parameter μ_M introduced by Müller et al. [32] ($\lambda = 0.4\,\mu_M$), to the parameter φ_P introduced by Pashley, and to the parameter σ_A introduced by Attard and Parker [31] ($\lambda \cong 0.4\sqrt[3]{\sigma_A^2}$). A complete conversion table is given by Greenwood [35]. A large λ occurs for more compliant, large, and adhesive bodies, whereas a small λ occurs for small rigid materials with low surface energies.

In the Maugis theory following the Dugdale model [36], adhesion is considered as a constant additional stress over an annular region around the contact area. The ratio of the width of the annular region c to the contact radius a is denoted by m. By introducing the dimensionless parameters

$$\bar{A} = \frac{a}{\sqrt[3]{\pi W R^2/K}}, \tag{2.11a}$$

$$\bar{F} = \frac{F}{\pi W R}, \tag{2.11b}$$

and

$$\bar{\delta} = \frac{\delta}{\sqrt[3]{\pi^2 W^2 R/K^2}}, \tag{2.11c}$$

a set of parametric equations is obtained. In particular, the corresponding equations to Eqs. (2.2a) and (2.2d) are:

$$\bar{\delta} = \bar{A}^2 - \frac{4}{3}\bar{A}\lambda\sqrt{m^2-1}, \tag{2.12}$$

$$\frac{\lambda\bar{A}^2}{2}\left[\sqrt{m^2-1} + (m^2-2)\operatorname{arctg}\sqrt{m^2-1}\right] + \frac{4\lambda^2\bar{A}}{3}\left[-m+1+\sqrt{m^2-1}\operatorname{arctg}\sqrt{m^2-1}\right] = 1, \tag{2.13}$$

and

$$\bar{F} = \bar{A}^3 - \lambda\bar{A}^2\left(\sqrt{m^2-1} + m^2\operatorname{arctg}\sqrt{m^2-1}\right). \tag{2.14}$$

Eqs. (2.12)–(2.14) form an equation system which enables the calculation of m, F and $\bar{\delta}(\bar{A})$ if $\bar{A}(\bar{\delta})$ is given. Eq. (2.12) reduces to Eq. (2.7d) for $\lambda \to 0$ (DMT) and to Eq. (2.8d) for $\lambda \to \infty$ (JKR).

The adhesion force F_{ad} given by Eq. (2.14) is $2\pi R$W for $\lambda \to 0$ (DMT) and $1.5\pi R$W for $\lambda \to \infty$ (JKR).

The results presented above are displayed in Fig. 9, showing the dependence of $\bar{A}$ on $\bar{\delta}$ and the dependence of $\bar{F}$ on $\bar{\delta}$. In panel (a) it is evident that the radius of contact at zero penetration is zero only

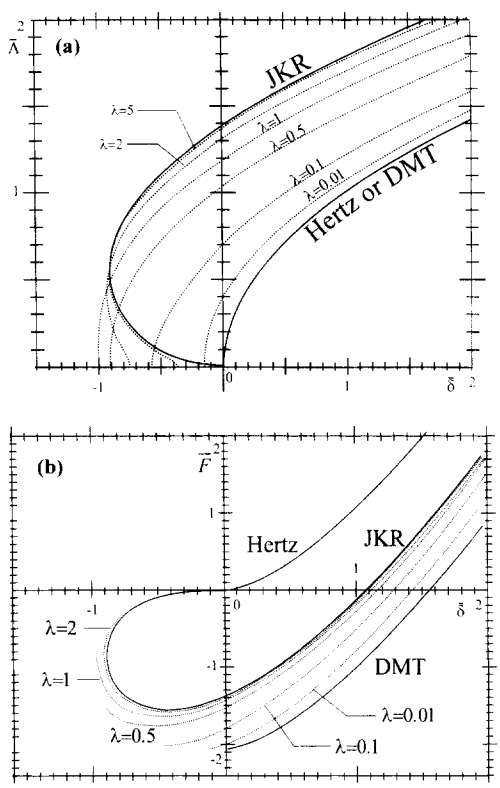

Fig. 9. The dependence of $\bar{A}$ on $\bar{\delta}$ (panel (a)) and the dependence of $\bar{F}$ on $\bar{\delta}$ (panel (b)) as functionals of λ calculated using Maugis theory. The JKR [30] and the DMT [29] limits are indicated. $\bar{A}$, $\bar{F}$, and $\bar{\delta}$ are the dimensionless contact radius, force and penetration depth given by Eqs. (2.11a)–(2.11c).

in the DMT limit. For $\lambda > 1$ and $\delta < 0$, there are two values of $\bar{A}$ (panel (a)) and of $\bar{F}$ (panel (b)) for each δ and the behavior is hysteretic.

Following Maugis theory, there is a continuous transition from the DMT deformation vs. load curve to the JKR deformation vs. load curve. This means that, at a certain applied load F, the deformation of the sample and the contact area, and hence the relation between k_s and E (see Eq. (2.1)) can be exactly known only if the surface energy, the tip shape and the stiffness of the sample are exactly known. In other words, provided the exact value of the elastic constant of the cantilever, for each value of load, one can calculate k_s from load/unloading curves, but in order to relate k_s to Young modulus E, one needs to know the contact radius a and hence the deformations δ of the sample. This is not possible as the deformation depends also on surface energies, and when deducing surface energies from pull-off forces, one has also to know the Young modulus E, i.e., the quantity one wants to draw from the experiments. Quite exact values of E can be obtained only when the materials or the experimental conditions approach the Hertz–Sneddon limit, and hence the measure of the Young modulus is usually obtained from the high load part of the load curve in order to exclude the influence of surface energies. Furthermore, in AFM measurements, E, R, and W are the *local* values of the Young modulus, the radius of curvature and the surface energy, and not the bulk macroscopic values. In 1997, Johnson and Greenwood [37] constructed a map of the elastic behavior of bodies, shown in Fig. 10, permitting to find the theory to be applied depending on the material properties. The authors observe that AFM experiments usually fall in the Maugis region.

At our knowledge, the only experimental verification of the Maugis theory is that of Lantz et al. [38]. In this work, the contact area between a Pt/Ir coated Si tip and graphite is deduced from current, friction, and normal force measurements. The experimental data are shown to follow a Maugis model rather than an hertzian law. Measurements are repeated for a Si tip on $NbSe_2$.

Finally, all the theories reviewed in this section are continuum elastic theories and hence assume smooth surfaces with no plastic deformation and no viscoelastic phenomena.

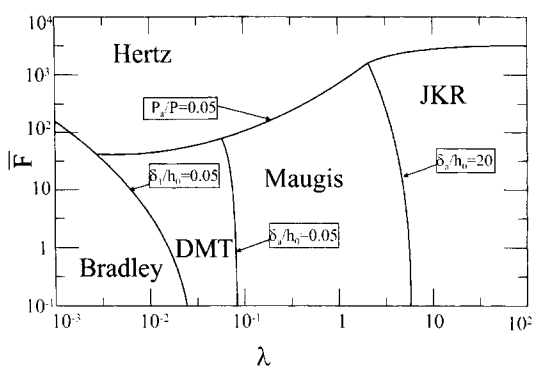

Fig. 10. Map of the elastic behavior of bodies. P_a/P is the ratio between the adhesive part of the load and the total load. When the adhesion is negligible, bodies fall in the Hertz limit (approximately $F > 10^3\,\pi W R$). δ_1 is the elastic compression, and h_0 is an equilibrium distance. When $\delta_1 \ll h_0$, the bodies are rigid and follow Bradley theory ($\lambda < 10^{-3}$). δ_a is the deformation due to adhesion. When the adhesion is small the behavior of materials is described by the DMT theory (approximately $10^{-2} < \lambda < 10^{-1}$), whilst JKR theory predicts the behavior of highly adhesive bodies (approximately $\lambda > 10^1$). The Maugis theory suits to the intermediate region (approximately $10^{-1} < \lambda < 10^1$) (adapted from [37]).

2.4. Artifacts

One of the most striking artifacts concerning contact lines is due to the piezoelectric actuators hysteresis and creep [7]. As a matter of fact, in order to acquire force–displacement curves sequentially, the piezo actuator has to be ramped repeatedly along Z. Hysteresis and creep affect the zero line of the approach curve and the contact line of the withdrawal curve, i.e., the regions near the inversion of motion.

Hysteresis and creep lead to an incorrect determination of displacements. In particular, because of creep, the loads in the unloading curve for a given displacement may appear bigger and finally overcome those of the loading curve. This unphysical phenomenon is called "reverse path effect".

Several methods have been proposed in order to compensate for hysteresis and creep effects. To our knowledge, the only method applied to force–distance curves is the one that uses lead magnesium niobate (PMN) actuators [7] which have less non-linearities when used in a cyclic application. However, PMN ceramics are electrostrictive materials for which the strain is proportional to the square of the applied field and the displacement is thus independent of the sign of the applied voltage yielding only one half the displacement range of a corresponding lead zirconate titanate (PZT) actuator. Furthermore, PMN response is much more temperature dependent.

Aimé et al. [24] have studied the elastic behavior of viscoelastic materials. For such materials, the work of adhesion is a function of the Z scan rate v, i.e.,

$$W_v = W(1 + \zeta(T)v^n), \tag{2.15}$$

in which $\zeta(T)$ is a function characterizing the material, T is the temperature and n is found to be equal to 0.6. This dependence of the adhesion force, when inserted in the equations describing the elastic behavior of materials, leads to a dependence of the loading/unloading curves on velocity. Furthermore, since the hysteresis changes with the scanning frequency, the slope of the contact lines decreases with frequency, even in the case of hard, inorganic, non-viscoelastic surfaces.

Besides viscoelastic properties, another source of artifacts not accounted for in the elastic continuum media equations is surface roughness. Both AFM tips produced by electrochemical etching and tips produced through microfabrication techniques have on the surface some small asperities which can reach few nanometers in size. In the contact region of the force–displacement curve the effect of asperities is twofold. On the one hand, for a given load, the deformation depth is enhanced since the actual contact radius is much smaller than the macroscopic tip. On the other hand, the surface deformation is smaller than that expected for a single asperity contact since there are multiple contacts and the load will be distributed over many points. Cohen [39] has compared the deformations in the case of a smooth tip (radius 1 μm) and of a rough tip on a flat gold surface. The roughness is described as a distribution of hemispherical minitips (radius 2 nm), and the contact is modeled with an hertzian law. Deformations due to the rough tip turn out to be larger than the one in the case of a smooth tip. Anyway, for forces above 1 μN, the slope of the deformation vs. load curve is the same in the two cases, since above a certain load, the microasperities are buried and the entire tip surface comes in contact.

Hoh and Engel [40] have shown that the loading/unloading hysteresis is scan-rate dependent. At high scan rates the separation between the two contact lines is large. As the scan rate is decreased, this separation reaches a minimum after which it increases again. Such a scan-rate dependence is typical of stick slip friction and is not consistent with effects arising from electromagnetic forces. The authors propose that the friction between the tip and sample makes the cantilever bow forward after the tip

comes in contact, resulting in an offset of the contact line. As the tip is retracted, the cantilever bends upward, causing an opposite effect in the line. At the turn-around point, the deflection signal jumps nearly vertically, as it would be expected when the cantilever turns up from a forward bow. Unfortunately, no experiment has been carried out to separate the effects of friction and of scan rate dependent hysteresis.

Haugstad and Glaedfelter [41] have studied the effect of photodiode non-linearities on the contact lines of force–displacement curves. The withdrawal contact line is the portion of the force–displacement curves with the highest repulsive and/or attractive loads, and hence with high cantilever deflections. In turn, this means high displacements of the laser spot on the photodiode. The authors prove, experimentally and theoretically, that the difference between the measured contact line and the line $\delta_c = Z$ is a cubic curve whose maximum contribution is about 8% of the total signal. This non-linear contribution is related to the features of the photodiode. The measurements are done on a rigid material, namely polycrystalline Si_3N_4, so that sample deformations can be neglected.

2.5. Experimental results

The first pioneering work dealing with the determination of materials elasto-plastic properties by means of an AFM is that of Burnham and Colton [42]. Using a hertzian analysis, the modulus of elasticity has been drawn from the experiments for an elastometer, HOPG graphite, and gold, in rather good agreement with literature values.

Acquiring force–displacement curves on gold, Cohen et al. [43] have shown the effect of microasperities on an iridium tip, as indicated in Section 2.4. The same effect has been discussed by Blackman et al. [44] pointing out the inadequacy of continuum elastic theories and the need of models for atomic-scale contacts.

Hao et al. [21] have measured the slope of loading/unloading curves for graphite, mica, and stainless steel, finding inexplicable results for graphite. The authors account neither for elasticity theory nor for microasperities effects. Consequently, they are unable to explain the discrepancy between expected and measured values.

Aimé et al. [24] have characterized force–displacement curves on rigid and soft polymer films in controlled atmosphere. The authors point out several causes of misinterpretation of force–displacement curves: the lack of an accurate knowledge of the cantilever stiffness and of the tip size and the difficulty in separating viscoelastic, elastic, and plastic effects. Even with these numerous restrictions, AFM measurements can lead to a characterization of the film properties. Following the JKR theory and taking into account viscoelastic effects (see Section 2.4), a good agreement between theoretical and experimental values is obtained.

Thomas et al. [45] have acquired force–displacement curves between a W tip and a gold sample covered with a monolayer of docasanethiol. They show that the deformation follows an hertzian model for forces smaller than 15 μN, but a considerable loading/unloading hysteresis appears for loads of about 25 μN.

Weisenhorn et al. [46] have compared load vs. indentation curves on glass, polyurethane, and rubber, showing that it is possible to distinguish between two polyurethane layers of different Young's modulus (namely 14 and 30 MPa).

The measurement of elastic properties of biological materials has been pioneered by Tao et al. [47], who have measured elastic properties of bones, comparing them with stainless steel and rubber.

Radmacher et al. [48] have measured the indentation of an Si_3N_4 tip on lysozyme adsorbed on mica. A good agreement between Hertz equation for a sphere on a flat surface and experimental data is reached (although the formula reported in the text is affected by an error, and it is not clear if the same error affects also the fit of the data). What is most important, the authors show the different behavior of lysozyme and mica in indentation measurements, thus leading to the possibility of distinguishing the two materials throughout the acquisition of force–displacement curves. Later on, Radmacher et al. [49], acquiring force–displacement curves on gelatin, have shown that the agreement with Hertz equation improves when the tip is modeled as a cone for higher loads and as a sphere for small loads. They proved the capability of AFM force–displacement curves to measure the change of gelatin elastic properties under various conditions. The gelatin was immersed in pure water, propanol, or mixtures of the two, and the measurement of the Young modulus reached a resolution of 0.5 MPa.

Domke and Radmacher [50] have determined the Young modulus of gelatin layers of different thickness. They have verified that the calculated Young modulus depends both on the thickness of the medium and on the portion of the contact line used for the calculation. In particular, the Young modulus of a thick film (1.1 μm) depends very little on the range of analysis (it goes from 15.9 kPa for cantilever deflections in the range 10–30 nm up to 18.5 kPa in the range 170–200 nm). The load–deformation curve is well fitted with the hertzian model. In the case of the thin film (<300 nm), the Young modulus is 27 kPa in the range 10–30 nm and it is bigger than 1 GPa in the range 170–200 nm. The load–deformation curve cannot be fitted with the hertzian model. As a matter of fact, when the tip indents a thin film, at high loads the deformation–load curve is influenced by the presence of the rigid substrate, that in turn cannot be probed with a thick film.

Several load–indentation studies have been performed on cells. Ricci and Grattarola [51] have explored the possibility of measuring cell height by means of indentation–load curves. No calculation is presented for cells elastic modulus.

Finally, several works have exploited dynamic force–distance curves in order to characterize sample elasticity [52, 53].

Experiments dealing with the study of elastic properties of materials by means of the AFM have shown that the absolute measurement of Young modulus or other elastic properties is not a simple and straightforward issue, whereas the comparison of elastic properties of different materials gives quite satisfactory results. However, the AFM turns out to be the only instrument able to characterize the local elastic properties of materials with high lateral resolution (25 nm) [11].

3. Theories of non-contact region

3.1. Approach curve: jump-to-contact and attractive forces

The jump-to-contact is one of the important quantities one can measure in a force–displacement curve. As discussed in Section 1.3, this discontinuity occurs when the gradient of the tip–sample force is larger than the elastic constant of the cantilever. The general expressions of the cantilever deflection and the tip–sample distance at which the tip jumps onto the surface are given by Eqs. (1.9).

The jump-to-contact may be preceded by a region of attractive (Van der Waals or Coulomb force) or repulsive (Van der Waals force in certain liquids, double-layer, hydration, and steric) force. The jump-to-contact gives information on attractive forces between the tip and sample. The maximum

sampled value of the attractive force equals the jump-to-contact cantilever deflection $(\delta_c)_{jtc}$ times the cantilever elastic constant. In order to evaluate such attractive forces it is necessary to know the force law and the tip shape. In Section 6 we consider in detail the different forces and the influence of the tip shape.

The onset of a jump-to-contact is predicted by any theory that takes attractive forces into account (JKR or Maugis) and is also predicted by numerical calculations [31, 35].

In AFM measurements the jump-to-contact instability is governed by the stiffness of the cantilever relative to the long-range tip–sample forces. As indicated in Section 1.3, if the cantilever elastic constant is bigger than the maximum value of the tip–sample force gradient, then the discontinuities virtually disappear. However, jump-to-contact is always present at an atomic scale, even if the cantilever can be modeled as an infinitely rigid body. In this case, the jump-to-contact instability is governed by the inherent stiffness of the tip and sample materials, related to their cohesive strengths. This phenomenon has been demonstrated by Pethica and Sutton [54] by means of calculations employing Lennard-Jones potentials and by Landman et al. [55] by use of molecular dynamics (MD) simulations.

Pethica and Sutton [54] have shown that in general it exists a minimum separation ($\cong 1-2$ Å) below which the surfaces jump in contact irrespective of the rigidity of the holder. This instability is due to the fact that, at some small enough separation, the gradient of the surface forces exceeds the gradient of the elastic restoring force of the bodies. The instability is irreversible because surface forces have stronger separation dependence than does the elastic restoring force. The Lennard-Jones pair potential used by Pethica and Sutton is inapplicable to free surface structures. *N*-body potentials of the embedded-atom variety are much more reliable. They do not, however, account for long-range attractive forces, because they do not incorporate a Van der Waals term.

Landman et al. [55] verified the onset of jump-to-contact instability by means of MD simulations and compared their results to AFM measurements for a nickel tip interacting with a gold substrate. In MD simulations the tip is modeled as a pyramid with an effective radius of curvature of $\cong 30$ Å and the sample is made up of 11 layers of 450 atoms per layer. The interatomic interactions governing the energetics and dynamics of the system are modeled by means of the embedded-atom method (EAM). In the EAM [56], the dominant contribution to the cohesive energy of the material is viewed as the energy to embed an atom into the local electron density provided by other atoms of the system. The AFM measurements were carried out with a nickel tip with a radius of curvature of $\cong 200$ nm and the cantilever spring constant is $\cong 5$ kN/m. The measurements were done under dry nitrogen.

MD simulation shows the onset of an instability when the tip is at a distance of 4.2 Å from the sample. This jump-to-contact is associated with a tip-induced sample deformation and the process involves large atomic displacements ($\cong 2$Å) occurring in a time span of $\cong 1$ ps. When the tip jumps onto the surface, the distance decreases from 4.2 to 2.1 Å. Just after the jump-to-contact, in addition to the adhesive contact between the two surfaces, a partial wetting of the tip bottom by Au atoms induced by adhesion is observed (panel (a), Fig. 11). Pressure contours reveal that atoms at the periphery of the contact area are under extreme tensile stress ($\cong 10$ GPa), in accord with the JKR theory (panel (b), Fig. 11). In the AFM experiment the magnitude of the force and the distance from the sample at which the tip begins to deviate from zero are much larger than those predicted by the MD simulation. The authors list several causes of these differences: tip dimensions, cantilever elastic constant, neglect of long range attractive forces in MD calculations, tip and sample roughness, and the exposure to air of the tip and sample.

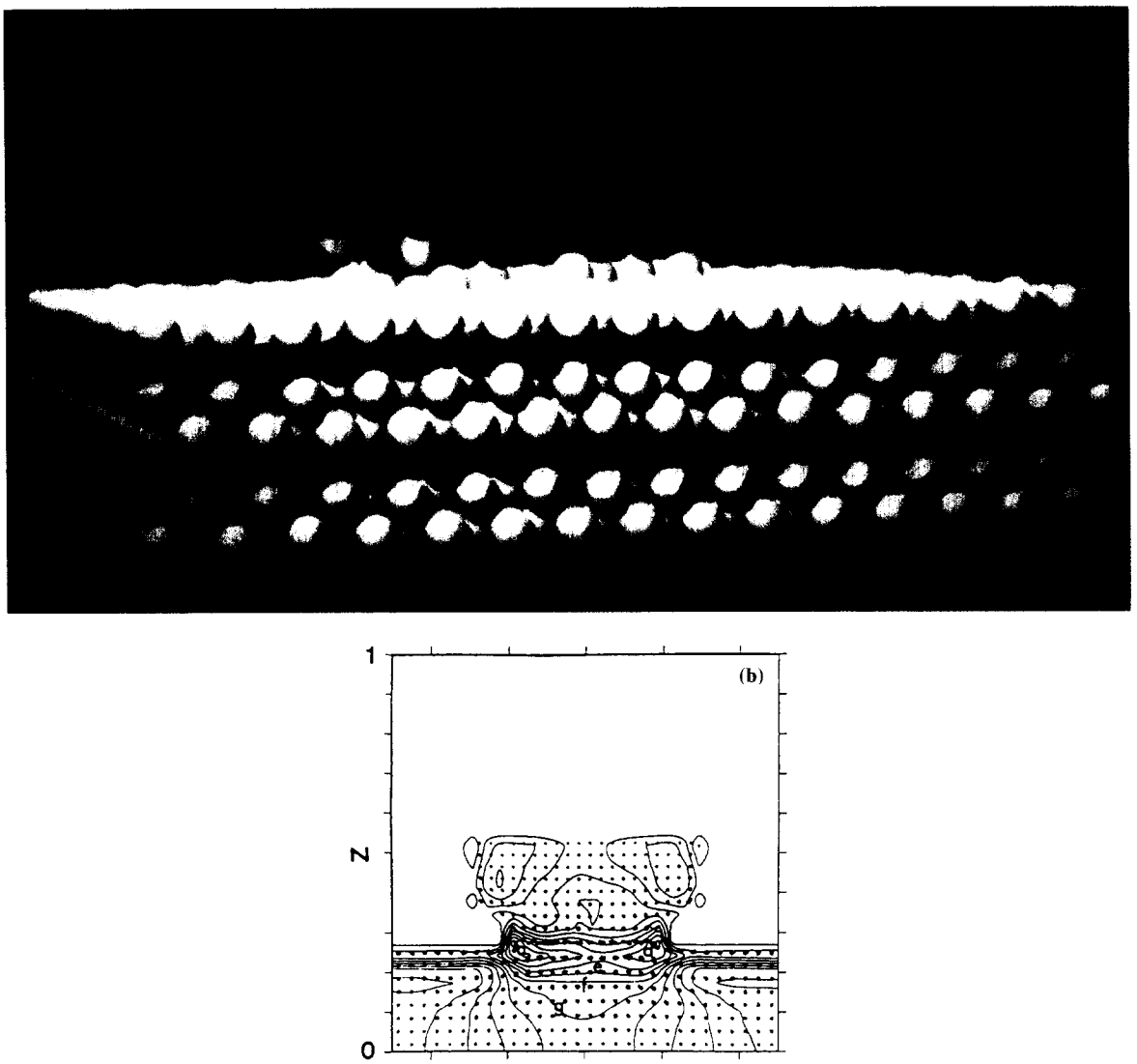

Fig. 11. Atomic configuration generated by the MD simulation (panel (a)) and calculated pressure contours just after the jump-to-contact (panel (b)) (reprinted with permission from [55]; copyright 1990 American Association for the Advancement of Science).

3.2. Withdrawal curve: jump-off-contact and adhesion forces

The second discontinuity of force–displacement curves, the jump-off-contact, occurs when, during the withdrawal of the sample, the cantilever elastic constant is larger than the gradient of tip–sample adhesive forces.

As we have already seen in Sections 2.2 and 2.3, the jump-off-contact is related to tip and sample surface energies via equations that depend on materials dimensions, stiffness, and adhesion. The jump-off-contact force can be deduced from Fig. 9. For an infinitely stiff tip-holder, the pull-off load is given

by the horizontal tangent to the deformation–load curves in panel (b) of Fig. 9. When the apparatus has a finite stiffness, the tangent to the curve in panel (b) of Fig. 9 with a slope corresponding to the elastic constant of the support has to be drawn. It is evident that Maugis theory shows that the pull-off force gradually passes from $(F_{ad})_{JKR} = -3/2\pi RW$ to $(F_{ad})_{DMT} = -2\pi RW$ as the parameter λ, that describes tip and sample dimensions, stiffness, and adhesion, decreases. Similar results were obtained by Müller et al. [32] and have been confirmed by Greenwood [35]. Hence, measuring the pull-off force is not an accurate method to estimate surface energies. Nevertheless, the jump-off-contact shows a wide range of adhesive material properties.

The jump-off-contact deflection and the jump-off-contact distance are always greater than jump-to-contact deflection and jump-to-contact distance, respectively. This occurs for several reasons.

1. During the contact some chemical bonds or adhesive bonds may engender non-conservative forces.
2. During the contact, the sample deforms, buckles and "wraps" around the tip, increasing the contact area, because of the elastic behavior described in Section 2, but also under the influence of particular tip–sample forces (e.g., hydrophobic force and viscoelastic forces). Thus, soft materials with low cohesive energies containing hydrophobic groups, as some biological materials, have a large pull-off force in water, and the jump-off-contact occurs as a gradual detachment rather than a sharp discontinuity.

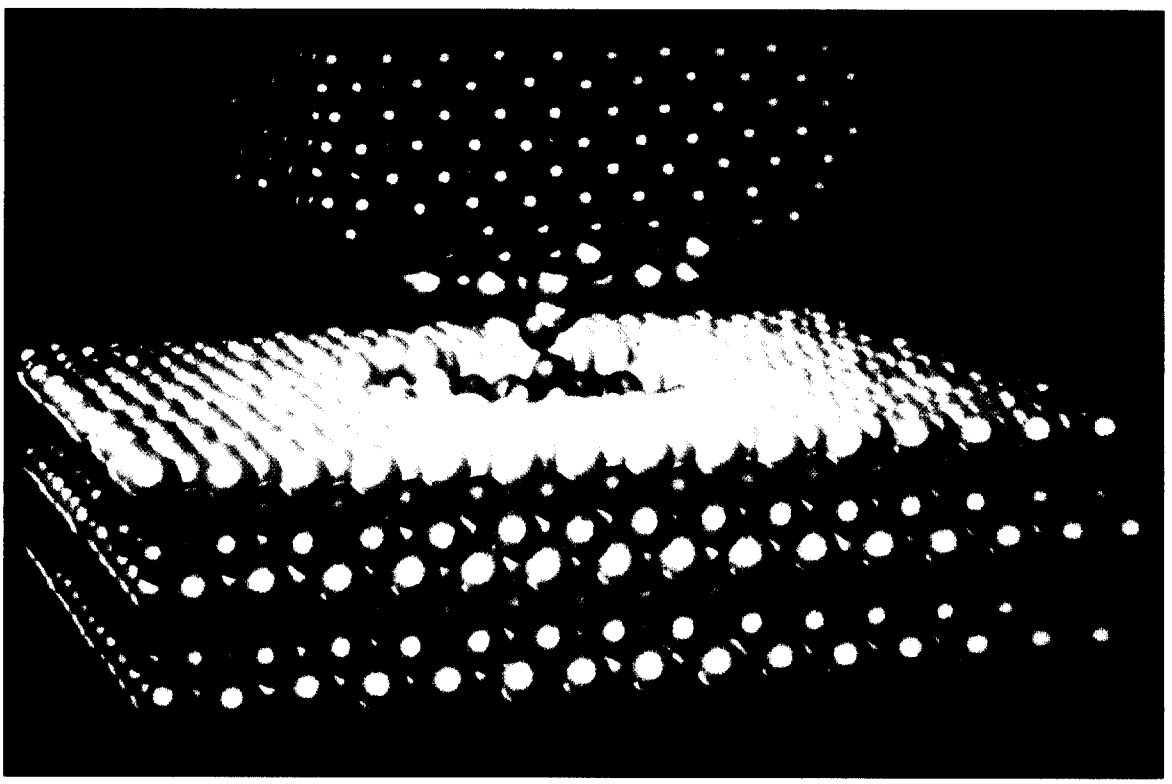

Fig. 12. Neck formation in the case of a separation without indentation (panel (a)) and a cut through the system at the point of maximum indentation, i.e., the point M in panel (c) (panel (b)). The calculated force–displacement curve corresponding to the situation in panel (b) is shown in panel (c). The capital letters from D to X indicate the stages of the non-monotonic detachment (reprinted with permission from [55]; copyright 1990 American Association for the Advancement of Science).

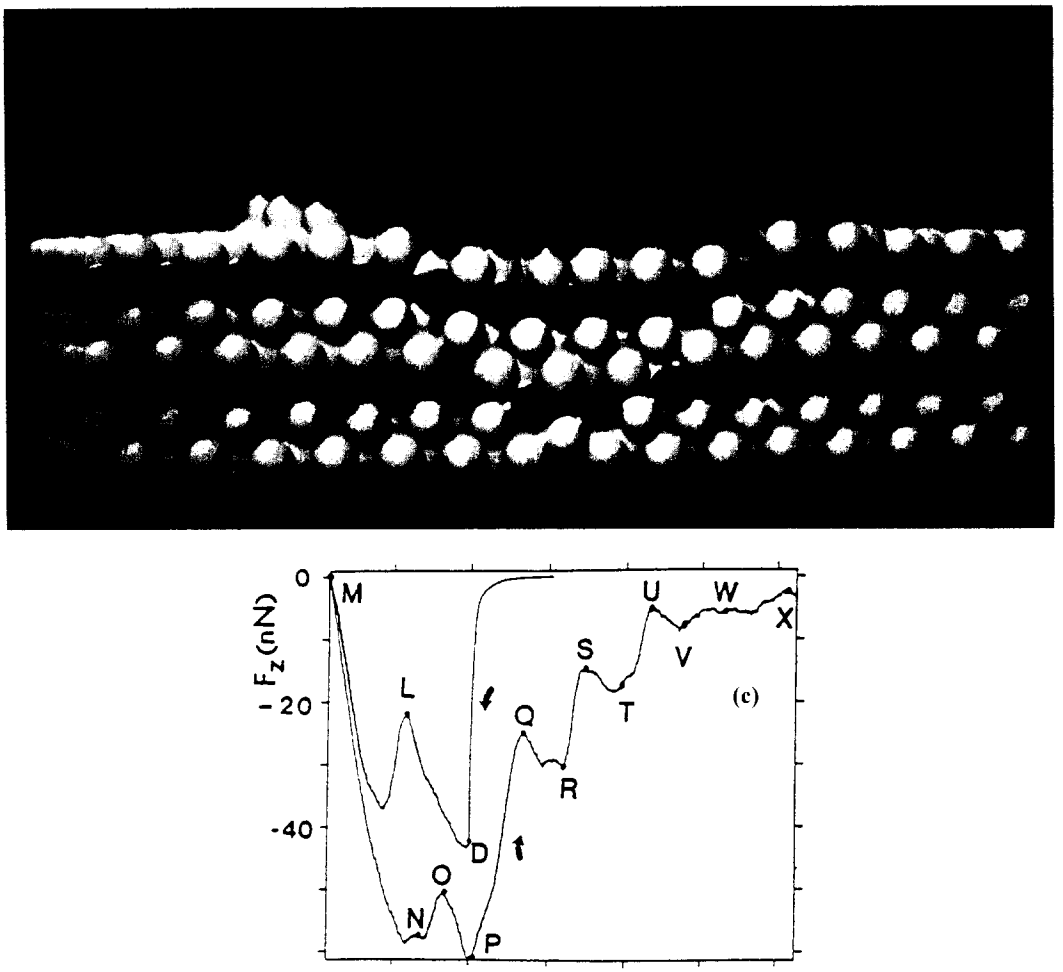

Fig. 12. (contd.)

3. Meniscus force exerted by layers of liquid contaminants (chiefly water) acts against the pull-off [57].
4. In the absence of chemical bonds, non-elastic deformations or meniscus forces, the interaction force could be described by a Lennard-Jones like force and the mechanisms involved in force–displacement curves acquisition would be well described by Fig. 2. It is evident that, also in this case, the discontinuity CC′ is greater than BB′. This is the most important reason of force–displacement curves hysteresis, because it is almost always present.

As for the jump-to-contact, it is not possible to eliminate the jump-off-contact and the approach–withdrawal hysteresis, even in the absence of chemical bonds, non-elastic deformations or meniscus forces and even if the tip-holder is infinitely rigid. This phenomenon is illustrated by the MD calculations of Landman et al. [55] already discussed in Section 3.2.

In their work, both MD simulations and AFM experiments have been performed with and without indentation. When the tip is immediately withdrawn after jump-to-contact, i.e., it is not allowed to

indent the sample, the separation is associated with inelastic processes in which the surface atoms of the gold sample adhere to the tip. While the tip is further lifted, the contact area decreases and a thin "adhesive neck" forms, as shown in panel (a) of Fig. 12. This neck breaks at a distance of 9–10 Å. The pull-off force is of the order of 40 nN.

When the tip is allowed to indent the sample, the connective neck is wider and elongates for a larger distance during withdrawal, as shown in panel (b) of Fig. 12. The elongation process occurs in several stages in which the atoms of a layer disorder and then rearrange to build up another layer, i.e., to extend the neck. The number of atoms in the neck is roughly constant throughout the elongation process. These stages result in a series of monotonous decrease of attractive forces (just after the creation of a new Au layer in the neck) followed by increase (before the formation of a further layer), as indicated in panel (c) of Fig. 12. The pull-off force is about 60 nN and the neck breaks at a distance of about 13 Å.

The same behavior (a series of discontinuities) has been predicted for the case of the fracture between two identical materials by Lynden-Bell [58]. Pethica and Sutton [54] and Attard and Parker [31] obtained similar results by use of Lennard-Jones potentials.

The associated AFM experiments of Landman et al. exhibit approach–withdrawal hysteresis both with and without indentation. The jump-off-contact force is $\cong 4\,\mu N$ without indentation and $\cong 5\,\mu N$ with indentation. Pull-off distances are of the order of 16 nm. However, the non-monotonic features predicted by MD calculations are not discernible in the withdrawal curve after indentation. The experiment is apparently not sensitive to such individual atomic-scale events when averaged over the whole contact area.

In 1995, Agraït et al. [59] have succeeded in detecting such discontinuities during jump-to-contact and jump-off-contact. They have measured forces between a gold tip and a gold substrate in vacuum at liquid helium temperature (the substrate is mounted on the cantilever and also the tunneling current can be measured). They showed that necks are formed during jump-to-contact and jump-off-contact, and that such necks elongate (compress) during the unloading (loading) process. As the neck is elongated, the current decreases stepwise, while the force decreases with an oscillatory sawtooth-like behavior. Abrupt relaxations of current correlate to abrupt relaxations of force and they occur at 0.1–0.2 nm intervals in displacement. During a complete loading–unloading cycle, structural transformations are reversible. The neck radius varies about 1 nm in an elongation of 1 nm. The effective elastic constant of the necks varies linearly with the contact radius (see also Ref. [60]).

The increase of force–displacement curves hysteresis with indentation has also been observed by Weisenhorn et al. [61]. For indenting distances smaller than 10, 70 and 150 nm, the pull-off force is smaller than 0.35, 0.35 and 0.70 nN. Toikka et al. [62] have measured the dependence of pull-off force and adhesion energy on the loading force in air and in water. In air the adhesion energy goes from 3 mJ/m^2 for zero load up to 5 mJ/m^2 for a loading force of 120 nN. In water it goes from 0.3 mJ/m^2 for zero load up to 1.2 mJ/m^2 for 120 nN. These authors also verified an hysteretical behavior in the dependence of pull-off force on loading force along a complete cycle, i.e., first increasing and then decreasing the loading force.

We have already said that both the jump-to-contact and the jump-off-contact due to inherent stiffness of the tip cannot be eliminated, but in AFM force–displacement curves, jumps are also due to the stiffness of the cantilever, and so they could be eliminated using a stiffer cantilever to the detriment of force sensibility. Alternative approaches, making use of magnetic or electric force feedback loops, have succeeded in eliminating force–displacement curves discontinuities.

In 1992, Gauthier-Manuel [63] devised a feedback loop, using an inhomogeneous magnetic field produced by a coil, in order to keep constant the force on a tip and prevent it from jumping onto the sample surface. By means of such an apparatus, the author could sample the entire tip–sample force law. The feedback loop was not applied to an usual AFM tip mounted on a cantilever, but the author himself noted that this would be possible. Jarvis et al. [64] and Yamamoto et al. [65] have developed a feedback loop (similar to the one of Gauthier-Manuel) to be applied to the AFM tip. The force on the cantilever, and hence the cantilever deflection, is kept constant and the tip–sample force is deduced from the feedback correction signal. In both works force–distance curves without hysteresis are shown. In order to make the tip sensitive to the applied magnetic field, a small piece of magnetic material is mounted directly behind the tip. Quite different approaches are that of Joyce and Houston [66], in which the force is counterbalanced by a differential capacitance sensor acting also as displacement detector, and that of Bryant et al. [67], in which the deflection of the cantilever is measured by means of a tunneling tip and the position of the cantilever is adjusted by moving the lever holder.

By using these feedback techniques, the stiffness of the cantilever is in practice infinitely increased (no displacement of the tip occurs, whichever is the amplitude of the force) without decreasing the force resolution. The distance dependence of the force can be entirely sampled without losing the details.

4. The zero line

The zero lines are the parts of force–displacement curves in which the tip exerts no force on the sample, e.g., when the tip and sample are far apart, and the tip does not deflect.

Despite that almost no force can be detected in this portion of the curve, zero lines have a great importance in that, as discussed in Section 1, all distances are referred to the cantilever rest position. Thus, the forces can be calculated only when the deflection of the cantilever, i.e., the difference between the current deflection and the rest position, is known. The latter is given by the zero line.

Zero lines seldom happen to be lines. They always have a superimposed oscillation due to optical interference between the beam reflected by the upper face of the cantilever and that scattered by sample surface, as shown in Fig. 13. The laser beam (i in Fig. 13) reaches the sample because the laser spot is not completely inside the lever surface and because of the fact that part of the light passes through the cantilever. The beam that reaches the sample is scattered, resulting in a second beam pointing towards the photodiode (r_2). r_2 interferes with the beam reflected by the upper face of the cantilever (r_1). The resulting oscillation has a fixed spatial period determined by the laser light wavelength and by the microscope geometry.

The optical path difference s is given by [61]:

$$s = n\frac{(1+\cos 2\Theta)}{\cos\Theta}D, \tag{4.1}$$

in which D is the cantilever–sample distance, Θ the incidence angle and n is the refractive index of the medium. If Λ is the wavelength of the laser, the spatial period of the oscillation is given by

$$\bar{D} = \frac{\Lambda}{n((1+\cos 2\Theta)/\cos\Theta)}. \tag{4.2}$$

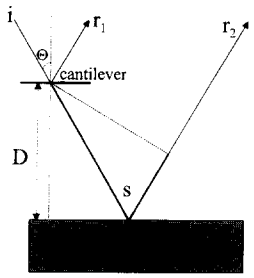

Fig. 13. Schematic representation of the interference between the laser beam reflected by the upper face of the cantilever and the beam scattered by the sample surface, resulting in an oscillation on the zero lines of the force–displacement curves.

Also the zero lines exhibit a kind of hysteresis that results in a separation of approach and withdrawal traces. The hysteresis of zero lines is due to the viscosity of the medium. The viscous force pulls the cantilever upward when approaching the sample and makes it bend downward when the sample is withdrawn. Hoh and Engel [40] have measured this hysteresis by altering the viscosity of the medium and the scan rate. Force–displacement curves obtained in water and glycerol are shown in Fig. 14. In water, there is a notable effect for velocities bigger than 30 μm/s. The separation between approach and withdrawal zero lines is about 5 nm for a cantilever 200 μm long, a scan range of 500 nm and a scan rate of 40 μm/s. In a high viscosity medium such as glycerol (15 P instead of 10^{-2} P for water) the separation becomes very large even at low scan rates ($\cong$ 10 nm for 0.6 μm/s and $\cong$ 50 nm for 4.8 μm/s). In a low viscosity medium such as air (2×10^{-4} P) zero lines hysteresis is hardly detectable (see also Ref. [68]).

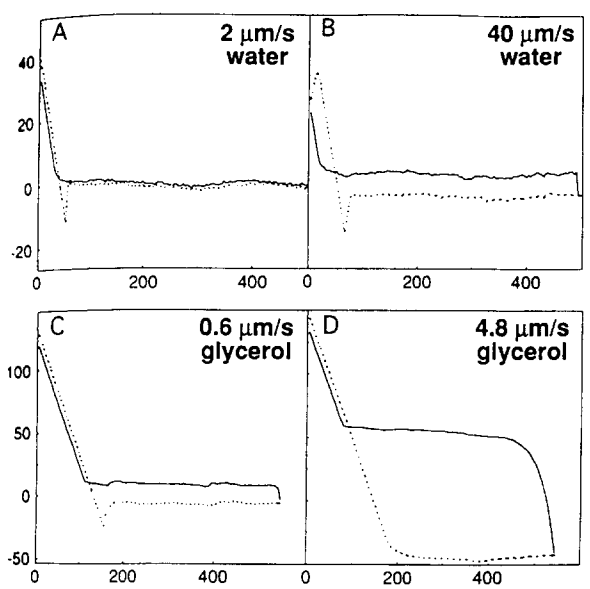

Fig. 14. Zero-lines hysteresis in water and in glycerol. On the x-axis, the sample position in nm. On the y-axis, the cantilever deflection in nm. (reprinted with permission from [40]; copyright 1993 American Chemical Society).

5. Calibration

5.1. Methods for the calculation of forces

All AFM, whether home made or not, provide the cantilever deflection as a function of the distance between the sample and the rest position of the cantilever. In order to know the tip–sample force, several transformations of the data have to be performed. Eq. (1.10) reveals that, if the sample is much more rigid than the cantilever and no deformation of the sample occurs, along the contact line the deflection of the cantilever equals the displacement of the piezoactuator, i.e., $\Delta\delta_c = \Delta Z$.

Usually, if the optical lever method is employed, the deflection of the cantilever is given by the voltage output of the photodiode. This voltage, however, depends also on laser spot shape and dimensions. Along the contact line, the relation between the voltage output ΔV and the displacement of the piezo is given by

$$\Delta\delta_c = \Delta Z = \Delta V/\Omega, \tag{5.1}$$

where Ω is a proportionality factor. In order to know δ_c the zero deflection value V_0 of the voltage is needed, and can be determined from the zero line.

A first problem with this procedure is associated with the hysteresis and the creep of the piezo, affecting the measurement of Z. As a general rule, the response of the piezo should be checked previous to any force–distance curves acquisition and Eq. (5.1) should be applied to approach curves. Furthermore, depending on the sample, the relation $\Delta\delta_c = \Delta Z$ might not be correct at low loads. Hence, as a rule of thumb, it is always better to consider in the above procedure the tangent to the loading curve at high loads. The origin of the Z axis is placed at the beginning of the contact line. Because of tip asperities, the contact line may begin prior to intimate true contact. Thus, the asperities on the tip affect the determination of tip–sample distances. Taking into account all these effects, tip–sample distances can be determined by means of the equation:

$$\Delta Z = -\frac{L_p}{w_p} d_{31} \Delta V, \tag{5.2}$$

in which L_p and w_p are the length and the wall thickness of the piezotube, d_{31} is a proportionality factor characteristic of materials, and V is the voltage applied to the piezo.

The factor Ω in Eq. (5.1) depends on the dimensions and on the shape of the laser spot on the photodiode, and hence depends on the refractive index of the medium in which the measurements are performed [69]. Furthermore, this factor may change in time due to the thermal drift of the components of the microscope, and should be checked previous to any measurement.

Once the deflection of the cantilever in nanometers is known, the product $k_c \Delta\delta_c$ gives the force in newtons:

$$\Delta F = k_c \Delta\delta_c = k_c \Delta V/\Omega. \tag{5.3}$$

Once the true tip–sample distance is known, and the force has been deduced from cantilever deflections, the curve can be rearranged in order to give a "normalized" representation, i.e., a plot of the force vs. the true tip–sample distance D. This representation is referred to as the "force–distance curve" (see Section 1.2). This procedure corresponds to the reversal of the geometric construction presented in Section 1.2.

The main problem in the calculation of forces is given by the knowledge of the cantilever elastic constant.

5.2. The cantilever elastic constant and the tip radius

The nominal elastic constant of rectangular and "V"-shaped [70] cantilevers is given by

$$k_c = \frac{E t_c^3 w}{4L^3} \quad \text{(rectangular cantilever)}, \tag{5.4}$$

and

$$k_c = \frac{E t_c^3 W b}{2b(L_1^3 - L_2^3) + 6WL_2^3} \quad \text{(“V”-shaped cantilever)}, \tag{5.5}$$

in which t_c is the thickness, E is the Young modulus and the other quantities are defined in Fig. 15. Eq. (5.5) is not an exact formula. The elastic constant of "V"-shaped cantilevers was calculated by use of the "parallel beam" approximation [71, 72], in which the "V"-shaped cantilever is modeled as a couple of rectangular cantilevers. Sader and White [73] have demonstrated the inaccuracy of such an approximation by means of a finite element calculation.

A more accurate formula has been given by Neumeister and Ducker [74]:

$$\begin{aligned} k_c &= \left[\Delta_I + \Delta_{II} + \Psi\left(\frac{W}{\sin\alpha} - d\right)\right]^{-1}, \\ \Delta_I &= \frac{3}{E t_c^3 \,\mathrm{tg}\alpha}\left[\left(\frac{W}{\sin\alpha} - 2d\right)^2 - d^2\left(2\log\frac{W}{d\sin\alpha} + 1\right)\right], \\ \Delta_{II} &= \frac{L^2}{EWt_c^3\cos^2\alpha}\left[\frac{2L}{\cos\alpha} + 3(W\cot\alpha - d\cos\alpha - \vartheta\sin\alpha)\right], \end{aligned} \tag{5.6}$$

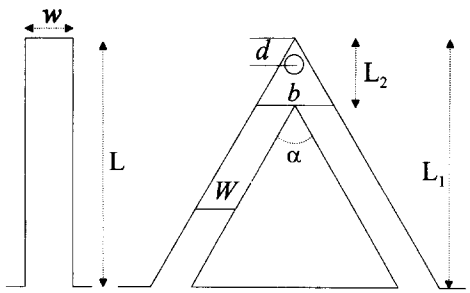

Fig. 15. Schematic representation of a rectangular and a "V"-shaped cantilever. L and w are the length and the width of the rectangular cantilever, W is the width of the arms of the "V-shaped" cantilever, α is the angle between the arms, b and L_2 are the base and the height of the triangle at the end of the "V-shaped" cantilever, L_1 is the total height of the "V-shaped" cantilever, and d is the distance between the center of the tip and the end of the cantilever.

and

$$\Psi = \frac{3L(1+\nu)}{EWt_c^3 \cos\alpha}\left(\frac{W}{\sin\alpha} - d + \vartheta\cot\alpha\right),$$

in which ν is the Poisson ratio and ϑ is given by

$$\vartheta = \frac{L\,\mathrm{tg}\alpha + (W - d\sin\alpha)(1-\nu)\cos\alpha}{2 - (1-\nu)\cos^2\alpha}. \tag{5.7}$$

All the above formulas depend on the knowledge of E and ν (E = 304 GPa and $\nu = 0.24$ for the silicon nitride) that can be measured by different techniques (see Ref. [75] and references therein). Anyway, each cantilever has its own elastic constant that can vary between cantilevers on the same wafer, and hence, rather than calculate them, it would be better to measure them. Several methods have been proposed for doing this as indicated below.

The most effective method is that proposed by Cleveland et al. [76]. Consider a rectangular cantilever with elastic constant k_c and mass m_c. The resonance frequency of this cantilever is

$$\omega_0 = \sqrt{\frac{k_c}{m^*}}. \tag{5.8}$$

The effective mass m^* is given by $m^* = m_c + 0.24\,m_t$, where m_t is the mass of the tip. When an extra mass M is added, the resonance frequency becomes

$$\omega_1 = \sqrt{\frac{k_c}{M + m^*}}. \tag{5.9}$$

By measuring ω_1 and ω_0, k_c is given by

$$k_c = \frac{M}{1/\omega_1^2 - 1/\omega_0^2}. \tag{5.10}$$

The added extra mass is usually a sphere placed near the end of the cantilever. Since the sphere is secured onto the cantilever by adhesive forces (e.g., capillary force), the method turns out to be non-destructive.

Senden and Ducker [77] have proposed a similar method in which a tungsten sphere (10–50 μm in diameter) is glued at the end of the cantilever and the static deflection due to gravity is measured. Subsequently, the cantilever is turned upside down and the deflection is measured again. The difference $\Delta\delta$ between the two measurements is twice the deflection due to the gravity. The deflections can be calibrated as shown in Section 5.1 and the spring constant is given by

$$k_c = \frac{8\pi R^3 \rho g}{3\Delta\delta_c}, \tag{5.11}$$

in which R is the radius, ρ the density of the sphere and g is the gravitational acceleration. Hutter and Bechhoefer [78] have measured the spring constant of the cantilever from the power spectral density of cantilever fluctuations due to thermal noise. If the cantilever is modeled as a harmonic oscillator, then

$$\left\langle \frac{1}{2} m\omega_0^2 \delta_c^2 \right\rangle = \frac{1}{2} k_B T; \quad \omega_0^2 = k_c/m \quad \text{and} \quad k_c = k_B T/\langle \delta_c^2 \rangle. \tag{5.12}$$

Rabinovich and Yoon [79] have calibrated the spring constant of a cantilever by comparing it with the spring constant of a glass fiber. The glass fiber spring constant is measured by detecting its deflection under a known weight. After mounting the glass fiber on a piezoactuator, it is brought into contact with the cantilever of unknown elastic constant. The cantilever spring constant is given by

$$k_c = k_f\left(\frac{\Delta Z}{\Delta \delta_c} - 1\right), \tag{5.13}$$

in which k_f is the spring constant of the glass fiber and ΔZ is the displacement of the piezo. The same authors have tested their technique together with that of Ducker and Senden, and have compared the values obtained with those calculated by means of Eq. (5.4) [80]. All three methods give k_c values within ±7% of each other.

Finally, Sader et al. [81] have developed a technique to calculate the cantilever spring constant once the mass or the density of the cantilever is known. These quantities are not provided by the manufacturers, so the method is rather useless.

Another major problem encountered when a quantitative treatment of force–distance curves is undertaken is the characterization of the size and shape of tips. Forces depend on the dimensions of the tip both on a mesoscopic (overall shape of the tip) and a microscopic range (shape of the apex and presence of asperities). Although several approaches to characterize AFM tips exist, none of them provides a reliable and general technique easily applicable to all cases.

A first approach is the examination of tips with the transmission electron microscope (TEM) [82]. If Si_3N_4 tips are to be imaged by TEM, then a coating with Pt/Pd is needed in order to prevent charging, while silicon tips can be imaged without coating. Resolutions of the order of 1 nm can be attained.

Alternatively, once the process of image formation is known, given a surface of known profile employed as characterizer, the shape of the tip can be deduced from the artifacts in the image of the characterizer [83–89]. Such methods are affected by the uncertainty of characterizers profiles and by the poor reliability of mathematical reconstructions of imaging processes.

Two other methods of calibrating tip size and shape exploit the measurement by means of force–distance curves of some forces, namely the Coulomb force [21] and the double-layer force [69]. These are treated in Sections 6.1.2 and 6.3.2.

In order to eliminate the problem of the unknown shape of the tip, Ducker et al. [17] have used modified cantilevers with tips of known geometry. Such a technique, generally known as "colloidal probe technique", has been widely employed in force–distance curves acquisition. It is implemented by gluing at the end of a cantilever a sphere of radius between 2 and 10 μm by means of an epoxy resin. The radius of the sphere can be determined by electron microscopy and the mean roughness by AFM measurements. Fig. 16 shows a colloidal tip glued on a cantilever. A wide variety of materials has been employed: silica [17], TiO_2 [91], ZnS [62,92], gold [93], polystyrene [94] and others. When a colloidal probe is used, curves are often presented as a logarithmic plot of the ratio F/R_{eff} vs. the tip–sample separation. The advantage of this technique lies in the exact knowledge of the tip geometry, but it turns out to be disadvantageous when a high lateral resolution is needed. Thus, it cannot be effectively used in force–distance curves mapping.

5.3. Noise and systematic errors

Some general considerations on noise and systematic errors in force–distance curves acquisition are discussed here. Other specific artifacts are listed in Sections 2.4, 6.2.3, and 6.3.3.

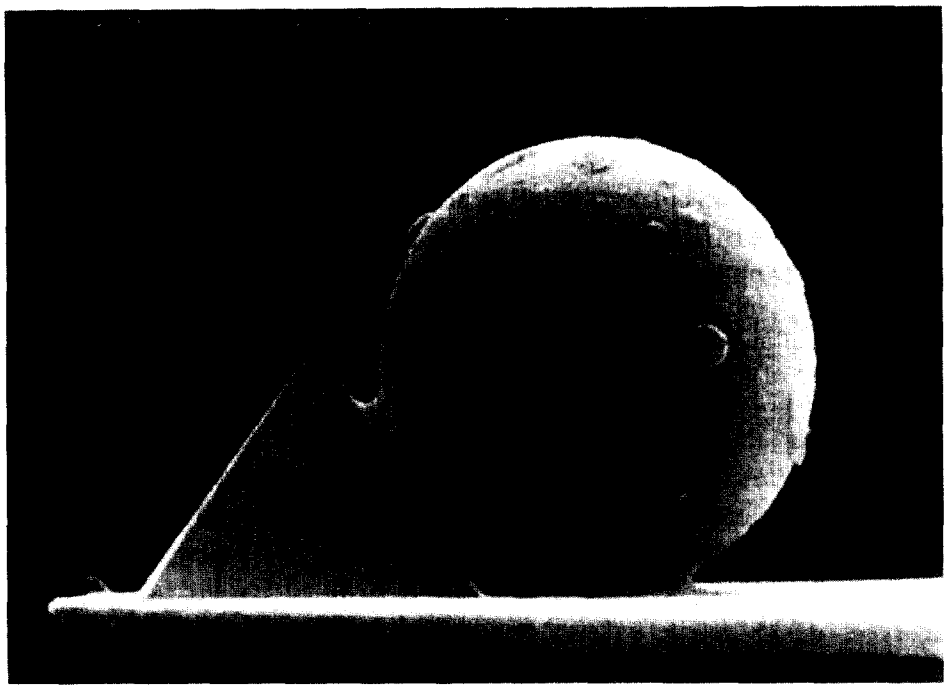

Fig. 16. A silica colloidal probe attached on a silicon nitride cantilever (reprinted with permission from [90]; copyright 1993 American Chemical Society).

The noise level of a force–distance curve, due to thermal agitation, mechanical vibrations of the apparatus and/or turbulence of the liquid environment, depends on the cantilever stiffness, and is usually ≤ 30 pN. Sources of the noise vary widely. Along the zero lines the noise is dominated by the thermal agitation, whereas along the contact lines, the thermal agitation is damped but mechanical vibrations are enhanced. In order to minimize the effects due to thermal drift, force–distance curves should be acquired with high scan rates but, over a certain threshold speed, dynamic effects begin to affect the measurement. This threshold value depends on the environment and can be roughly put at 1 μm/s in air [95]. Another obvious approach to minimize thermal noise consists in averaging several force–distance curves acquired on the same point and in the same conditions. This approach implies a careful superposition of curves.

The calculation of forces is affected by systematic errors in the estimation of the cantilever spring constant and tip radius. Since deflections are obtained from the contact line through Eq. (5.1), errors due to the sample compliance are possible, and are specific for each material and sample.

The estimation of distances is affected by systematic errors in piezo response and by piezo hysteresis and creep, which depend on the history of the piezo and on the scan rate.

Finally, digitalization errors must be considered. Siedle and Butt [68] have demonstrated that the cantilever oscillates due to its coupling to the discrete steps of the piezo via the liquid. This oscillation affects both the zero deflection and the determination of the jump-to-contact.

6. Measurement of forces

6.1. Forces in air

6.1.1. Meniscus force

Fig. 17 shows a force–displacement curve acquired on mica in air. Note that the hysteresis is very large. The jump-to-contact is rather small, while the jump-off-contact is quite large. Such a large adhesion is due to the meniscus force exerted by a thin layer of water vapor adsorbed on the sample surface, as schematically shown in Fig. 18. Such a layer barely affects attractive forces, whereas it prevents the tip from pulling off from the surface due to its high surface energy.

The Laplace pressure of the liquid meniscus is given by [15]:

$$P = \gamma_L\left(\frac{1}{r_1}+\frac{1}{r_2}\right) \cong \frac{\gamma_L}{r_{eff}}, \tag{6.1}$$

in which γ_L is the surface energy of the liquid and r_1 and r_2 are defined in Fig. 18. The Laplace pressure acts on the area [15]:

$$A \cong 2\pi R d \cong 2\pi R[r_{eff}(1+\cos\theta)+u_M], \tag{6.2}$$

in which d, θ, and u_M are given in panel (a) of Fig. 18. The surfaces are pulled together with a force

$$F \cong 2\pi R\gamma_L\left(1+\cos\theta+\frac{u_M}{r_{eff}}\right) \tag{6.3}$$

Eq. (6.3) is the contribution of the Laplace pressure to the adhesion. Recently, Gao [96] has calculated formulas for different tip geometries, showing that the force is decreased by about 20% for a conical tip.

Mate et al. [97] have studied the meniscus force exerted by a perfluoropolyether polymer liquid film on silicon. Fig. 19 shows a typical force–displacement curve on such films.

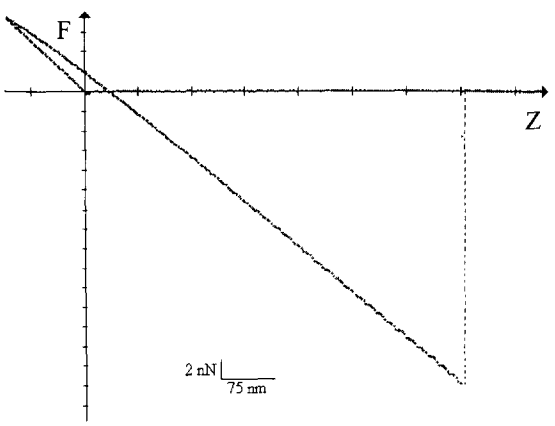

Fig. 17. Force–displacement curve on mica in air with a silicon nitride tip (R between 50 and 100 nm). The large jump-off-contact is due to the meniscus force. One can observe one of the most common artifacts in force–displacement curves, namely the inverse path effect (adapted from [128]).

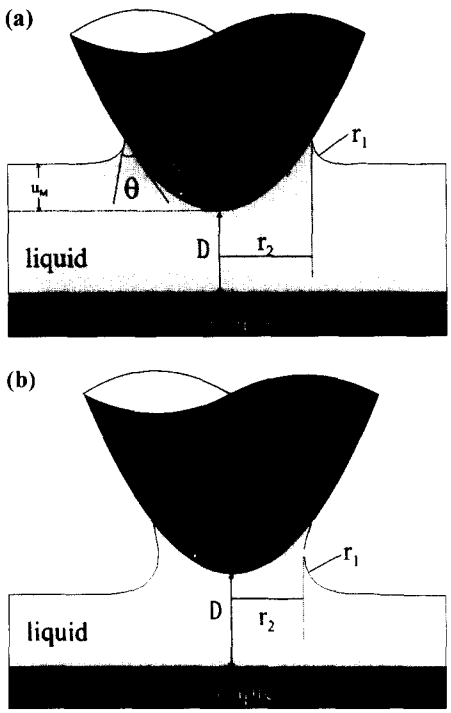

Fig. 18. The meniscus of the water vapor layer adsorbed on the sample surface onto a paraboidal tip, during approach (panel (a)) and retraction (panel (b)). R is the radius of curvature of the tip, D is the distance from the sample, u_M is the penetration depth in the liquid layer, r_1 and r_2 the two radii that define the liquid meniscus, θ the contact angle the liquid makes with the tip, and d the height of the meniscus relative to the end of the tip.

At great distances (right) the tip is far away from the surface and the deflection is zero. At 25 nm from the surface, while approaching the sample, the tip contacts the surface of the liquid film, that wicks up and forms a meniscus, resulting in an attractive force of 60 nN. After this first jump, the force on the tip is fairly constant, since the tip is penetrating through the liquid. When the tip contacts the

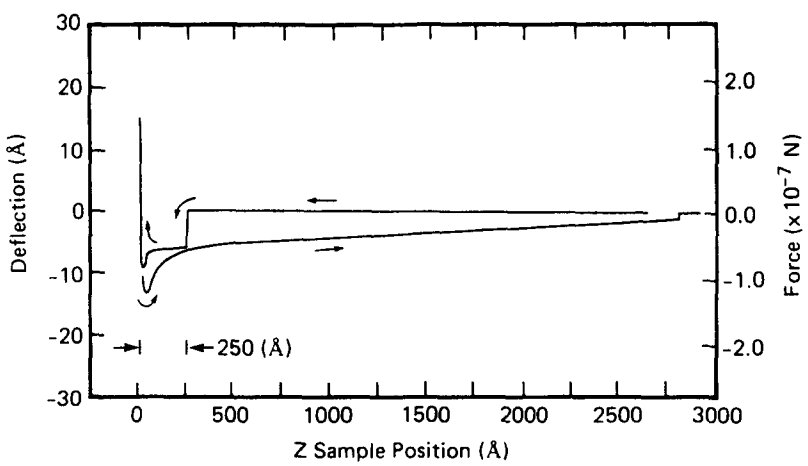

Fig. 19. Force–displacement curve on a perfluoropolyether polymer liquid film (reprinted with permission from [97]).

silicon, there is a second jump followed by the contact line. There are also two jumps-off-contact. The first jump, of 120 nN, occurs when the tip pulls off from silicon. The second, of $\cong$ 10 nN, when the tip detaches from the liquid film at $\cong$ 280 nm. In between, the force slowly decreases. The tip radius is approximately 230 nm. Force–distance curves allow to measure the effective meniscus radius r_{eff} and the thickness of the liquid film. Mate et al. have compared the thickness measured by the AFM with that measured by ellipsometry, showing that AFM always overestimates the film thickness, and that this is probably due to a thin film of liquid on the surface of the tip. Furthermore, the film thickness was acquired along a line of the sample in order to study the local liquid uniformity.

Thundat et al. [98] have observed the dependence of adhesion force on the relative humidity and have fitted the experimental data on meniscus force with the equation

$$F = -\frac{4\pi R\gamma_{\text{L}}\cos\theta}{[1 + D\log(H_{\text{r}})]/1.08\cos\theta}, \tag{6.4}$$

in which D is the tip–sample distance in nm and H_{r} is the relative humidity. With a rather small tip ($R = 15$ nm) the adhesion force is larger than 10 nN for $H_{\text{r}} > 60\%$ and becomes smaller than 5 nN for $H_{\text{r}} < 20\%$. Later on Thundat et al. [99] reproduced the same fit for a clean and a contaminated tip, showing that adhesion forces are larger for the contaminated tip (70 nN at $H_{\text{r}} > 50\%$ and 40 nN at $H_{\text{r}} < 10\%$). When rinsing the contaminated tips in acetone, methanol or methylene chloride, a slight decrease (< 10%) in adhesion force is observed. Such a decrease is enhanced by cleaning the tips in UV ozone, in which case the adhesion reaches the values of the clean tips (see also Ref. [100]).

The increase of adhesion force with increasing relative humidity has been studied for silicon nitride tips on SiO_2 substrates by Torii et al. [101].

Xu et al. [102] have studied the dependence of pull-off forces on relative humidity with Pt-covered tips on mica. The pull-off force is constant (2 nN) for $H_{\text{r}} < 20\%$, increases rapidly (8 nN) for $H_{\text{r}} = 20\%$, and then slowly decreases down to 3 nN for $H_{\text{r}} = 95\%$. They also verified that, depending on relative humidity, the pull-off force depends on contact time. At $H_{\text{r}} = 42\%$, the force goes from 87 nN for 1 ms contact time to 100 nN for a 10 s contact time. On the contrary, at $H_{\text{r}} = 12\%$, the pull-off force decreases with increasing contact time. Later on, Xu and Salmeron [103] have studied the effects of surface ions on the adhesion dependence on relative humidity.

Eastman and Zhu [104] have measured capillary forces between a mica substrate and surface modified tips, namely a Si_3N_4 tip, a gold coated tip and a paraffin coated tip. The results show that the capillary force, and hence the total adhesion force diminishes when the tip is coated with a hydrophobic material. The value of the capillary force is 92 nN for the gold coated tip and −31 nN for paraffin. The tip radius is about 100 nm. The authors do not obtain the same dependence of adhesion force as a function of relative humidity as Thundat et al., even for the Si_3N_4 tip. They claim that this disagreement is due to the hydrophobicity of their mica substrate. Since the substrate is hydrophobic, the height of the water layer is limited and does not increase with relative humidity so that the adhesion force stays the same at all values of relative humidity.

The different dependence of meniscus force on relative humidity for hydrophilic and for hydrophobic substrates has been addressed by Fujihira et al. [105]. The authors study the adhesion force on a Si substrate partially covered with a hydrocarbon monolayer. They show that the adhesion force is about 5 nN on the hydrophilic Si substrate and 1 nN on the hydrophobic hydrocarbon substrate, using the same tip. Furthermore the meniscus force on silicon increases from 20 nN at 10% relative humidity to 40 nN at 60% relative humidity, while it is about 20 nN for any relative humidity value on hydrocarbon. This

latter measurement was performed using a tip with a larger curvature radius. Hence capillary force allows to distinguish hydrophobic and hydrophilic materials. A similar set of measurements has been performed by Binggeli and Mate [106] on silicon, carbon and perfluoropolyether and by Olsson et al. [107] between a tungsten tip and a methylated SiO_2 surface. In this latter work, dynamic force–distance curves also are acquired, showing that, when the meniscus forms and the capillary force onsets, the amplitude of the oscillations abruptly goes from the free amplitude to an almost zero amplitude via a sharp and strong discontinuity. Dynamic force–distance curves are, therefore, more suitable for the detection of the distance of formation of menisci. This capability of dynamic force–displacement curves has been exploited by Friedenberg and Mate [108] in order to study the meniscus force exerted by different layers of polydimethylsiloxane (PDMS). Dynamic force–displacement curves are acquired varying the penetration distances in the PDMS layer and the thickness of the PDMS layer. The experimental results are in rather good agreement with theoretical predictions. Colchero et al. [109] have acquired force–displacement curves in the static and in the dynamic modes simultaneously. They have shown that static force–displacement curves reveal the liquid–solid interface, while the dynamic force–distance curve is able to reveal the presence of the liquid–vapor interface.

The study of capillary forces, of great importance also for the comprehension of the mechanisms involved in AFM imaging, has revealed the measurement of their effect as a useful technique for distinguishing materials with different hydrophobicity (see also Section 7). The different techniques reviewed here may be used effectively for the study of wetting properties of lubricants.

Water meniscus force exceeds all other forces, and in particular, it masks the Van der Waals force. Inserting $\gamma_L = 72\,\text{mJ m}^2$, $R = 30\,\text{nm}$ and $d = 2\,\text{nm}$ into Eq. (6.3) the meniscus force is approximately 30 nN, whereas the adhesion force due to Van der Waals attraction for normal materials is typically only 20 nN. In order to measure Van der Waals force and/or other surface forces, the meniscus force must be eliminated, either by removing the water layer by working in a low humidity environment (such as dry nitrogen or vacuum), or by dipping both sample and tip in a liquid environment [57].

6.1.2. Coulomb force

The measure of Coulomb forces until now has been of little interest, but it can be employed in order to study the tip shape. Hao et al. [21] have studied Coulomb forces by modeling the tip–sample system as a sphere on a flat surface and as a sphere-ended conical tip on a flat sample, as shown in Fig. 20. In the first case, the force is given by

$$F_0^{sp} = \pi\varepsilon_0 V^2 \frac{R}{D} \tag{6.5a}$$

for $R/D \gg 1$ and by

$$F_\infty^{sp} = \pi\varepsilon_0 V^2 \left(\frac{R}{D}\right)^2 \tag{6.5b}$$

for $R/D \ll 1$. V is the voltage difference between the tip and sample, R the radius of the sphere and D is the tip–sample distance.

In the case of a sphere-ended cone on a flat surface, the force may be calculated by replacing the equipotential conducting surfaces with their equivalent image charges. For small aperture angles

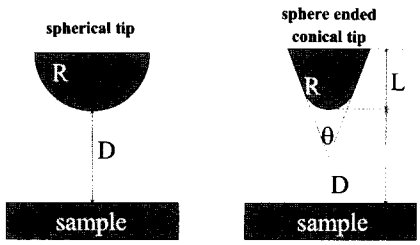

Fig. 20. The two tip–sample systems employed by Hao et al. [21] for the calculation of Coulomb force. R is the radius of the sphere, D the tip–sample distance, L the length of the sphere-ended conical tip, and θ the aperture angle.

($\theta \leq \pi/9$) the cone may be approximated by a charged line of constant charge density λ_0 given by

$$\lambda_0 = 4\pi\varepsilon_0 V\left[\ln\left(\frac{1+\cos\theta}{1-\cos\theta}\right)\right]^{-1}. \tag{6.6}$$

The resulting force is given by

$$F^c \cong \frac{\lambda_0^2}{4\pi\varepsilon_0}\ln\left(\frac{L}{4D}\right), \tag{6.7}$$

in which L is the cone length ($L \ll D \ll R$).

Hao et al. have measured the Coulomb forces between a tungsten tip and graphite. By fitting the experimental data, the authors have been able to determine the curvature radius of different tips (270 and 27.5 nm, in good agreement with scanning electron microscope measurements). Furthermore, they have shown that Eq. (6.5a) fits well the measured forces at small tip–sample separations, whereas at larger distances Eq. (6.7) is needed (see Fig. 21). The disagreement between experimental data and Eq. (6.5b) increases with decreasing tip dimensions.

Burnham et al. [110] have studied another kind of Coulomb-like force which arises from the patch charges distribution on the tip and sample, i.e., from regions of different surface charge density

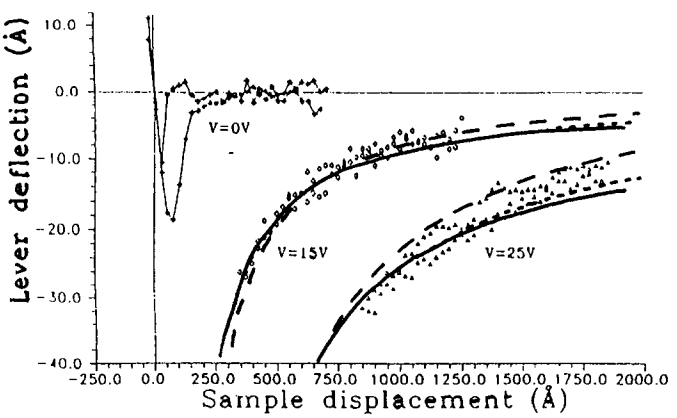

Fig. 21. Force–displacement curves on graphite. Coulomb forces at $V=0$ V, $V=15$ V and $V=25$ V are displayed. The theoretical results for the sphere-ended conical tip (continuous line), the spherical tip (— — —) and the simple R/D approximation (- - -) are also shown (reprinted with permission from [21]; copyright 1991 American Vacuum Society).

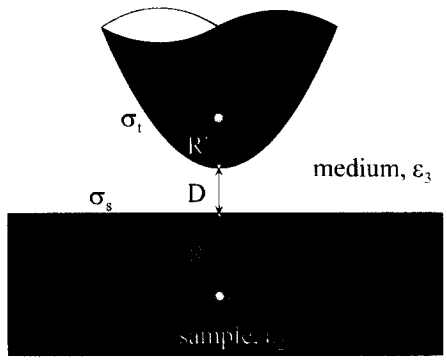

Fig. 22. The tip–sample system employed by Burnham et al. [110] for the calculation of patch charges force. The tip and sample surface charges are represented by two image charges Q_t and Q_s placed at the distances R' and R''. D is the tip–sample distance. ε_1, ε_2 and ε_3 are the dielectric constants of the tip, the sample, and the medium, respectively.

interacting via a long range force law. The patch charges distribution can be modeled by means of the image charge method, as shown in Fig. 22. Consider a spherical tip of radius R on a flat sample with surface charge densities σ_t and σ_s represented by an image charge Q_t at a distance R' inside the tip and by an image charge Q_s at a distance R'' inside the sample. If $R \gg R' \gg D$ and $R'' \gg D, R, R'$, then the force is given by

$$4\pi\varepsilon_0 F = -\frac{Q_t}{4R'^2}\left(1-\frac{2D}{R'}\right)\left(\frac{\varepsilon_2-\varepsilon_3}{\varepsilon_2+\varepsilon_3}\right)+\frac{Q_tQ_s}{RR''}\left(1-\frac{2R'}{R}-\frac{4D}{R}\right)\left(\frac{\varepsilon_1-\varepsilon_3}{\varepsilon_1+\varepsilon_3}\right)\left(\frac{\varepsilon_2-\varepsilon_3}{\varepsilon_2+\varepsilon_3}\right), \tag{6.8}$$

where ε_1 and ε_2 are the dielectric constants of the tip and sample and ε_3 is the dielectric constant of the medium.

Patch charge densities are negligible compared to double-layer charge densities (see Section 6.3.1). The patch charge force is larger than the Van der Waals force and has the same dependence on the dielectric constants. Note that, if the geometrical constants R and R' are much larger than D, Eq. (6.8) becomes effectively independent on the distance. There is evidence that this occurs when the ratio of the probe radius to the distance is 10^3.

This kind of force has been measured by Burnham et al. [110] and by Agraït et al. [59]. This latter experiment has been performed in vacuum, at liquid helium temperature (4.2 K), using a gold tip on a gold sample. The presence of contaminants can therefore be excluded, allowing the different forces to be distinguished from each other.

6.2. Van der Waals force

6.2.1. Theory

In the theoretical subsections only the issues necessary to the comprehension of the experimental results are reviewed. The discussion is based on the derivations given in [15, 111–113].

The Van der Waals force between atoms and/or molecules is the sum of three different forces, all proportional to $1/r^6$ (r is the distance between the atoms or molecules). These forces are: (a) the orientation or Keesom force, (b) the induction or Debye force, and (c) the dispersion or London force.

(a) The Keesom force is the angle–averaged dipole–dipole interaction between two atoms or molecules and its potential is [15]:

$$w_K(r) = -\frac{u_1^2 u_2^2}{3(4\pi\varepsilon_0\varepsilon)^2 k_B T r^6} = -\frac{C_K}{r^6}, \tag{6.9}$$

where u_1 and u_2 are the dipole moments of the molecules, ε the dielectric constant of the medium, k_B the Boltzmann constant and T is the temperature. Eq. (6.9) holds for $k_B T > u_1 u_2/4\pi\varepsilon_0\varepsilon r^3$[15].

(b) The Debye force is the angle-averaged dipole-induced dipole interaction between two atoms or molecules:

$$w_D(r) = -\frac{u_1^2\alpha_{02} + u_2^2\alpha_{01}}{(4\pi\varepsilon_0\varepsilon)^2 r^6} = -\frac{C_D}{r^6} \tag{6.10}$$

in which α_{01} and α_{02} are the electronic polarizabilities of the molecules. Eq. (6.9) may be obtained from Eq. (6.10) by replacing the electronic polarizability α_0 with the orientation polarizability $\alpha = u^2/3k_B T$.

(c) The dispersion force is the most important contribution to Van der Waals force, because it acts between all molecules or atoms, on a distance that ranges from more than 10 nm down to 2 Å. It may be attractive or repulsive. The dispersion force is the instantaneous dipole-induced dipole interaction, and is of quantum-mechanical nature. An expression of this force has been calculated in 1930 by London [114]. The corresponding potential is

$$w_L(r) = -\frac{3}{2}\frac{\alpha_{01}\alpha_{02}}{(4\pi\varepsilon_0)^2 r^6}\frac{(h\nu_1)(h\nu_2)}{h\nu_1 + h\nu_2} = -\frac{C_L}{r^6}, \tag{6.11}$$

in which $h\nu_1$ and $h\nu_2$ are the first ionization potentials of the molecules and h is the Planck constant.

Thus the total Van der Waals potential can be written as

$$w_{VdW}(r) = -\frac{C_K + C_D + C_L}{r^6} = -\frac{1}{(4\pi\varepsilon_0)^2 r^6}\left[(u_1^2\alpha_{02} + u_2^2\alpha_{01}) + \frac{u_1^2 u_2^2}{3k_B T} + \frac{3\alpha_{01}\alpha_{02}}{2}\frac{(h\nu_1)(h\nu_2)}{h\nu_1 + h\nu_2}\right]. \tag{6.12}$$

In 1963 McLachlan [115] presented a generalized theory of the Van der Waals force between infinite media 1 and 2 separated by a medium 3 in the form:

$$w_{VdW}(r) = -\frac{6k_B T}{(4\pi\varepsilon_0)^2 r^6}\sum_{n=0}^{\infty}{}' \frac{\alpha_1(i\nu_n)\alpha_2(i\nu_n)}{\varepsilon_3^2(i\nu_n)}, \tag{6.13}$$

in which the 0-term of the sum has to be multiplied by 1/2, $\alpha_1(i\nu_n)$ and $\alpha_2(i\nu_n)$ are the polarizabilities of molecules, and $\varepsilon_3(i\nu_n)$ is the dielectric constant of the medium at the frequencies $i\nu_n = 2ni\pi k_B T/h$. The total polarizability in vacuum at the frequency $i\nu_n$ is [116]:

$$\alpha(i\nu_n) = \frac{\alpha_0}{1 + (\nu_n/\nu_1)^2} + \frac{u^2}{3k_B T(1 + \nu_n/\nu_{rot})}, \tag{6.14}$$

in which ν_1 is the ionization frequency and ν_{rot} is the average rotational relaxation frequency.

The first term ($n = 0$) of Eq. (6.13) is:

$$(w_{\mathrm{VdW}}(r))_{\nu=0} = -\frac{3k_{\mathrm{B}}T}{(4\pi\varepsilon_0)^2 r^6}\alpha_1(0)\alpha_2(0) = -\frac{3k_{\mathrm{B}}T}{(4\pi\varepsilon_0)^2 r^6}\left(\frac{u_1^2}{3k_{\mathrm{B}}T} + \alpha_{01}\right)\left(\frac{u_2^2}{3k_{\mathrm{B}}T} + \alpha_{02}\right). \tag{6.15}$$

It contains the Keesom and Debye energies. This term acts only between polar molecules and is called polar or entropic contribution.

The term at non-zero frequencies is called dispersion contribution. This sum entails the calculation of $\alpha(\mathrm{i}\nu_n)$ at the discrete frequencies ν_n and hence the knowledge of the absorption spectrum of the materials over the entire real frequency range, $0 \leq \nu < \infty$. With a few exceptions, only partial data are available, and some approximate methods have been developed, such as the Ninham and Parsegian method [117]. In this method $\alpha(\mathrm{i}\nu_n)$ is considered as determined only by electronic polarizability, since, at normal temperatures, the first frequency $\nu_{n=1} \cong 4 \times 10^{13}$ Hz is already much greater than $\nu_{\mathrm{rot}} \cong 10^{11}$ Hz. Further, since all the frequencies ν_n are very close in the UV region, the sum in Eq. (6.13) can be replaced [15] by an integration over $\mathrm{d}n = (h/2\pi k_{\mathrm{B}}T)\,\mathrm{d}\nu$:

$$(w_{\mathrm{VdW}}(r))_{\nu>0} = -\frac{3h}{(4\pi\varepsilon_0)^2\pi r^6}\int_{\nu_1}^{\infty}\alpha_1(\mathrm{i}\nu)\alpha_2(\mathrm{i}\nu)\,\mathrm{d}\nu \cong -\frac{3}{2}\frac{\alpha_{01}\alpha_{02}}{(4\pi\varepsilon_0)^2 r^6}\frac{h\nu_1\nu_2}{\nu_1+\nu_2}, \tag{6.16}$$

yielding Eq. (6.11).

McLachlan theory allows to calculate dispersion forces also for atoms or molecules of dielectric constant ε_1 in a medium of dielectric constant ε_3. In this case it is necessary to consider the excess polarizability of the molecule of radius R_{m} given by the Clausius–Mossotti equation [118]:

$$\alpha_{\mathrm{exc}}(\nu) = 4\pi\varepsilon_0\varepsilon_3(\nu)\frac{\varepsilon_1(\nu)-\varepsilon_3(\nu)}{\varepsilon_1(\nu)+2\varepsilon_3(\nu)}R_{\mathrm{m}}^3. \tag{6.17}$$

Inserting Eq. (6.17) into Eqs. (6.15) and (6.16) the total Van der Waals interaction, Eq. (6.13), becomes the sum of two terms given by

$$(w_{\mathrm{VdW}}(r))_{\nu=0} = -\frac{3k_{\mathrm{B}}TR_{\mathrm{m1}}^3R_{\mathrm{m2}}^3}{r^6}\left(\frac{\varepsilon_1(0)-\varepsilon_3(0)}{\varepsilon_1(0)+2\varepsilon_3(0)}\right)\left(\frac{\varepsilon_2(0)-\varepsilon_3(0)}{\varepsilon_2(0)+2\varepsilon_3(0)}\right), \tag{6.18a}$$

and

$$(w_{\mathrm{VdW}}(r))_{\nu>0} = -\frac{3hR_{\mathrm{m1}}^3R_{\mathrm{m2}}^3}{\pi r^6}\int_0^{\infty}\frac{\varepsilon_1(\mathrm{i}\nu)-\varepsilon_3(\mathrm{i}\nu)}{\varepsilon_1(\mathrm{i}\nu)+2\varepsilon_3(\mathrm{i}\nu)}\frac{\varepsilon_2(\mathrm{i}\nu)-\varepsilon_3(\mathrm{i}\nu)}{\varepsilon_2(\mathrm{i}\nu)+2\varepsilon_3(\mathrm{i}\nu)}\,\mathrm{d}\nu. \tag{6.18b}$$

If the dielectric medium has one strong absorption peak at the frequency ν_e (that is usually different from the frequency ν_1 of the isolated molecule), $\varepsilon(\nu)$ can be written as

$$\varepsilon(\nu) = 1 + \frac{n^2-1}{1+(\nu/\nu_e)^2}, \tag{6.19}$$

in which n is the refractive index. Substituting in Eq. (6.18b) we obtain:

$$(w_{\mathrm{VdW}}(r))_{\nu>0} = -\frac{\sqrt{3}}{2}\frac{h\nu_eR_{\mathrm{m1}}^3R_{\mathrm{m2}}^3}{r^6}\frac{(n_1^2-n_3^2)(n_2^2-n_3^2)}{\sqrt{(n_1^2+2n_3^2)}\sqrt{(n_2^2+2n_3^2)}\left[\sqrt{(n_1^2+2n_3^2)}+\sqrt{(n_2^2+2n_3^2)}\right]}. \tag{6.20}$$

Hence the total Van der Waals force between two identical molecules is:

$$w_{\mathrm{VdW}}(r) = -\left[3k_{\mathrm{B}}T\left(\frac{\varepsilon_1(0)-\varepsilon_3(0)}{\varepsilon_1(0)+2\varepsilon_3(0)}\right)^2 + \frac{\sqrt{3}}{4}h\nu_e\frac{(n_1^2-n_3^2)^2}{\sqrt{(n_1^2+2n_3^2)^3}}\frac{R_{m1}^3}{r^6}\right]. \tag{6.21}$$

From the above equations, some conclusions about Van der Waals force can be drawn.

(1) Whenever $h\nu_e \gg k_{\mathrm{B}}T$, as in vacuum, the dispersion term is larger than the polar term.

(2) In a medium, the Van der Waals force is greatly reduced.

(3) The Van der Waals dispersion (polar) force in a medium may be attractive, vanishing or repulsive. It is repulsive whenever $n_3(\varepsilon_3)$ is intermediate between $n_1(\varepsilon_1)$ and $n_2(\varepsilon_2)$. It vanishes if $n_3(\varepsilon_3)$ matches $n_1(\varepsilon_1)$ or $n_2(\varepsilon_2)$. The force between two identical molecules is always attractive.

Some other features of Van der Waals force are noteworthy.

(1) The Van der Waals force is anisotropic. As a matter of fact, the polarizabilities of the majority of molecules are anisotropic, i.e., they have different values for different molecular directions. One of the consequences of the anisotropy of polarizabilities is that the dispersion force between two molecules depends on their mutual orientation. This effect is important in solids and liquid crystals, where the thermal motion is reduced.

(2) The Van der Waals force is non-additive. The force between two molecules is affected by other molecules nearby, since they behave like a medium.

(3) The Van der Waals force is affected by retardation effects. This effect is described in detail in [119] and only a qualitative description is given here. When two atoms are far away, the time taken by the field of the first atom to reach the second one and come back may be comparable to the period of the fluctuating dipole. In this case, the reflected field finds that the orientation of the first dipole is now different. At large separation, because of the retardation effect, the power law index increases by unity. Thus, with increasing separation, the dispersion force begins to decay as $-1/r^7$ at distances larger than 100 nm. Such retardation effects turn out to be very important in liquids, where the speed of light is low, and the effect appears at distances smaller than 5 nm. Only the dispersion term is retarded, whereas the polar one is non-retarded at all distances. In the presence of a medium, the Van der Waals force has three distance regimes. At small distances the force law is $1/r^6$. At intermediate distances, where the retarded dispersion dominates the Van der Waals force, the force law is $1/r^7$. At larger distances, the polar term, that is always non-retarded, turns out to be dominant and the force law is again $1/r^6$.

In order to model the interactions taking place in AFM, it is necessary to study interactions between surfaces, rather than between atoms or molecules. Let us begin with a pair potential in the form $w(r) = -C/r^n$. Assuming that the potential is additive, the interaction energies between macroscopic bodies may be obtained via integration. In the case of two interacting spheres of radius R_1 and R_2 at the distance D, the force $F(D)$ can be obtained by integrating over small circular sections of surface $2\pi x\,\mathrm{d}x$ on both spheres [120] (Fig. 23):

$$F(D) = \int_D^{\infty} 2\pi x\,\mathrm{d}x f(Z), \tag{6.22}$$

in which $f(Z)$ is the normal force per unit area. From the Chord theorem $x^2 \cong 2R_1z_1 = 2R_2z_2$ and

$$Z = D + z_1 + z_2 = D + \frac{x^2}{2}\left(\frac{1}{R_1}+\frac{1}{R_2}\right), \tag{6.23}$$

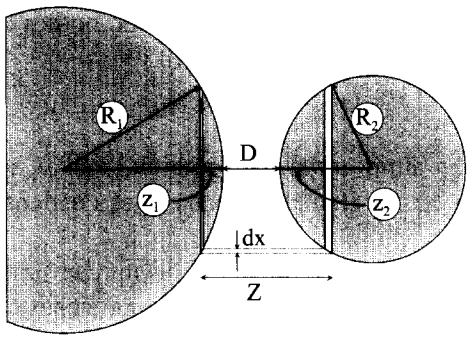

Fig. 23. Geometry employed in the Derjaguin approximation. The two spheres of radii R_1 and R_2 are at a distance D. The force is integrated over small circular sections of radius x and height dx at distances $Z = D + z_1 + z_2$.

and hence

$$dZ = \left(\frac{1}{R_1} + \frac{1}{R_2}\right) x\,dx. \tag{6.24}$$

Finally, the force is given by

$$F(D) \cong \int_D^{\infty} 2\pi \frac{R_1 R_2}{R_2 + R_2} f(Z)\,dZ = 2\pi \frac{R_1 R_2}{R_1 + R_2} W(D), \tag{6.25}$$

in which $W(D)$ is the interaction potential between two flat surfaces.

Eq. (6.25) is known as the Derjaguin approximation, and holds whenever the interaction range and the separation D are much smaller than R_1 and R_2. It should be emphasized that in Eq. (6.25) it is not necessary to specify explicitly the type of interaction $f(Z)$. This fact implies that Eq. (6.25) is correct for any kind of force, whether attractive, repulsive, or oscillating. From the Derjaguin approximation, by putting $R_2 \gg R_1$, it is possible to obtain the force between a sphere and a flat surface:

$$F(D) = 2\pi R_1 W(D). \tag{6.26}$$

Van der Waals energies between macroscopic bodies in vacuum may be computed via integration only in the approximation that the Van der Waals force is considered additive and non-retarded. The interaction laws obtained via integration are listed in Table 1 for the most common geometries.

Table 1
Van der Waals interactions for the most common geometries. R is the radius of spheres, D the distance between the interacting bodies, and A the Hamaker constant.

Geometry	Interaction law
Two spheres	$W = -\frac{A}{6D}\frac{R_1 R_2}{R_1 + R_2}$
Sphere-flat surface	$W = -\frac{AR}{6D}$
Two flat surfaces	$W = -\frac{A}{12\pi D^2}$ per unit area

All interaction laws depend on geometrical features of the bodies and on the Hamaker constant A, which includes all physico-chemical information [121]:

$$A = \pi^2 C \rho_1 \rho_2, \tag{6.27}$$

in which C is the constant in the atom–atom pair potential and ρ_1 and ρ_2 are the number of atoms per unit volume. Typical values of the Hamaker constant of condensed phases in vacuum are about 10^{-19} J.

In the following, we will show how the Hamaker constant can be calculated. However, in order to determine Hamaker constants from measured curves, two approaches can be followed. The first method consists in fitting one of the force laws listed in Table 1 to the attractive part of the force–distance curve. This procedure can be somewhat difficult due to the short interaction range. The second method adapts Eq. (1.9) to the Van der Waals force and to the appropriate geometry. Thus, the Hamaker constant can be determined from the jump-to-contact force.

For $n = 2$ and $C = AR/6$, i.e., for a sphere on a flat surface, Eq. (1.9) becomes

$$\begin{aligned} (\delta_c)_{jtc} &= \frac{1}{2}\sqrt[3]{\frac{AR}{3\beta^2 k_c}} \\ D_{jtc} &= 2\beta(\delta_c)_{jtc} = \sqrt[3]{\frac{\beta AR}{3k_c}}. \end{aligned} \tag{6.28}$$

Eq. (6.28) permits to calculate A and R from the measured $(\delta_c)_{jtc}$ and D_{jtc} once β and k_c are known.

By assuming the additivity of the Van der Waals force, the influence of nearby atoms on the couple of interacting atoms is neglected, thus introducing large errors in the calculation of the Hamaker constant. To circumvent this problem, Lifshitz [122] presented an alternative approach in which each body is treated as a continuum with certain dielectric properties. This approach automatically incorporates many-body effects which are neglected in the microscopic approach. All the expressions in Table 1 remain valid. Only the computation of the Hamaker constant changes.

In Lifshitz theory, the Hamaker constant for the interaction of media 1 and 2 across the medium 3 may be expressed in terms of McLachlan equation (6.13) as

$$\begin{aligned} A = \pi^2 C \rho_1 \rho_2 &= \frac{6\pi^2 k_B T \rho_1 \rho_2}{(4\pi\varepsilon_0)^2} \sum_0^\infty \frac{\alpha_1(i\nu_n)\alpha_2(i\nu_n)}{\varepsilon_3^2(i\nu_n)} \\ &= \frac{3}{2} k_B T \sum_0^\infty \left[\frac{\varepsilon_1(i\nu_n) - \varepsilon_3(i\nu_n)}{\varepsilon_1(i\nu_n) + \varepsilon_3(i\nu_n)}\right]\left[\frac{\varepsilon_2(i\nu_n) - \varepsilon_3(i\nu_n)}{\varepsilon_2(i\nu_n) + \varepsilon_3(i\nu_n)}\right] \end{aligned} \tag{6.29}$$

Substituting the sum with an integration, as already done in Eq. (6.16), yields

$$A \cong \frac{3}{4} k_B T \frac{\varepsilon_1 - \varepsilon_3}{\varepsilon_1 + \varepsilon_3}\frac{\varepsilon_2 - \varepsilon_3}{\varepsilon_2 + \varepsilon_3} + \frac{3h}{4\pi}\int_{\nu_1}^\infty \frac{\varepsilon_1(i\nu_n) - \varepsilon_3(i\nu_n)}{\varepsilon_1(i\nu_n) + \varepsilon_3(i\nu_n)}\frac{\varepsilon_2(i\nu_n) - \varepsilon_3(i\nu_n)}{\varepsilon_2(i\nu_n) + \varepsilon_3(i\nu_n)} d\nu. \tag{6.30}$$

The first term is the zero frequency contribution and includes Debye and Keesom forces. The second term is the dispersion contribution.

In order to compute Hamaker constants it is necessary to know the dependence of the dielectric constant on the frequency. Hough and White [113], following Ninham and Parsegian [117], have

approximated $\varepsilon(i\nu)$ in the form:

$$\varepsilon(i\nu) = 1 + \frac{C_{IR}}{1+\nu/\nu_{rot}} + \frac{C_{UV}}{1+\nu^2/\nu_e^2}, \quad C_{IR} \cong \varepsilon_0 - n^2; \text{ and } C_{UV} \cong n^2 - 1. \tag{6.31}$$

Such an approximation holds for materials with sharp, non-overlapping absorption peaks. The infrared term can be neglected when $\varepsilon_0 \cong n^2$. Using the Hough and White approximation, and neglecting the infrared term, Eq. (6.30) becomes

$$\begin{aligned} A_{TOT} &= A_{\nu=0} + A_{\nu>0} \\ &\cong \frac{3}{4}k_B T \frac{\varepsilon_1-\varepsilon_3}{\varepsilon_1+\varepsilon_3}\frac{\varepsilon_2-\varepsilon_3}{\varepsilon_2+\varepsilon_3} + \frac{3h\nu_e}{8\sqrt{2}} \frac{(n_1^2-n_3^2)(n_2^2-n_3^2)}{\sqrt{n_1^2+n_3^2}\sqrt{n_2^2+n_3^2}\left[\sqrt{n_1^2+n_3^2}+\sqrt{n_2^2+n_3^2}\right]} \end{aligned} \tag{6.32}$$

For two identical media ($\varepsilon_1 = \varepsilon_2 \neq \varepsilon_3, n_1 = n_2 \neq n_3$), Eq. (6.32) becomes

$$A \cong \frac{3}{4}k_B T\left(\frac{\varepsilon_1-\varepsilon_3}{\varepsilon_1+\varepsilon_3}\right)^2 + \frac{3h\nu_e}{16\sqrt{2}} \frac{(n_1^2-n_3^2)^2}{\sqrt{(n_1^2+n_3^2)^3}}. \tag{6.33}$$

Eq. (6.33) exhibits three interesting aspects.

1. The Van der Waals force between two identical bodies in a medium is always attractive (A is positive), whereas the force between two different bodies may be attractive or repulsive.
2. The Van der Waals force between any two condensed bodies in vacuum or in air ($\varepsilon_3 = 1$ and $n_3 = 1$) is always attractive.
3. The polar term cannot be larger than $(3/4)k_BT$, which is about 3.6×10^{-21} J at $T = 300$ K.

Bergström [112] has evaluated the accuracy of Ninham–Parsegian and Hough–White approximations, and the importance of the infrared contribution.

For interactions between conductive bodies such as metals, Eq. (6.33) cannot be applied, since ε is infinite. For two metals in vacuum the Hamaker constant is [15]:

$$A \cong \frac{3}{8\sqrt{2}} h \frac{\nu_{e1}\nu_{e2}}{\nu_{e1}+\nu_{e2}} \cong 4 \cdot 10^{-19}\,\text{J}, \tag{6.34}$$

in which ν_{e1} and ν_{e2} are the plasma frequencies of the two metals.

At large separations, the retardation effect becomes important, and a retarded Hamaker constant A_r has to be considered [111, 123]. The entropic Hamaker constant scales as k_BT and the non-retarded Hamaker constant scales as $h\nu_e$. Similarly, the retarded Hamaker constant scales as hc (c is the speed of light). The characteristic wavelength

$$\lambda_{132} = 6\pi A_r/A \tag{6.35}$$

indicates the onset of retardation. A_r depends on low-frequency indices of refraction n^*. It is negative for $n_1^* < n_3^* < n_2^*$ and positive for $n_3^* < n_1^*$ or $n_3^* > n_2^*$. Anyway, since there is no correlation between n^* and n, the Van der Waals force may be attractive at small distances and repulsive at great distances, and vice versa.

Hamaker constants for materials commonly used in AFM are listed in Table 2. Usual AFM tips are made out of silicon nitride or silicon, one common substrate is mica and the colloidal probes are usually silica spheres. A complete list of Hamaker constants calculated with the full Hough and White

Table 2
Hamaker constants ($\times 10^{-20}$ J) through air (italic values) or water (bold values) for most common AFM materials as calculated by (a) Bergström [112] using the Hough and White expression and the Prieve-Russel representation for water, (b) Bergström using the approximate expressions Eqs. (6.31) or (6.32), (c) Senden and Drummond [124] using Hough and White method and Gingell-Parsegian representation of water.

	Si_3N_4	silicon	mica	silica
Si_3N_4	*16.7*[a], *16.2*[b], **4.85**[a], **6.07**[c]	*16.84*[c], **6.75**[c]	*12.8*[a], **2.45**[a], **3.40**[c]	*10.8*[a], **1.17**[a], **1.9**[c]
silicon		*18.65*[c], **9.75**[c]	*12.63*[c], **3.48**[c]	*10.26*[c], **1.92**[c]
mica			*9.86*[a], *9.64*[b], **1.34**[a], **2.01**[c]	*8.01*[a], **0.69**[a], **1.19**[c]
silica				*6.5*[a], *6.39*[b], **0.46**[a], **0.77**[c]

approximation is given by Bergström [112]. In Table 2 the values calculated by Senden and Drummond [124] are also included. In the case of water as a medium, Hamaker constants may differ up to 67% due to the different models of water used in the calculations. The exclusion of the infrared term brings an error of about 2%.

6.2.2. Experimental results

At the very beginning of the study of tip–sample interactions with the AFM, the importance of capillary force had not been realized, and some researchers pretended to measure Van der Waals force and sample surface energies in air. Weisenhorn et al. [57] were the first to realize the necessity of working in water if one would like to perform measurement in absence of capillary force.

Nevertheless, a lot of measurements have been performed in dry nitrogen. There are some common drawbacks affecting these initial experiments.

1. The tips are rather large, so that the interaction is averaged over a large area and details are lost. Furthermore, any asperity on the tip turns to determine the interaction.
2. Surface contaminants are likely to store up on a very large tip and cannot be easily eliminated.
3. Maugis theory was still unknown, so that the elastic contact is modeled according to the JKR theory or according to the DMT analysis.

The previous considerations do not hold for the study of Eastman and Zhu [104] and for that of Hutter and Bechhoefer [95]. The work of Eastman and Zhu [104] is focused on determining separately the contributions of capillary and Van der Waals forces (see Section 6.1). The work of Hutter and Bechhoefer [95] is the first measurement of the transition from the non-retarded regime to the retarded regime of the Van der Waals force. The power law is -2 (-2.19 is the experimental value) for distances smaller than 16 nm and increases to -3 (-2.92) for distances larger than 20 nm. The exponent -2 is characteristic for the interaction between a sphere and a plane. The increased exponent at larger distances is due to the retardation effect. Table 3 contains a list of measurements performed in air or in dry nitrogen. Even if measured quantities have a large uncertainty, they often show a valid trend with surface energies.

Fig. 24 shows a curve acquired on mica in water. Both attractive and adhesion forces become nearly 10 times smaller than in air and the Van der Waals force makes the greatest contribution to adhesion since the meniscus has been removed. Also the pull-off distance is reduced by a factor of 10.

Table 4 provides a list of measurements in water or water solutions.

Table 3
Measured attractive force F_{attr}, adhesion force F_{ad}, and surface energy γ_s for experiments in air or in dry nitrogen: (a) The tip material and dimensions are unknown in this work, (b) The tips are colloidal particles, (c) PTFE = poly-tetrafluoroethylene.

Ref.	Tip radius (nm)	Tip material/Medium/Sample	Measured (calculated)		
			F_{attr} (nN)	γ_s (mJ/m^2)	F_{ad} (nN)
[18]	270	SiO_2/air/graphite, LiF			100, 160
[57]	[a]	[a]/air/mica			400
[44]	50–100	tungsten/dry N_2/silicon			50
[42]	100–200	tungsten/dry N_2/gold	$\cong$ 750	270–540	$\cong$ 750
		tungsten/dry N_2/graphite	$\cong$ 140		$\cong$ 250
[125]	2500	tungsten/dry N_2/mica	230 ± 30		330 ± 150
		/graphite	140 ± 90		220 ± 120
		/PTEE[c]	2 ± 2	21 ± 2 (18)	5 ± 5
	2000	/stearic acid	17 ± 11	24 ± 2 (21)	35 ± 11
		/Al_2O_3	85 ± 25	41 ± 4 (45)	100 ± 25
	3000	/trifluorostearic acid	5 ± 4	23 ± 2 (20)	20 ± 8
[55]	200	Ni/dry N_2/Au	$\cong$ 3000		4000–5000
[21]	270, 27.5	tungsten/air/graphite		15–40, 60–80	$\cong$ 24, $\cong$ 8
[95]	40	Si_3N_4/air/mica	0.6		
[126]	20–50	Si_3N_4/air/glass			300
[104]	100	Si_3N_4/air/mica			192 (184)
		gold/air/mica			51 (48)
		paraffin/air/mica			17 (16)
[62]	5000[b]	iron oxide/air/silica		3 (163)	

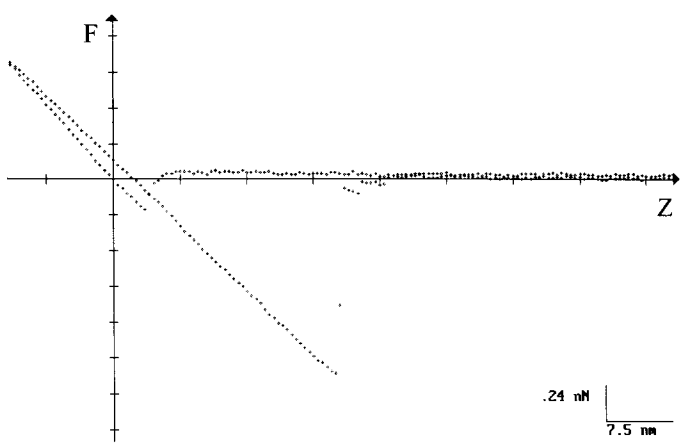

Fig. 24. Force–displacement curve on mica in water with a silicon nitride tip (R between 50 and 100 nm). Note the inverse path effect on the contact lines (adapted from [128]).

Table 4
Measured attractive force F_{attr}, adhesion force F_{ad}, and Hamaker constants A for experiments in water. Tips labeled with (a) are colloidal probes.

Ref.	Tip radius (nm)	Tip material/Medium/Sample	Measured (calculated)		
			A ($\times 10^{-19}$ J)	F_{attr} (nN)	F_{ad} (nN)
[91]	9000[a]	TiO_2/TiO_2	0.6 ± 0.2		
[93]	3300[a], 100[a]	Au/Au	2.5, 2.5		
[69]	160-260[a]	Si_3N_4/Si_3N_4	0.32–2.2 (0.61)		
	130-280[a]	Si_3N_4/mica	0.06–1.7 (0.34)		
[127]	30–50	Si_3N_4/stearyl amine			3–5
		/stearic acid			1–1.5
		/stearyl amide			$\cong 0.5$
[48]	20	Si_3N_4/mica			0.8–1.4
		/lysozyme			0.2–0.4
[77]	220[a]	Si_3N_4/Si_3N_4		1.3	
[101]	50	Si_3N_4/SiO_2			44 (45)
		$/Si_3N_4$			50
[62]	5000[a]	iron oxide/silica			(γ in mJ/m^2) 0.3 (51)
[128]	$\cong 50$	Si_3N_4/mica		0.24	1.4
		Si_3N_4/stearic acid		1–3	
		Si_3N_4/Au		0.4	10

Hartmann [123, 129] has calculated, according to Lifshitz theory, the Van der Waals force in different liquids (H_2O, glycerol, CCl_4, H_2O_2, formamide, and glycol) verifying that the force is reduced by a 10-fold factor (or 100 for the last three liquids). For CCl_4 the Van der Waals force is attractive at any distance. For formamide and glycerol it is repulsive, because their dielectric functions exhibit a rather strong polar contribution. For H_2O, H_2O_2, and glycol there is a transition point from the attractive to the repulsive regime between 100 and 1000 nm. This effect is due to the retardation of the dispersion contribution that becomes smaller than the polar repulsive term. Unfortunately, the Van der Waals force becomes very small at such distances. Hence it turns out to be very difficult to detect such inversion points. In Fig. 25 a force–displacement curve acquired on mica in formamide is shown. Before the jump-to-contact and after the jump-off-contact, the force follows a D^{-2} law and is repulsive.

In water, another phenomenon can be observed, namely the hydrophobic meniscus force. If the sample surface is made hydrophobic by means of a layer of hydrocarbons and is dipped in water, after the tip has contacted the sample, hydrocarbon molecules form a meniscus that exerts a strong adhesion force. Thus the sample has to be withdrawn for a rather long distance before the tip detaches from the sample surface. Such a meniscus force results in withdrawal curves with a "slide-off-contact", i.e., a gradual and continuous pull-off, instead of a jump-off-contact. The attractive hydrophobic force can be hardly seen in Fig. 26. The jump-to-contact is rather big, however, and this cannot be due to the Hamaker constant. The attractive hydrophobic force is treated in detail in Section 6.6. Similar curves can be obtained on gold or platinum [61], because metals become hydrophobic when exposed to air due

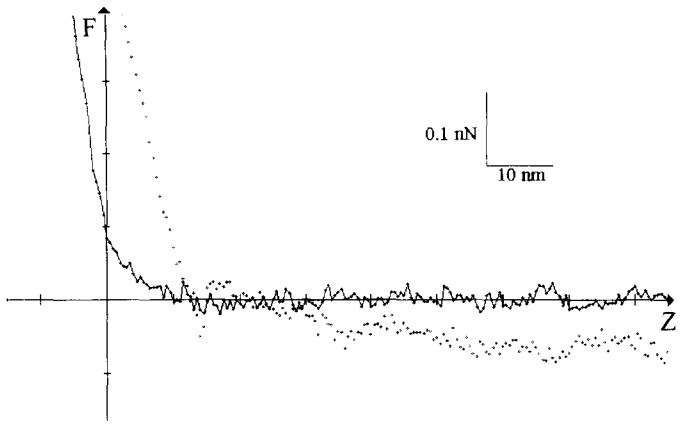

Fig. 25. Force–displacement curve in formamide with the repulsive van der Waals force just before the contact line and just past jump-off-contact (the continuous line is the approach curve). Note the splitting of the two zero lines of the approach and the retraction curve due to the viscosity of the medium (adapted from [128]).

to the adsorption of a thin layer of alkanes. Such "slide-off" curves become "jump-off" curves if gold is dipped into ethanol or cleaned with ethanol, which dissolves the alkane layer.

Experiments carried out in several liquids are summarized in Table 5. In addition to the works listed in Tables 4 and 5, those on double-layer force also contain measurements of the Van der Waals force of the system, since it is necessary to subtract the Van der Waals contribution in order to correctly estimate the double-layer force. Sometimes the Van der Waals force is computed on the basis of theoretical Hamaker constants in order to measure experimentally the double-layer force. Some authors compute the double-layer force and then experimentally measure the Van der Waals force.

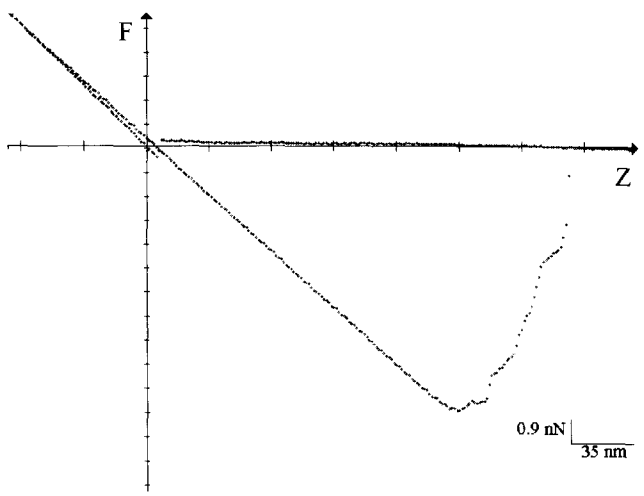

Fig. 26. Hydrophobic meniscus on gold in water. The pull-off is larger than on mica, and it is gradual and continuous over a distance of about 40 nm. Also the pull-off distance is larger than on mica (adapted from [128]).

Table 5
Measured attractive force F_{attr}, adhesion force F_{ad}, and surface energy γ for experiments in different liquids. Quantities labeled with (a) are unknown, tips labeled with (b) are colloidal particle. (c) PTFE = poly-tetra-fluoro-ethylene, PFMCH = per-fluoro-methyl-cyclo-hexane.

Ref.	Tip radius (nm)	Tip material/Medium/Sample	Measured (calculated)		
			A ($\times 10^{-19}$ J)	F_{attr} (nN)	F_{ad} (nN)
[61]	50	Si_3N_4/ethanol/mica, Au		0.14	0.2, 0.2–0.5
		/mica		0.06	0.2–1.5
		/platinum		26	55
		/H_2O + ethanol/platinum		20	29
		/ethanol/platinum		0	0
		/formamide/mica		−0.12	−0.12
	(a)	WC/ethanol/Au		0.3	0.5
		/mica			0.2–0.5
		/mica			0.5–2
		/Au		6	10
		/formamide/Au		7	15
[78]	50	Si_3N_4/ethanol/mica	1.16		
		/bromo-naphtalene/mica	−0.07		
		/methyl-naphtalene/mica	−2.36		
[101]	50	Si_3N_4/acetone/SiO_2, Si_3N_4			14 (15), 32
		/ethanol/SiO_2, Si_3N_4			12 (13), 20
[131]	(a), (b)	Au/cyclohexane/PTFE[c]	−0.55 (−0.52)		
		/*p*-Xylene/	−0.5 (−0.48)		
		/bromobenzene/	−0.55 (−0.76)		
		/perfluorohexane/	0.07 (0.125)		
		/PFMCH[c]/	0.05		
		/formamide	−0.4		
[128]	≅ 50	Si_3N_4/formamide/mica		−0.1	
		/ethanol/		0.1	
[130]	50	Si_3N_4/diodomethane/Si_3N_4, SiO_2	(0.1), (−0.08)	0.1, ≅ −0.2	0.6, ≅ −0.2
		/bromonaphtalene/SiO_2, Si_3N_4	(−0.02), (0.3)	≅ −0.1	≅ −0.1

The work of Weisenhorn et al. [61] has been of outstanding importance in the development of force–distance curves acquisition. Measurements have been done in water, ethanol and formamide for three kinds of systems: non-metal/non-metal, non-metal/metal and metal/metal. In water, the forces for non-metal/metal or metal/metal systems (Si_3N_4 on platinum or gold and WC on Au) are very much bigger than for non-metal/non-metal systems (Si_3N_4 on mica). The authors demonstrate that this is due to the hydrophobic meniscus by dipping the metals in ethanol or ethanol–water mixtures. The force progressively decreases due to the dissolving of the alkane layer. Forces in ethanol are of the same order for all the three systems. In formamide, the force between Si_3N_4 and mica is repulsive, while it is strongly attractive for WC and platinum. This is once again due to the hydrophobic meniscus, which is smaller than in water.

Table 6
Measured and calculated adhesion force for different polymers in perfluorodecalin. All data are taken from the Ref. [132]. The polystyrene tip is a colloidal particle. (a) FEP = poly-tetra-fluoro-ethylene-*co*-hexa-fluoro-propylene; PVDF = poly-vinilidene-fluoride; PAN = poly-acriloni-trile; PAA = poly-acrylic acid; PMMA = poly-(methyl-methacrylate).

Tip radius (nm)	Tip material/Sample	Measured (calculated) F_{ad} (nN)
51	SiO_x/FEP[a]	0.18 ± 0.08 (0.39)
	/PVDF[a]	0.62 ± 0.2 (1.23)
	/polypropilene	2.07 ± 0.15 (1.98)
	/polystyrene	2.98 ± 0.16 (2.76)
20	/PAN[a]	1.32 ± 0.15 (0.26)
	/PMMA[a]	1.84 ± 0.16 (0.73)
	/PAA[a]	2.13 ± 0.14 (0.84)
	/polystyrene	0.66 ± 0.1 (1.08)
3750	polystyrene/PAN[a]	54.4 ± 20.6 (55.5)
	/PMMA[a]	113 ± 4 (203)
	/PAA[a]	75.4 ± 4.5 (231)
	/polystyrene	135 ± 7.5 (314)

In the work of Hutter and Bechhoefer [78] different liquids are chosen in order to minimize the Hamaker constant and hence the Van der Waals attraction. The Van der Waals force is attractive in ethanol and repulsive in methyl-naphtalene, but it is nearly zero in bromo-naphthalene. Therefore, this liquid could be used in contact mode to enhance lateral resolution (see also Ref. [130]).

Finally, the work of Milling et al. [131] is designed to measure repulsive Van der Waals forces in different liquids. Nevertheless, some liquids with attractive Van der Waals forces are studied.

Feldman et al. [132] have shown the possibility of a kind of force spectroscopy on polymers. The best liquid for distinguishing samples is perfluorodecalin (PFD), since it shows the best signal-to-noise ratio. Measurements are all performed in PFD (see Table 6) using a glass or a polystyrene colloidal tip. The "exact" adhesion force is calculated on the basis of the JKR theory. Although a sensible trend for the adhesion force is found in the case of the first four polymers listed in Table 6, considerable discrepancies between the calculated and measured values occur for all the other measurements. These discrepancies are attributed to the microasperities of the polystyrene tip and to the presence of other interactions (e.g., hydrogen bonding) not accounted for in the Lifshitz theory.

A very interesting experiment is that of Mulvaney et al. [133], in which the authors have measured the forces between an oil (decane) droplet and a glass colloidal particle. The contact lines of the curves acquired with such a system depend on the scan rate. At very low scan rates (<0.5 Hz), the lines show a large number of high frequency oscillations and in the region between 0.5 and 2 Hz the lines show numerous, regularly spaced waves. At higher scan rates the oscillations are no longer evident. The Van der Waals force between glass and decane in water has been measured at low scan rates and the Hamaker constant is $6 \times 10^{-21} \pm 3 \times 10^{-21}$ J, in good agreement with the theoretical value of $3 \times 10^{-21} - 7 \times 10^{-21}$ J.

The experiments dealing with the determination of the Van der Waals force have demonstrated that the AFM is a useful tool in the study of this fundamental force. Measurements can be performed in any kind of liquid and between any kind of surfaces with high resolution. The exact determination of Hamaker constants is not a simple issue, but for several materials this has been achieved in good agreement with theoretical predictions. In other cases, the presence of other forces, the difficulty of eliminating contaminants, and the lack of knowledge of the tip shape make the measurement more problematic. The capability of distinguishing the Hamaker constants of very similar materials also has been demonstrated. The recent measurements of the Van der Waals force at a liquid/liquid interface are of outstanding importance.

6.2.3. Dependence on tip shape

Hartmann [111] has calculated the effect of tip shape assuming a Van der Waals force in the form:

$$F = g\frac{A}{D^n}, \tag{6.36}$$

in which g is a geometric factor that he has calculated by means of Lifshitz theory and A is the Hamaker constant, which is shape independent.

Hartmann has pointed out that, like Hamaker constants, geometric factors also depend on retardation. The retarded Van der Waals force decays on smaller distances, and hence involves a smaller effective volume than the non-retarded Van der Waals force. The non-retarded factor g_n, the retarded one g_r, and the power law index n of the non-retarded Van der Waals force are indicated in Table 7. The power law index of the retarded force is $n+1$, and there is a transition from n to $n+1$ for $D \geq 5\lambda_{132}$. In the present context the most important result is that the Van der Waals force decays as D^{-2} for the most realistic probe geometry, i.e., the paraboloidal apex.

Hao et al. [21] have calculated a correction factor for the flat-sphere system in order to take into account the elongated nature of the tip. Considering the tip as a cone of semiaperture $\theta/2$ and length L, ending with a sphere of radius R, for $D \ll L$ they obtain:

$$F(D) = -\frac{AR}{6D^2}\left(1 + \frac{D\mathrm{tg}^2(\theta/2)}{R}\right). \tag{6.37}$$

The correction factor is negligible for $D \ll R$.

The distribution of microasperities on the tip and/or on the sample has a dramatic effect on the calculated Van der Waals forces. Generally, the effect of microasperities is to greatly reduce the force,

Table 7
Retarded and non-retarded geometric factors for three geometries as calculated by Hartmann [111]. l_{xy} and l_z are the semiaxes of the paraboloid, R is the radius of the cylinder and θ the semiaperture of the cone.

	g_n	g_r	n
Cone	$(\mathrm{tg}^2\theta)/6$	$(\pi/3)\mathrm{tg}^2\theta$	1
Paraboloid	$l_{xy}^2/12l_z$	$\pi l_{xy}^2/3l_z$	2
Cylinder	$R^2/6$	πR^2	3

because the effective contact radius is smaller than the overall radius. Cohen et al. [43] have calculated that a distribution of microtips with mean radius of 20 Å and 4 Å rms deviation would reduce the adhesion force by more than 90%.

Bordag et al. [134] have calculated the corrections to the Van der Waals force corresponding to two types of deviations of the tip from the paraboloidal shape. The deviations of the first type are small protrusions on the tip surface that, in this case, can be described by the formula:

$$z_1(\rho) = \frac{\rho^2}{2R} + \xi f(x,y), \tag{6.38}$$

in which ρ is the cylindrical coordinate, R the tip radius, and $\xi f(x,y)$ is the stationary stochastic function with dispersion ξ and mean value $\langle \xi f(x,y) \rangle = 0$. The second type of deviations corresponds to a possible deformation of the tip surface described by

$$z_2 = \frac{[\rho + \xi g(\varphi)]^2}{2R}, \tag{6.39}$$

in which ρ and φ are cylindrical coordinates and $g(\varphi)$ is another stationary stochastic function with dispersion ξ and zero mean value.

In the first case the correction to the Van der Waals force is

$$F = -\frac{AR}{6D^2}\left[1 + 3\left(\frac{\xi}{D}\right)^2 + 15\left(\frac{\xi}{D}\right)^4\right]. \tag{6.40}$$

In the second case the correction is

$$F = -\frac{AR}{6D^2}\left[1 + \left(\frac{\xi}{\sqrt{RD}}\right)^2 - \frac{3}{4}\left(\frac{\xi}{\sqrt{RD}}\right)^4\right]. \tag{6.41}$$

For $\xi/D \cong 0.1$ the contribution of the second order correction is about 3%, while the contribution of the fourth order term is negligible. For $\xi/\sqrt{RD} \cong 0.1$ the correction to F_0 according to Eq. (6.41) is about 0.1%.

Toikka et al. [62] have verified the effect of microasperities on the tip. They measured the Van der Waals force for the system iron oxide/air or water/silica with a colloidal probe of radius $\cong$ 5μm. The measured value of the Van der Waals adhesion energy is very much smaller than the calculated value (see Table 2). If the calculation is made with the characteristic dimension of the asperities (between 10 and 40 nm) instead of the overall radius of the colloidal probe, experimental and calculated values are in agreement. They argue that asperities on the tip decrease the adhesion force not only because the effective radius is smaller than the overall radius, but also because a thin layer of water solution stays between the tip and the sample surface, thus exerting a repulsive double-layer force.

Cohen [39] has considered the effect of a layer of contaminants of height X adsorbed on a tip of radius R at a distance D from the sample surface. The interaction between the spherical tip and the flat sample is affected by the layer of contaminants as follows:

$$\mathrm{W} = \frac{A}{6}\left[\frac{2RD + D^2}{2(D+X)^2} - \frac{2(D+R)}{(D+X)} + \frac{3D + 2R}{2D} + \ln D + \ln(D+X)\right]. \tag{6.42}$$

For $R \gg D$, the force is given by

$$F = -\frac{A}{6}\left[\frac{R}{D^2} - \frac{RD + 3RX}{(D+X)^3}\right]. \tag{6.43}$$

For $D = 5$ Å and $X = 7$ Å the contaminant layer decreases the attractive force by about 50%.

6.3. Double-layer force

6.3.1. Theory

Usually, all surfaces of high dielectric constant in water or other liquids are charged. The charging may occur via either dissociation of surface groups (e.g., $COOH \rightarrow COO^- + H^+$) or adsorption of ions from the solution. Whatever be the charging mechanism, the final surface charge is balanced by a charged region of counterions of equal and opposite charge. Some of these counterions are bound to the surface in the so-called Stern layer, while others form an atmosphere of ions near the surface known as electric double-layer.

Following [15], consider two equally charged surfaces at a distance D and a liquid solution in between. The coordinate system is illustrated in panel (a) of Fig. 27.

If ions are present in solution, the chemical potential of each species of ion can be written as

$$\mu = ze\psi(x) + k_B T \log \rho(x), \tag{6.44}$$

in which $\psi(x)$ is the electrostatic potential and $\rho(x)$ is the number density of the counterions of valence z at each point x between the surfaces. Let $\psi(0) = \psi_0 = 0$, $\rho(0) = \rho_0$, and $(d\psi/dx)_0 = 0$ ($x = 0$ is the midplane between the two surfaces). Then the Boltzmann distribution of counterions is given by

$$\rho(x) = \rho_0 \exp(-ze\psi(x)/k_B T). \tag{6.45}$$

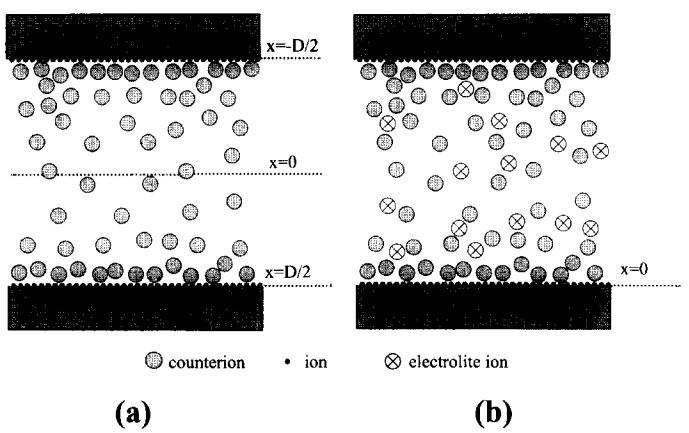

Fig. 27. Panel (a): the coordinate system employed in the derivation of the double-layer force without electrolyte ions (Eqs. (6.44)–(6.59)). D is the tip–sample distance and the tip and sample surfaces are at $x = \pm D/2$. $x = 0$ is the midplane. Panel (b): the coordinate system employed in the derivation of the double-layer force with electrolyte ions (Eqs. (6.60)–(6.75)). D is the tip–sample distance. $x = 0$ is the sample surface. The distribution of the counterions and of the electrolyte ions in the liquid gap is also sketched.

Eq. (6.45), together with the Poisson equation, yields

$$\frac{d^2\psi(x)}{dx^2} = -\frac{ze\rho(x)}{\varepsilon\varepsilon_0} = -\frac{ze\rho_0}{\varepsilon\varepsilon_0}\exp\left(-\frac{ze\psi(x)}{k_BT}\right). \tag{6.46}$$

This is the Poisson–Boltzmann equation. Solving Eq. (6.46), one obtains the potential $\psi(x)$, the electric field $E(x) = d\psi(x)/dx$, and the counterion density $\rho(x)$.

The two boundary conditions needed to solve Eq. (6.46) are

$$E_0 = \left.\frac{d\psi(x)}{dx}\right|_0 = 0, \tag{6.47a}$$

$$\sigma = -\int_0^{D/2} ze\rho(x)\,dx = \varepsilon\varepsilon_0\int_0^{D/2}\frac{d^2\psi(x)}{dx^2}dx = \varepsilon\varepsilon_0\left.\frac{d\psi(x)}{dx}\right|_{D/2} = \varepsilon\varepsilon_0 E_s. \tag{6.47b}$$

The latter condition means that the total charge in the liquid gap is equal and opposite to the surface charge, σ.

Next consider the counterions distribution. Differentiating Eq. (6.45) and inserting Eq. (6.46), yields

$$\frac{d\rho(x)}{dx} = -\frac{ze\rho_0}{k_BT}\exp\left(-\frac{ze\psi(x)}{k_BT}\right)\frac{d\psi(x)}{dx} = \frac{\varepsilon\varepsilon_0}{k_BT}\frac{d\psi(x)}{dx}\frac{d^2\psi(x)}{dx^2} = \frac{\varepsilon\varepsilon_0}{2k_BT}\frac{d}{dx}\left(\frac{d\psi(x)}{dx}\right)^2 \tag{6.48}$$

and hence

$$\rho(x) - \rho_0 = \int_0^x d\rho = \frac{\varepsilon\varepsilon_0}{2k_BT}\int_0^x d\left(\frac{d\psi(x)}{dx}\right)^2 = \frac{\varepsilon\varepsilon_0}{2k_BT}\left(\frac{d\psi(x)}{dx}\right)^2\Bigg|_x. \tag{6.49}$$

Using Eq. (6.47b), the value ρ_s of $\rho(x)$ at the surface ($x = \pm D/2$) can be determined:

$$\rho_s = \rho_0 + \frac{\sigma^2}{2\varepsilon\varepsilon_0 k_BT}. \tag{6.50}$$

Eq. (6.50) shows that the concentration of ions at the surface depends only on σ and ρ_0. Most of the counterions balancing the surface charge are placed in the first few angstroms near the surface. However, for lower densities σ, since $\rho_s \propto \sigma^2$, the counterions layer extends well beyond the surface.

The Poisson–Boltzmann equation can be satisfied by

$$\psi(x) = \frac{k_BT}{ze}\log\cos^2\Gamma x, \quad \Gamma = \sqrt{\frac{(ze)^2\rho_0}{2\varepsilon\varepsilon_0 k_BT}}. \tag{6.51}$$

Γ can be determined from Eq. (6.51) if E_s is known:

$$E(x) = \frac{d\psi(x)}{dx} = -\frac{2k_BT\Gamma}{ze}\operatorname{tg}\Gamma x \Rightarrow E_s = \frac{\sigma}{\varepsilon\varepsilon_0} = -\frac{2k_BT\Gamma}{ze}\operatorname{tg}\frac{\Gamma D}{2}. \tag{6.52}$$

The counterion distribution

$$\rho(x) = \rho_0\exp\left(-\frac{ze\psi(x)}{k_BT}\right) = \frac{\rho_0}{\cos^2\Gamma x} \tag{6.53}$$

is known once Γ is determined in terms of σ and D.

Since $\partial P/\partial x|_{x,T} = \rho\partial\mu/\partial x|_{x,T}$, the variation in pressure resulting from bringing the two surfaces from an infinite distance to a distance $x = D/2$ is

$$P(x) = -\int_{\xi=D/2}^{\xi=\infty}\left[ze\rho\frac{\mathrm{d}\psi(x)}{\mathrm{d}x}\bigg|_x \mathrm{d}\xi + k_\mathrm{B}T\,\mathrm{d}\rho(x)\right], \tag{6.54}$$

in which x is the fixed point in which values are computed and ξ is the variable separation between surfaces. Substituting the Poisson equation into the previous equation we obtain

$$P^D(x) - P^\infty(x) = -\frac{\varepsilon\varepsilon_0}{2}\left(\frac{\mathrm{d}\psi(x)}{\mathrm{d}x}\bigg|_{x(D)}\right)^2 + k_\mathrm{B}T\rho^D(x) + \frac{\varepsilon\varepsilon_0}{2}\left(\frac{\mathrm{d}\psi(x)}{\mathrm{d}x}\bigg|_{x(\infty)}\right)^2 - k_\mathrm{B}T\rho^\infty(x), \tag{6.55}$$

in which $P^D(x), P^\infty(x), \rho^D(x)$, and $\rho^\infty(x)$ are the pressures and the distributions when the two surfaces are at a distance D and at an infinite distance. In the case that no electrolyte ions are present in solution, $\rho^\infty(0) = P^\infty(x) = 0$. Thus $P^D(x)$ is the sum of two contributions. The first one, always attractive, is the contribution of the electrostatic field and the second one is the osmotic or entropic contribution and it is always repulsive.

From Eq. (6.55) one can see that the origin of the repulsive force between charged surfaces in solution is not electrostatic (the electrostatic term is always attractive), but entropic. What keeps the double-layer of counterions expanded is the osmotic pressure that compels counterions away from the surfaces and far from each other, in order to increase the configurational entropy. By bringing the two surfaces in contact, the counterions in solution are forced to come in contact with the surfaces, against their equilibrium configuration.

Inserting Eqs. (6.49) and (6.50) into Eq. (6.55) it is possible to derive an expression for the pressure at the surface ($x = \pm D/2$):

$$P_\mathrm{s}^D = k_\mathrm{B}T\rho^D(0) = k_\mathrm{B}T[\rho_\mathrm{s}^D - \rho_\mathrm{s}^\infty]. \tag{6.56}$$

This important equation, known as the contact value theorem, is always valid as long as there is no interaction between counterions and surfaces.

Using Eqs. (6.46) and (6.51) to evaluate $\rho^D(0)$ in Eq. (6.56) leads to an expression for the pressure in terms of Γ:

$$P = k_\mathrm{B}T\rho_0 = 2\varepsilon\varepsilon_0\left(\frac{k_\mathrm{B}T}{ze}\right)^2\Gamma^2. \tag{6.57}$$

In order to evaluate Eq. (6.57) for two limiting cases $\sigma \to \infty$ and $D \to \infty$ one needs to know Γ. For $\sigma \to \infty$, Eq. (6.52) yields $\Gamma D/2 \to \pi/2$. For $D \to 0$, tg $\Gamma D/2 \cong \Gamma D/2$ and Eq. (6.52) yields $\Gamma^2 \to -\sigma ze/\varepsilon\varepsilon_0 k_\mathrm{B}TD$. In the first case the Langmuir equation is obtained:

$$\lim_{\Gamma D/2\to\pi/2} P(D) = \frac{2\varepsilon\varepsilon_0(\pi k_\mathrm{B}T/ze)^2}{D^2}. \tag{6.58}$$

In the second case:

$$\lim_{\Gamma^2\to-\sigma ze/\varepsilon\varepsilon_0 k_\mathrm{B}TD} P(D) = -\frac{2\sigma k_\mathrm{B}T}{zeD}. \tag{6.59}$$

The simple form for the Poisson equation, Eq. (6.46), is valid only if there are no electrolyte ions in solution. If there are electrolyte ions in solution, Eq. (6.45) must be written for each kind of ion and the sum used for $\rho(x)$ in Eq. (6.46). In this case the total concentration of ions at the surface is

$$\sum_i \rho_{0i} = \sum_i \rho_{\infty i} + \frac{\sigma^2}{2\varepsilon\varepsilon_0 k_B T} \tag{6.60}$$

in which z_i is the valence, ρ_{0i} the distribution at the surface, and $\rho_{\infty i}$ is the distribution at an infinite distance for the ith ion. In the following, the x coordinate origin is changed, since one of the surfaces is now at infinite distance. Hence $x = 0$ now indicates the surface position and no longer the midplane. The new system of coordinate is illustrated in panel (b) of Fig. 27.

The ions at the surface are mainly the counterions. Their excess concentration over the bulk concentration depends only on σ. From Eq. (6.60), it is possible [15] to determine the relation between σ and ψ_0 in the case of a mixed KCl+$CaCl_2$ electrolyte:

$$\begin{aligned}\sigma^2 &= 2\varepsilon\varepsilon_0 k_B T\left(\sum_i \rho_{0i} - \sum_i \rho_{\infty i}\right)\\ &= 2\varepsilon\varepsilon_0 k_B T([K^+]_\infty \exp(-e\psi_0/k_B T) + [Ca^{2-}]_\infty \exp(-2e\psi_0/k_B T) + [Cl^-]_\infty \exp(e\psi_0/k_B T))\\ &\quad - 2\varepsilon\varepsilon_0 k_B T([K^+]_\infty + [Ca^{2-}]_\infty + [Cl^-]_\infty).\end{aligned} \tag{6.61}$$

Since $[Cl^-]=[K^+]+2[Ca^{2+}]$, Eq. (6.61) becomes

$$\begin{aligned}\sigma &= \sqrt{2\varepsilon\varepsilon_0 k_B T}[K^+]_\infty\{\exp(-e\psi_0/k_B T) + \exp(e\psi_o/k_B T) - 2\}\\ &\quad + \sqrt{2\varepsilon\varepsilon_0 k_B T}[Ca^{2+}]_\infty\{\exp(-2e\psi_0/k_B T) + 2\exp(e\psi_0/k_B T) - 3\}\\ &= \sqrt{8\varepsilon\varepsilon_0 k_B T}\sinh(e\psi_0/k_B T)\sqrt{[K^+]_\infty + [Ca^{2+}]_\infty(2 + \exp(-e\psi_0/k_B T))}.\end{aligned} \tag{6.62}$$

Eq. (6.62) is the Grahame equation. This equation shows that, at constant surface charge density, the surface potential decreases with increasing electrolyte concentration. In the presence of divalent cations the surface potential decreases more than in the case of monovalent ions.

In most cases, when there are electrolyte ions in solution, neither σ nor ψ_0 stay constant, because of reactions at the surface. Such reactions at the surface can be described by means of a reaction constant that can be inserted in Grahame equation. Parsegian and Gingell [135] have studied the consequences of these surface reactions. Their results can be summarized as follows:

(1) The interaction potential is always intermediate between two limits.
(2) The upper limit corresponds to the case of constant charge.
(3) The lower limit corresponds to the case of constant electric potential.

A particularly interesting limit of the Grahame equation is the limit at small potentials. Below 25 mV, Eq. (6.62) becomes [15]:

$$\sigma = \varepsilon\varepsilon_0 K_D \psi_0, \tag{6.63}$$

in which

$$K_D = \sqrt{\sum_i \frac{\rho_{\infty i} e^2 z_i^2}{\varepsilon\varepsilon_0 k_B T}}. \tag{6.64}$$

Eq. (6.63) is analogous to the equation for a capacitor with charge density $\pm\sigma$, potential ψ_0, and whose plates are separated by a distance $1/K_D$. The characteristic length $1/K_D$ is the Debye length. The Debye length depends only on solution properties and not on surface properties. At 25 °C the Debye length of aqueous solutions is:

$$\frac{1}{K_D} = \begin{cases} 0.304/\sqrt{[X]}\,\text{nm} & \text{for 1:1 electrolytes,} \\ 0.176/\sqrt{[X]}\,\text{nm} & \text{for 1:2 or 2:1 electrolytes,} \\ 0.152/\sqrt{[X]}\,\text{nm} & \text{for 2:2 electrolytes,} \end{cases} \tag{6.65}$$

in which [X] is the electrolyte concentration in moles.

In the general case, i.e. for any potential, the electrostatic potential is given by

$$\psi(x) = \frac{2k_BT}{e}\log\frac{1+\gamma e^{-K_D x}}{1-\gamma e^{-K_D x}} \cong \frac{4k_BT}{e}\gamma e^{-K_D x}, \tag{6.66}$$

where

$$\gamma = \text{tgh}\frac{e\psi_0}{4k_BT}. \tag{6.67}$$

This is known as the Gouy–Chapman theory. At strong electric potentials $\gamma \to 1$, whereas, for small potentials, Eq. (6.66) becomes the so-called Debye–Hückel equation:

$$\psi(x) \cong \psi_0 e^{-K_D x}. \tag{6.68}$$

For an 1:1 electrolyte the interaction pressure and the interaction energy are given by [15]:

$$P = 64k_BT\rho_\infty\gamma^2 e^{-K_D D} \quad \text{and} \quad W = 64k_BT\rho_\infty\frac{\gamma^2}{K_D}e^{-K_D D}. \tag{6.69}$$

For small potentials Eq. (6.69) becomes

$$P = 2\frac{\sigma^2}{\varepsilon\varepsilon_0}e^{-K_D D} \quad \text{and} \quad W = 2\frac{\sigma^2}{K_D\varepsilon\varepsilon_0}e^{-K_D D}. \tag{6.70}$$

Since K_D is proportional to the electrolyte concentration ρ, the force and the potential are inversely proportional to the salt concentration.

Generally in an AFM the tip and sample have different surface charge densities. Parsegian and Gingell [135] have described the double-layer force per unit area between two semiinfinite surfaces with surface charge density σ_1 and σ_2 at a distance D in the limit of small potentials (<25 mV):

$$f_{dl} = \frac{2}{\varepsilon\varepsilon_0}\frac{\sigma_1^2+\sigma_2^2+\sigma_1\sigma_2(e^{K_D D}+e^{-K_D D})}{(e^{K_D D}-e^{-K_D D})^2}. \tag{6.71}$$

If $K_D D \gg 1$, Eq. (6.71) becomes

$$f_{dl} = \frac{2}{\varepsilon\varepsilon_0}[(\sigma_1^2+\sigma_2^2)e^{-2K_D D}+\sigma_1\sigma_2 e^{-K_D D}]. \tag{6.72}$$

Butt [136] has computed the double-layer force between a flat sample and a spherical tip with radius R by integrating Eq. (6.72) on circular sections $2\pi r dr$ (Derjaguin approximation):

$$F_{dl} = \frac{\pi}{\varepsilon\varepsilon_0 K_D^2}[(\sigma_T^2 + \sigma_S^2)(e^{-2K_D R} + 2K_D R - 1)e^{-2K_D D} + 4\sigma_T\sigma_S(K_D R + e^{-K_D R} - 1)e^{-K_D D}], \quad (6.73)$$

in which σ_T and σ_S are the tip and sample surface charge densities. If $K_D R \gg 1$, Eq. (6.73) becomes

$$F_{dl} = \frac{2\pi R}{\varepsilon\varepsilon_0 K_D}[(\sigma_T^2 + \sigma_S^2)e^{-2K_D D} + 2\sigma_T\sigma_S e^{-K_D D}]. \quad (6.74)$$

If $\sigma_T \ll \sigma_S$, i.e., if the tip is neutral, the first term in Eq. (6.74) dominates and the double-layer force decays with $1/2K_D$, whereas, if $\sigma_T \cong \sigma_S$, the second term dominates and the double-layer force decays with $1/K_D$. However, for $D > (1/K_D)\ln((\sigma_T^2 + \sigma_S^2)/2\sigma_T\sigma_S)$, the second term in Eq. (6.74) is always dominant. It should also be noted that the double-layer force between two bodies with different surface charge may be attractive, whereas the double-layer force between two surfaces with the same surface charge density is always repulsive.

A similar, approximate expression can be derived in the case of constant potential [137]:

$$F_{dl} = 4\pi\varepsilon\varepsilon_0 R K_D \psi_T \psi_S e^{-K_D D}. \quad (6.75)$$

Also in this case, the double-layer force may be attractive or repulsive depending on the sign of the potentials product.

The behavior of oxide-like materials, such as Si–OH, is particularly important for the AFM. For such materials, the potential is governed by the amphoteric character of surface sites, i.e., the groups can act as proton donors (Si–OH→SiO^-) or proton acceptors (Si–OH→$SiOH_2^+$). Therefore, both pK^+ for donors and pK^- for acceptors must be defined and the point of zero charge (PZC) is equal to the quantity $(pK^+ + pK^-)/2$. The surface potential is positive (negative) when the pH of the solution is smaller (larger) than the PZC. If both tip and sample are oxide-like materials, two isoelectric points (IEP) can be defined when the potential becomes zero for either the tip or the sample. Hence the double-layer force is repulsive for pH values smaller than the smallest IEP or larger than the largest IEP, and is attractive in between.

6.3.2. *Experimental results*

In order to introduce the experimental results on double-layer force, a specific AFM measurement of these forces is presented first. In this experiment, the AFM tip is made of silicon nitride and the substrate is mica. The electrolyte is KCl and the Debye length is varied by varying the KCl concentration at constant pH. The force–displacement curves at different concentrations are depicted in Fig. 28.

Increasing the concentration up to 0.1 M, three changes occur:

1. the repulsive force becomes smaller and smaller;
2. its decay length diminishes;
3. the Van der Waals force appears.

At 0.1 M KCl concentration, the force–displacement curve resembles the one in deionized water (Fig. 23). Since deionized water is a weak electrolyte (10^{-7} M in both H_3O^+ and OH^-), it should show

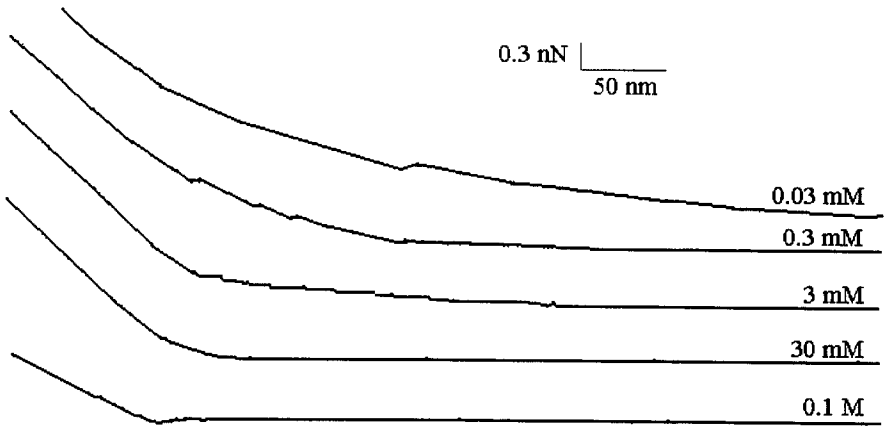

Fig. 28. Force–displacement approach curves associated with double-layer force between a silicon nitride tip and mica in KCl solutions of different concentration. The tip radius is estimated between 50 and 100 nm. On the x-axis, the sample position in nm. On the y-axis, the force in nN (adapted from [128]).

the highest double-layer force. However, this long range force is acting on distances well beyond the range of the AFM tip motion. Therefore, it is not possible to detect the actual zero line and to define the zero force reference.

These results were first obtained by Butt [138] with Si_3N_4 tips on mica, diamond tips on mica and glass tips on glass, by Weisenhorn et al. [61], by Atkins and Pashley [92] with a ZnS colloidal sphere on mica, and by Li et al. [94] with polystyrene spheres on polystyrene spheres or mica. Only a qualitative comparison can be done, since the tip radius of curvature is unknown. In all papers, in order to deduce the Debye length, the force law has been fitted with the second term of Eq. (6.74), since one supposes $K_D D \gg 1$ and $K_D R \gg 1$. A good agreement has been found in all the cases. Weisenhorn et al. have obtained a remarkable agreement with Eq. (6.65) (Debye length $= 0.308/\sqrt{[KCl]}$ nm). The fact that only the second term of Eq. (6.74) is needed to fit the experimental data implies that the surface charge density of diamond and silicon nitride are comparable to that of mica. This evidence contradicts what one would expect for these two materials. In the case of Si_3N_4 the origin of the surface charge could be explained by the presence of small amounts of oxide [138].

Similar series of curves can be obtained in other electrolyte solutions, e.g., $MgCl_2$ [138], $CaCl_2$ [139] or $Ca(NO_3)_2$ [140]. Using a 2:1 salt, the Debye length decreases, and the double-layer force vanishes at a 30 mM concentration. In order to measure the dependence of double-layer force on tip and/or sample surface charge, a sample whose surface charge density depends on pH has to be employed.

Fig. 29 shows force–displacement curves on stearic acid in different pH solutions. Stearic acid pK is nearly 8. This means that, at pH less than 8, the sample surface is uncharged, there is no double-layer force and there is a jump-to-contact due to the Van der Waals force (1–3 nN). At pH 8.1 the surface begins to charge and the double-layer force counterbalances the Van der Waals force, so that there is no jump-to-contact. Finally, at a pH greater than 8, the double-layer force appears.

Ishino et al. [127] have characterized the charging of several functional groups as a function of pH. A behavior similar to that shown in Fig. 29 was observed for stearic acid and steryl amide (in this case, repulsive forces are observed for pH > 10.5). Butt [138] has shown the transition from double-layer force to Van der Waals force for an alumina tip on mica. Mica is negatively charged at any pH value,

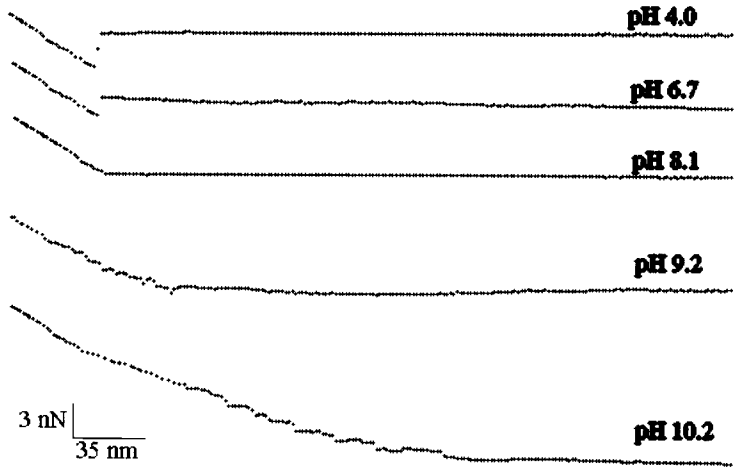

Fig. 29. Dependence of double-layer force on the surface charge of a stearic acid sample. Curves are acquired at different pH with a silicon nitride tip (tip radius between 50 and 100 nm). On the x-axis, the sample position in nm. On the y-axis, the force in nN.

whereas alumina is positively (negatively) charged below (above) pH 8.1. The forces are repulsive above pH 8.1 and attractive below pH 8.1.

Several studies have been dedicated to the double-layer force on oxide-like materials.

Raiteri et al. [141] have studied the pH dependence of forces for Si_3N_4 tips on Si_3N_4, Al_2O_3, and mica, demonstrating the capability of AFM in determining the PZC of such materials. For Si_3N_4 on Si_3N_4, forces are always repulsive with the exception of a range around pH 6–7. This means that the tip and sample always bear a charge of the same sign and that the PZC is around pH 6.5. For Si_3N_4 on mica the total tip–sample force changes from attractive (for $pH \leq 6$) to repulsive ($pH \cong 8$). This is consistent with the fact that mica is negatively charged and the PZC of silicon nitride tip is around pH=6.5. For Si_3N_4 tips on Al_2O_3 the forces are always repulsive, with a repulsion minimum at pH=4.3. Hence the PZC is between pH=4 and pH=5. In addition to the experimental results, the authors introduce a simulation method based on the computation of the double-layer force by means of Eq. (6.73), in which the tip and sample charges are calculated according to the site binding theory. Such a method predicts well the qualitative behavior of double-layer force for all the three samples.

Similar results have been obtained by Karaman et al. [142] for an Al_2O_3 substrate with aluminum or Si_3N_4 tips, and by Senden and Drummond [124] for mica with a silicon nitride tip. In this work, the pH dependence of double-layer force with and without background electrolyte is investigated, and measurements at constant pH with different electrolyte concentrations have been performed. The curves are fitted taking into account both the Van der Waals force and double-layer force (see also Ref. [143]).

Arai et al. [144] have measured the PZC of Al_2O_3, SnO_2, and SiO_2 with a Si_3N_4 tip in buffer. The PZC are measured by monitoring the amplitude of the repulsive or attractive forces at different pH (2–12) at a distance corresponding to $1/2K_D$, i.e., 15 nm, in order to make Van der Waals force negligible. For Al_2O_3 the results agree with those of Raiteri et al. For SnO_2 forces are repulsive below pH=6 and above pH=10. The first IEP is due to the PZC of Si_3N_4, the second to that of SnO_2. The SiO_2 has a PZC at $pH \cong 2$, and hence there is only an IEP due to Si_3N_4 (see also Refs. [17, 144, 145]). Furthermore, the

authors have studied the pH dependence of forces on a SiO_2 substrate partially covered with hydrocarbons. They show that both attractive (at pH=3) and repulsive (at pH=10) forces are stronger on bare SiO_2. Such a behavior indicates that the surface charge density of bare SiO_2 is larger than that of the HC-covered quartz. When the quartz is uncharged (pH=6.8), the force–displacement curves on the two substrates overlap and show a slight repulsive double-layer force due to the tip charging.

Lin et al. [137] have once more studied the IEP for a silicon nitride tip on SiO_2 with two different methods. The IEP due to silicon nitride is 6.2 ± 0.2 and 5.8 ± 0.4 (see also Ref. [62] for the determination of the IEP of ZnS and [146] for the determination of the IEP of TiO_2).

Larson et al. [91] have compared the determination of the potentials by means of the AFM with the electrophoretic determination. The system employed was a TiO_2 colloidal sphere on TiO_2. A good agreement between these two methods is found. In later works, the same comparison is established for a silica colloidal sphere on TiO_2 and on silica [147] and for colloidal silica probes on silica [148]. Once again there is a good agreement between the two methods (see also Ref. [149]).

Butt [150] has acquired force–displacement curves on purple membrane deposited onto alumina at different pH. The purple membrane is negatively charged above pH=3, alumina is negatively (positively) charged above (below) $pH = 8.1$ and the oxidized Si_3N_4 tip is always negatively charged. Hence, force–displacement curves are repulsive both on alumina and on purple membrane for pH values larger than 8, while they become attractive on alumina and stay repulsive on purple membrane for $pH < 8$. The force is weaker on alumina than on purple membrane. The author could calculate the surface charge density of purple membrane from the ratio of repulsive forces at pH 10.3 and 9.3 and from the known surface charge density of alumina.

The double-layer force between a very sharp ZnO whisker crystal ($R \cong 10$ nm) and an amino-silanized coverslip has been measured by Aoki et al. [12]. The double-layer force is measured in deionized water, in 0.1 mM and 1 mM KCl, and in 0.1 mM and 1 mM $MgCl_2$. The authors take advantage of extremely flexible cantilevers (see Section 1.3) in order to acquire subpiconewton details of the force in the range 0–5 nm.

Drummond and Senden [69] have demonstrated that the double-layer force between a silicon nitride tip and mica in hexadecyltrimethylammonium bromide (CTAB) is intermediate between the theoretical constant surface charge fit and the theoretical constant potential fit (see also Refs. [62, 90, 147, 151, 152]).

Biggs et al. [92, 153] have measured force–distance curves between a gold colloidal sphere and a gold flat substrate in different solutions. They verified the increasing of the strength and decay length of double-layer force with decreasing ion concentrations (NaCl, trisodium citrate or gold chloride). By fitting the experimental data both with the constant charge force and the constant potential force, the authors were able to establish that the charge, and hence the adsorbed ions concentration, is constant. Also the dependence of double-layer force on pH was studied (see also Ref. (154]).

Hu and Bard [155] have exploited the double-layer force to monitor the adsorption of sodium dodecyl sulfate (SDS) on functionalized gold substrates. SDS is a negatively charged molecule. When force–distance curves are collected between a silica colloidal probe and silica in SDS solutions at pH 5, the force is always repulsive at any SDS concentration. When the substrate is positively charged gold, the force is attractive for SDS concentrations smaller than 5×10^{-6} M and becomes repulsive for larger concentrations, indicating that the SDS has adsorbed on gold and the surface has become negatively charged. The same behavior is verified for hydrophobic gold (charge reversal for 10^{-5} M SDS concentration). At a certain concentration, called critical micelle concentration (cmc), micelles begin to

form and adsorb onto the substrate. Na^+ ions begin to bind to micelles in order to compensate the high negative charge of micelles. These bound Na^+ ions no longer contribute to the diffuse double-layer. By determining the Debye length of the solution, the cmc can be measured in rather good agreement with other methods.

Similar experiments have been performed by Manne et al. [156] with cetyltrimethilammonium bromide (CTAB) on graphite, by Larson et al. [157] with pyridine on gold, by Hu et al. [158] with hexa-meta-phosphate on CdS, and by Kane and Mulvaney [154] with lead on gold surfaces covered with thiols.

Raiteri et al. [159, 160] have acquired force–displacement curves between a silicon nitride tip and a platinum or gold sample mounted on an electrode. An electric potential was applied between the sample and a counter electrode. Measurements have been performed at pH 9–10 in order to have a negative tip potential. The authors show the existence of three regimes. At negative potentials (−0.5–0 V), as expected, the tip–sample force is dominated by the double-layer force. In this interval of potential the double-layer force is almost constant. Between 0 and 1V the double-layer force steeply declines. At high potentials (> 1 V) an attractive exponential force onsets, with a decay length of about 50 nm for platinum. The third region is absent in the case of gold (as a matter of fact, anions bind strongly to gold and hence larger positive potentials are needed to make the attractive force appear). In the case of gold, the oxidation of the surface can be revealed due to a sharp increase in adhesion. The calculation of forces by means of the Poisson–Boltzmann theory enables the prediction of the behavior of the system in the first and second region, but the attractive exponential force in the third region cannot be explained with this theory. Force–displacement curves with an applied potential have been measured also by Ishino et al. [161] with similar results.

Hillier et al. [162] have measured the forces between a silica colloidal probe and a gold electrode as a function of the applied potential. They show that the force is strongly repulsive for voltages between −0.2 and −0.7 V, and the double-layer repulsion increases with the decreasing potential. The force becomes slightly repulsive for $V = -0.1$ V and is attractive for $V = 0$ V or $V = 0.1$ V. The authors show that the theoretical curves with constant charge boundary conditions fit better to the experimental data than the constant potential model. The PZC of the system is also determined by plotting the force as a function of the applied voltage at different distances from the sample surface. The authors, both theoretically and experimentally, demonstrate that the point of zero force, i.e., the potential at which the force becomes zero depends on the distance from the sample surface at which forces are measured (going from −0.2 V for forces measured at 25 nm up to −0.1 V for forces measured at 5 nm). The dependence of the PZC on the dimensions of the ions in solutions is also verified by acquiring force–distance curves in NaF, KCl, KBr and KI solutions.

The double-layer force has been measured also at the liquid/liquid interface. Mulvaney et al. [133] have acquired force–distance curves between a glass colloidal particle and an oil droplet in pure water or in a 1 mM sodium dodecyl sulfate (SDS) and 10 mM NaCl solution. In pure water the curve is attractive (see Section 6.3), but when salts are added, they adsorb onto the oil droplet and form a charged monolayer giving rise to the repulsive double-layer force. The measured surface potential of the droplet is less than −40 mV, and the measured Debye length is 10 nm, rather than −120 mV and 0.3 nm, as expected from theory. The authors attribute these large discrepancies to several factors. First of all the contact line between the colloidal sphere and the droplet is affected by strong oscillations depending on the scan rate, probably due to fluctuations in the fluidity of the oil/water interface. Hence, it is very difficult to find the contact distance. Furthermore, since the droplet surface is oscillating, the

contact line might not correspond to a plane of surface charge. Finally, the surfactant SDS is likely to diffuse or migrate out of the region of double-layer interaction so that the surface charge is fluctuating in an undetermined fashion and the oil can flow into the diffuse double-layer.

Drummond and Senden [69] have exploited the double-layer force in order to determine the effective radius R_{eff} of a pyramidal tip. The method is based on comparing the forces measured with the colloidal probe and the forces measured with the pyramidal tip at a certain reference distance from the sample surface, thus obtaining a scaling factor that can be used to normalize the force measured at all other distances. The reference distance is chosen in order that the contribution of the Van der Waals force and of other forces is negligible (typically it is 15 or 20 nm) and the entire force is due solely to the double-layer. Furthermore, at such distances, also the difference between the two boundary conditions, i.e., constant charge and constant potential, is negligible.

The study of the double-layer force has perhaps given the best results in AFM studies of forces. The capability of the instrument in characterizing this force with high resolution in any kind of liquid solution and with any kind of surfaces is fully demonstrated. The dependence of the force on the pH of the solution or on the salt concentration has been extensively studied for several kinds of systems. The AFM is routinely used to measure the Debye length of solutions, to determine the PZC of materials, and to calculate the surface charge density of substrates. The forces at a liquid/liquid interface, the dependence of forces on applied potentials and the study of ions adsorption at interfaces are now the most intriguing issues.

6.3.3. Dependence on tip shape

As for all other forces, the knowledge of the tip shape is critical for the quantitative measurement of the double-layer force. Arai and Fujihira [163] have calculated the double-layer force according to Eq. (6.55) for a conical sphere-ended tip with the cone angle 2θ ranging from 1° to 150° and the radius of curvature R ranging from 1 to 3500 nm and for a spherical tip of the same R. The calculations were performed in 10^{-3} and 10^{-4} M 1 : 1 electrolytes. In the 10^{-3} M electrolyte, for $R = 20$ nm, the forces differ significantly for $2\theta = 90°$ and $2\theta = 30°$ (at 10 nm the force is 0.018 nN for the 90° tip and 0.01 nN for the 30° tip). The force for the spherical tip is similar to the force for the 30° tip. Such differences disappear for $R = 200$ nm. In the 10^{-4} M electrolyte, for $R = 20$ nm, all the three tips (30°, 90°, and spherical) probe different forces (at 1 nm the force is 0.0075 nN for the spherical tip, 0.015 nN for the 30° tip, and 0.0475 nN for the 90° tip). A slight difference persists for the 30° tip and the 90° tip or the spherical tip in the case of $R = 200$ nm. The difference disappears for $R = 500$ nm. The authors have also fitted experimental data testing the validity of the low potentials approximation [Eq. (6.70)] for a silicon nitride tip with $R = 20$ nm and $2\theta = 30°$ onto a silicon sample in pH 11.4. Experimental data are best fitted by the curve calculated without such an approximation.

Sader et al. [164] have used the linearized Poisson–Boltzmann theory to calculate the electrical double-layer force between identical spheres and have compared the exact value of the force with that obtained with the Derjaguin approximation. Drummond and Senden [69] have utilized this procedure to study the applicability of the Derjaguin approximation. They calculated the ratio of the Derjaguin approximation to the exact interaction between a sphere and a flat surface, assuming that such a ratio for the sphere–plate system is half of that for the sphere–sphere system. They found that, for the constant potential interaction, this ratio is always 1 for $K_D R > 2$ and is between 1.1 and 1 for $K_D R < 2$.

The situation is worst for the constant charge interaction, since the ratio is between 1.5 and 1.05 for $K_D R < 10$.

Also microasperities on the tip are of fundamental importance for the quantitative measurement of double-layer force. First of all, surface roughness may lead to a wrong determination of the contact distance and of the position of the plane of charge on the tip and on the sample. One simplistic approach to this problem is to create a macroscopic reference plane at a negative separation equal to half the maximum roughness (average plane of charge) [17, 69]. If the contact occurs at the microasperities separation rather than at the average plane of charge, the derived value of the surface potential is an underestimate [149].

Toikka et al. [62] have showed that, because of microasperities, the liquid is not completely squeezed out at contact and a thin layer of liquid stays between the tip and the sample, thus exerting a double-layer force that decreases the adhesion force. Therefore, the apparent adhesion force depends on pH. The authors found an evidence of this phenomenon measuring adhesion forces at different pH between an iron oxide colloidal probe and silica. The silica surface is negatively charged at pH > 2, while the iron oxide surface is negatively charged at pH > 6. Thus, for pH > 6, there is a repulsive double-layer force. If the liquid was completely squeezed out at contact, adhesion force would not depend on pH. But this is not the case, experimentally, as the adhesion decreases with increasing pH for pH < 6 and is zero for pH > 6.

6.4. Solvation forces

The continuum theories of Van der Waals force and double-layer force cannot describe the mutual interaction of two surfaces approaching at distances smaller than few nanometers, because (a) they are not valid at small separations; and (b) other forces arise. The theory modeling the interactions of the surfaces taking into account only Van der Waals and double-layer forces is called DLVO (Derjaguin–Landau–Verwey–Overbeek) theory [165, 166] and all other surface forces are called non-DLVO forces. The non-DLVO forces can be roughly grouped into four categories: solvation forces, repulsive hydration forces, hydrophobic attractive forces, and steric forces, which are reviewed in the forthcoming sections.

6.4.1. Theory

Solvation forces arise whenever liquid molecules are compelled to order in almost discrete layers between two surfaces. In most cases, these forces exhibit an oscillatory behavior. Consider the way liquid molecules order at an isolated surface or between two surfaces, as indicated schematically in Fig. 30. Computer simulations reveal three different behaviors of liquid molecules at interfaces. At a vapor–liquid or a liquid–liquid interface there is no oscillatory behavior in the density of the liquid, as shown in panel (A) of Fig. 30. At a solid–liquid interface liquid molecules begin to order in layers [167, 168], as shown in panel (B) of Fig. 30. Between two solid surfaces such an ordering increases, as shown in panel (C) of Fig. 30. Even in the absence of any liquid–solid interaction, geometric considerations alone compel the molecules to rearrange in order to fit between the solid surfaces. The variation of this ordering with the separation D generates the solvation force.

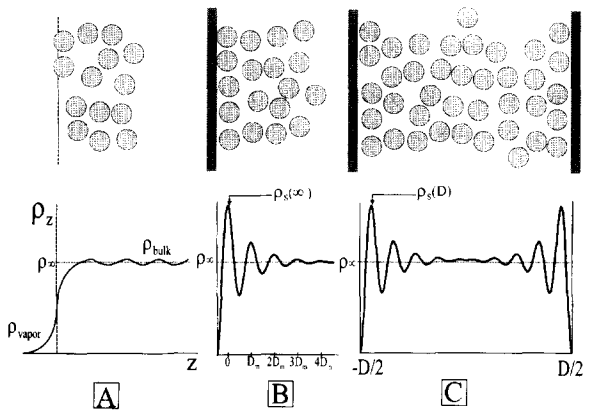

Fig. 30. Schematic representation for the ordering of liquid molecules. Panel (A): vapor–liquid interface. Panel (B): solid–liquid interface. Panel (C): between two solid surfaces. The density of the liquid as a function of position is shown. ρ_Z is the density of the liquid as a function of the distance from the interface, ρ_{vapor} is the density of the liquid molecules in the gas phase, ρ_∞ is the bulk density, $\rho_S(\infty)$ is the density of the liquid at the interface in the case of a single solid–liquid interface, $\rho_S(D)$ is the density of the liquid at the interface when a second interface is at a distance D, and D_m is the radius of the molecule (adapted from [15]).

Use of Eq. (6.56) permits the quantitative description of solvation forces. This equation can be applied to any kind of particle. Therefore, a solvation force occurs whenever there is a variation of density.

Like the density profile, the solvation pressure is an oscillatory function of distance with a period that approximately equals the molecular diameter D_m and with a range of few molecular diameters. At very small separations, when the last liquid layer has been squeezed out, $\lim_{D\to 0}\rho_s = 0$ and the pressure tends to a finite value, deduced from Eq. (6.56):

$$\lim_{D\to 0} P = -k_B T \rho_s^{\infty}. \tag{6.76}$$

Hence the contact force is adhesive.

In a first approximation the solvation oscillatory force can be described by a cosine exponentially decaying in the form [15]:

$$P(D) \cong -k_B T \rho_s(\infty) \cos\frac{2\pi D}{D_m} e^{-D/D_m}. \tag{6.77}$$

Integrating Eq. (6.77) and inserting $\rho_s(\infty) = \sqrt{2}/D_m^3$, yields the work of adhesion due to the solvation force:

$$W(0) \cong \frac{\sqrt{2}k_B T}{4\pi^2 D_m^2}. \tag{6.78}$$

Comparing this value to the work of adhesion due to the Van der Waals force, we conclude that the solvation force dominates the adhesion if the Hamaker constant is less than $0.2k_BT$, i.e., if $A < 10^{-21}$ J.

O'Shea et al., using the Derjaguin approximation, have calculated the force on a parabolic tip by integrating Eq. (6.77) [169]:

$$F(D) = -k_B T \rho_s(\infty) \frac{2\pi R\sigma}{\sqrt{4\pi^2 + 1}} \cos\frac{2\pi D}{D_m} e^{-D/D_m}, \tag{6.79}$$

in which R is the radius of curvature of the tip. Kralchevsky and Denkov [170] have obtained a semi-empirical expression of the solvation force as a function of D, D_m, and the molecule volume fraction φ_V. Their expression is

$$P(D) \cong -P_0 \cos\frac{2\pi D}{D_m} \exp\left(\frac{D_m^3}{D_{m1}^2 D_{m2}} - \frac{D}{D_m}\right). \tag{6.80}$$

P_0 is given by

$$P_0 = \rho k_B T \frac{1 + \varphi_V + \varphi_V^2 - \varphi_V^3}{(1 - \varphi_V)^3} \tag{6.81}$$

in which φ_V is the molecule volume fraction and $\rho = 6\varphi_V/\pi D_m^3$. The dimensionless period D_{m1} and the dimensionless decay length D_{m2} are given by

$$\frac{D_{m1}}{D_m} = \sqrt{\frac{2}{3}} + a_1 \Delta\varphi_V + a_2 (\Delta\varphi_V)^2, \tag{6.82}$$

and

$$\frac{D_{m2}}{D_m} = \frac{b_1}{\Delta\varphi_V} - b_2,$$

in which $\Delta\varphi_V = \pi/3\sqrt{2} - \varphi_V$, $a_1 = 0.23728$, $a_2 = 0.633$, $b_1 = 0.48663$ and $b_2 = 0.42032$.

Gelb and Lynden-Bell [171] have studied oscillatory solvation forces between a non-structured tip and a sample in a liquid by means of MD simulations and closed analytical solutions. They showed that the amplitude of the oscillations is linear with the tip radius, with the exception of the first oscillation below $2D_m$, which increases non-linearly. The number of oscillations per curve is not sensitive to tip dimension. The oscillations amplitude increases also with decreasing temperature. Neither the temperature nor tip dimensions alter the wavelength of the oscillating force. The density of the liquid has an effect both on oscillation amplitude and wavelength. With increasing density, the amplitude increases and the wavelength decreases. The authors suggested that the dependence of the first oscillatory peak on tip dimension could be exploited in order to calibrate the apex of the tip.

Subsequently, Patrick and Lynden-Bell [172] investigated the effect of structured tips and substrates, by considering an atom-ended tip and a four atoms-ended tip. They showed that, in the case of the "flat" tip, oscillations are about sixfold larger than with the atomic sharp tip. This is due to the fact that the apex atom of the sharp tip compensates the repulsive forces exerted by liquid molecules on the tip. They also showed that the sharp tip is able to trap a liquid molecule into the hole of a fourfold hollow site, thus yielding an additional peak below D_m. This additional peak is absent when the tip is located above an atop site of the substrate. The trapped liquid molecule stays between the tip and sample for 10–100 ps. Hence, the authors state the incapability of AFM to detect such a phenomenon.

6.4.2. Experimental results

The first measurement of solvation forces with an AFM has been performed by O'Shea et al. [173] in octamethylcyclotetrasiloxane (OMCTS) and dodecanol on graphite with a Si_3N_4 tip. Both curves are shown in Fig. 31. In OMCTS, there is an oscillatory force superimposed to the attractive Van der Waals force. The oscillatory force results in a series of repulsive surges followed by sudden jumps. The repulsive surge is due to the tip pushing on the structured liquid layer. When the layer beneath the tip is

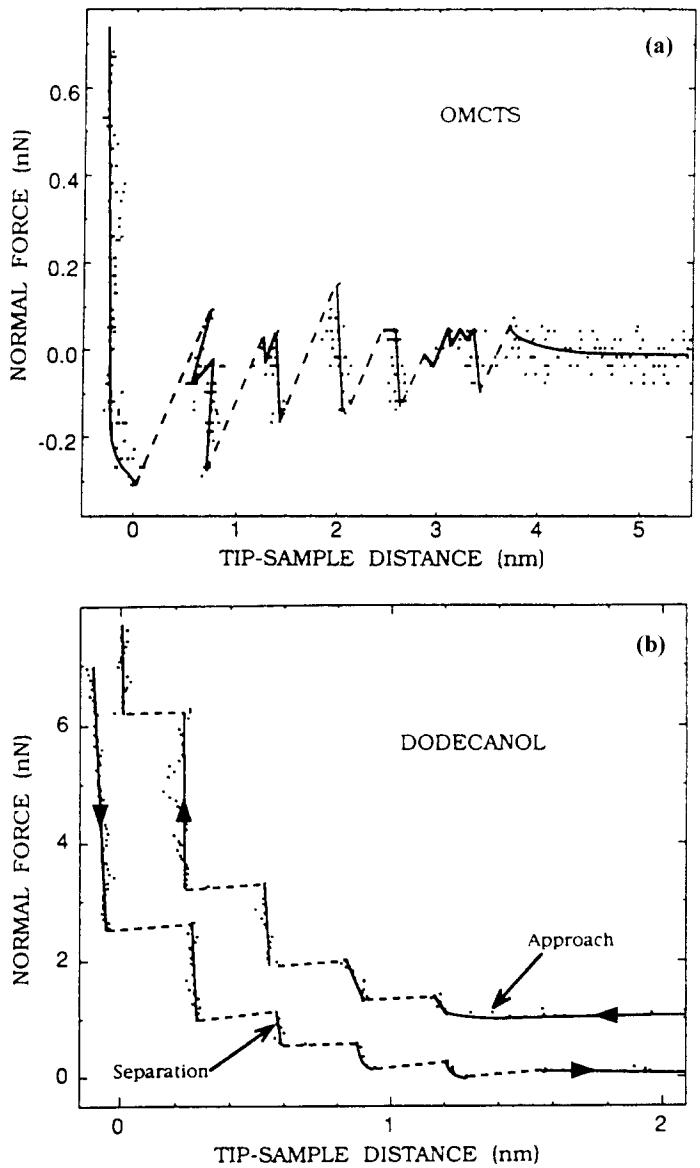

Fig. 31. Force–distance curves in octamethylcyclotetrasiloxane (OMCTS) (panel (a)) and in dodecanol (panel (b)) (reprinted with permission from [173]).

squeezed out, the tip jumps onto the next layer. The curves shown in Fig. 31 seem to have been rearranged by calculating the true tip–sample distance as explained in Section 5.1, but this is not plainly stated in the paper. The oscillations increase with decreasing distance, from $\cong 0.2$ to $\cong 0.4$ nN. The period is 0.73 ± 0.06 nm, whereas the molecule has a diameter of 0.8 nm. The small discrepancy between the diameter of the molecule and the period of the oscillations might be due to packing geometry or to errors in the calibration of distances.

In dodecanol, the oscillatory force is superimposed to the repulsive Van der Waals force. It can be observed both on the approach curve and on the withdrawal curve. The amplitude of the oscillations increases with decreasing distance from $\cong 0.5$ up to $\cong 2.5$ nN. The period is 0.35 ± 0.04 nm.

The same measurement in OMCTS has been repeated by Cappella et al. [128] on graphite. The authors were not able to measure solvation forces on mica since a few molecules of water (that are likely to remain on a cleaved hydrophilic mica substrate) are likely to destroy the ordering of OMCTS molecules.

Subsequently, O'Shea et al. [169] have acquired both static and dynamic force–distance curves, making the cantilever vibrate by means of an external magnetic field. They were able to detect solvation forces in OMCTS and dodecanol in both modes.

O'Shea et al. could not measure solvation forces in water. This has been done by Hoh et al. [174]. Force–displacement curves were acquired on a glass surface with a silicon nitride tip. The pH was adjusted between 8 and 9 in order to compensate the Van der Waals attractive force with the double-layer repulsive force. A small jump-off-contact is obtained. Recording the jumps-off-contact for several curves, discrete jump-off forces can be observed and the histogram of these jumps shows a well-defined peak at 1.2×10^{-11} N. Also a second peak can be seen, but higher multiples are lost because of peak broadening. The authors explain what they call "quantized adhesion" in two ways. Either the peaks are due to individual hydrogen bonds being resolved, or to solvation forces caused by the ordering of water layers between the tip and sample. A later experiment [175] seems to confirm this latter hypothesis.

6.5. Hydration forces

The hydration force probably arises between hydrophilic surfaces, such as silica and mica, since strongly H-bonding surface groups modify the H-bonding network of nearby liquid water molecules. This also occurs when hydrated cations in solution bind to a negatively charged surface at high salt concentration. The hydration force is probably due to the energy needed to dehydrate the ions, as indicated by the fact that the strength and the range of the force increase with the hydration number in the order $Mg^{2+} > Ca^{2+} > Li^{+} \cong Na^{+} > K^{+} > Cs^{+}$. The hydration force is exponential with the distance, but the origin of the exponential decay is still unknown.

Fig. 32 shows force–displacement curves illustrating the effects of the hydration force on mica in $MgCl_2$ solutions at different concentrations. At 3 mM $MgCl_2$ (first curve), the double-layer repulsive force can be seen. This force disappears at higher concentrations (second and third curve), but at 3M $MgCl_2$ the hydration force onsets. The shape of the curve in presence of the hydration force is not very different from that of the curve associated with double-layer force. The presence of the hydration force is inferred from theoretical considerations, since it is known that, for $[MgCl_2]>3$ mM, the double-layer force disappears.

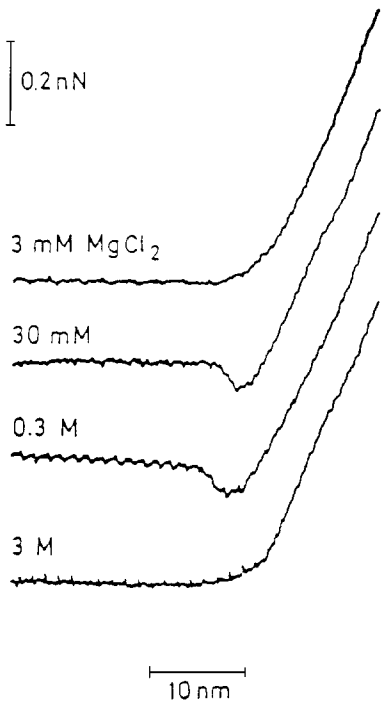

Fig. 32. Force–displacement approach curves illustrating hydration force on mica in $MgCl_2$ solutions at different concentrations. Curves are acquired at constant pH with a silicon nitride tip (reprinted with permission from [138]; Biophysical Society).

Similar forces have been observed by Butt [138] for a silicon nitride tip on mica in $CaCl_2$ and $SrCl_2$. The force in a 3M $MgCl_2$ solution has a decay length of 3 nm and is 0.07 nN strong.

Ducker et al. [17, 176] argue the presence of an hydration force between a silica colloidal sphere and a silica flat plate from the fact that, at small distances (<2–3 nm), the measured force does not follow the DLVO fit. The authors list other possible origins of such a mismatch (presence of a gel layer on the silica surface, shift in the position of the plane of surface charge). The authors have observed that the force increases with pH, i.e., with the charge on the surface.

Meagher [139] has measured hydration forces between a silica colloidal sphere and a silicon sample in 0.01 M $CaCl_2$ solutions at pH 4.1. He has shown that the theoretical curve based on DLVO theory fits the experimental data well for distances larger than 2 nm. Below 2 nm, however, a repulsive force is probed and no jump-to-contact occurs. The hydration force disappears at pH 5.3 and 1 M or at pH 10.3 and 0.01 M $CaCl_2$. These results suggest that the force is due to the specific adsorption of Ca^{2+} onto the silica surface. When the adsorption increases (because pH or ions concentration increase), the force becomes attractive and is well predicted by the DLVO theory.

Atkins and Ninham [151] have measured forces between silica surfaces in 1,2-ethanediol and water. In both solvents, for $D \geq 3$ nm, the DLVO theory can fit the data, but at smaller separations, a non-DLVO force is measured. This force can be represented by the equation

$$F = \eta R \exp(-\tau D). \tag{6.83}$$

The decay length is $\tau = 0.97 \pm 0.12$ nm for 1,2-ethanediol and $\tau = 0.41$ nm for pure water (in good agreement with other measurements). From the fact that the hydration force scales with the radius of the solvent molecules, the authors argue that the hydration force is actually an oscillatory solvation force whose oscillations are smeared out by the roughness of the tip and sample.

Biggs et al. [93] have observed hydration-like forces between gold surfaces in NaCl. Approaching the tip to the sample, an additional repulsion is observed at all concentrations. This repulsion extends over more than 10 nm in distance. The authors attribute this force to the presence of highly hydrated sodium ions near the surface, but do not discuss the differences with the case of mica surfaces.

Larson et al. [147] have observed the hydration force between silica surfaces and silicon on TiO_2 at high pH. The authors were not able to distinguish between real hydration forces and effects due to tip or sample asperities.

Karaman et al. [142] have studied the forces between an alumina surface and an aluminum or silicon nitride tip. Hydration forces are observed below 3 nm. The cause of this non-DLVO force is attributed to the formation of a thin hydrolyzed oxide gel layer near the surface. This supposition is supported by the fact that, when force–distance curves are repeatedly acquired, initially attractive forces become more and more repulsive, reflecting the characteristic time of formation of the gel layer.

Despite of the importance that hydration forces seem to have in surface science and in biology, this force is still unknown. A lot of theoretical and experimental work is needed. The study of hydration forces by AFM presents several problems. This force acts on a very small range and is in most cases very weak. Often the presence of this force is inferred from the fact that the force–distance curve cannot be fitted by DLVO equations. Errors in the determination of distances, of the Hamaker constants, of the surface charge densities or of surface potentials are likely to affect the fit and to give wrong results. Therefore, this force is rather difficult to characterize quantitatively, and depending on the system, it is not possible to single out the contribution of hydration force to the total tip–sample force.

6.6. Hydrophobic force

Attractive forces between hydrophobic macroscopic bodies in water have been measured for different systems. The origin of these forces is not well understood, although recently several hypothesis have been proposed.

1. The hydrophobic force could originate from changes of the water structure in the thin layer between hydrophobic surfaces compared to the structure of bulk water [177, 178].
2. The hydrophobic force could be the capillary force due to cavitation in the vicinity of hydrophobic surfaces [179].
3. In another hypothesis, hydrodynamic fluctuations at a hydrophobic surface/water interface are believed to correlate with those at the neighboring interface to give rise to an attractive force [180].
4. Some researchers suggest that hydrophobic force arises from correlated dipole–dipole or dipole–charge interactions [181–183].
5. Others believe that such a force is the result of dipole interactions associated with the large domains of ordered hydrocarbon chains [79, 184, 185].

Since no theory is able to explain the experimental results, data are fitted by an empirical force law in the following form [80]:

$$\frac{F}{R} = C_1 \exp\left(-\frac{D}{D_1}\right) + C_2 \exp\left(-\frac{D}{D_2}\right), \tag{6.84}$$

in which C_1 and C_2 represent the strength of the short- and long-range force respectively, and D_1 and D_2 are the respective decay lengths. The term "short-range" refers to the hydrophobic attraction with decay length of 1–2 nm.

The hydrophobic force can also be fitted by a power law:

$$\frac{F}{R} = -\frac{\Gamma}{6D^2}. \tag{6.85}$$

This equation can fit both short- and long-range hydrophobic force, but there are uncertainties about the exponent, since an exponent slightly larger than 2 can fit experimental data better [79, 184].

Rabinovich and Yoon [80] have measured the hydrophobic force between a silica plate and a glass colloidal probe hydrophobized with octadecyltrichlorosilane (ODTCS). They could measure the parameters in Eqs. (6.84) and (6.85) by measuring the jump-to-contact of the curves, according to the following relationships:

$$(C_{1,2})_{\text{jtc}} = -\frac{k_c D_{1,2}}{R} \exp\left(\frac{D_{\text{jtc}}}{D_{1,2}}\right), \quad \text{and} \quad (\Gamma)_{\text{jtc}} = \frac{3k_c D_{\text{jtc}}^3}{R}, \tag{6.86}$$

in which the subscript "jtc" means that these values are obtained with the "jump" method.

The parameters C_1, C_2, and Γ also have been calculated by fitting the whole curve. The authors show that the "jump" method gives less precise values than the fitting of the whole curve.

Values determined by both methods are correlated with advancing and receding contact angles θ_a and θ_r. For $\theta_a = 88°$, three ranges of the force are evidenced. For $\theta_a = 95°$, the force has a short- and a long-range regime, while for $\theta_a = 102°$, $105°$, and $115°$ only the long-range regime can be observed. The parameter C_2 correlates well with the advancing angle (it is smaller than 5 mN/m for $\theta_a < 95°$ and increases sharply up to 255 mN/m for $\theta_a > 95°$), while D_2 is rather insensitive to θ_a. The authors suggest that C_2 depends on the density and hence on the ordering of hydrocarbon chains, while D_2 varies with the distance between the charge or dipole domains. Increasing the density (and the contact angle) results in increasing the ordering, but does not increase the distance between domains.

If D_2 depends on the distance between charge or dipole domains, then it should depend on the Debye length. Following the theory of correlation between charges in lattice arrays on two interacting surfaces, the authors derived the following relation for D_2:

$$1/D_2 = \sqrt{K_D^2 + (\pi/d_c)^2} \Rightarrow 1/D_2^2 = 10.5z^2[\text{X}] + (\pi/d_c)^2, \tag{6.87}$$

in which d_c is the average charge or dipole distance, and z and [X] are the valence and the concentration of the electrolyte. The fit of several experimental data with Eq. (6.87) is not good at high electrolyte concentrations and some experimental data are independent of [X] (see also Ref. [186]).

The role of gas dissolved in the liquid also was investigated. No difference can be observed between curves acquired in degassed water and water in equilibrium with surrounding air, but this could be due to dissolution of air in water during the measurement. Force–displacement curves in water saturated

with argon (whose solubility is about twice that of nitrogen) show a considerably higher attractive force, and this could be explained with the formation of microbubbles. Gas microbubbles in the liquid gap act in analogous way like liquid bubbles in an air gap, i.e., they contact the tip and sample surface and exert a meniscus force. The sharp increase of the force for $\theta_a > 95°$ may support this view.

Also the adhesion force is measured. Typical values of F_{ad}/R are in the range 100–400 mN/m, and the jump-off-contact distance is in the range 20–100 nm.

Forces were measured also for an asymmetric system, i.e., a hydrophobic glass colloidal sphere on a clean hydrophilic silica plate. Only after subtracting DLVO forces, can a short-range hydrophobic force be revealed. In a later work, the same authors have confirmed these results with trimethylchlorosilane [79].

Tsao et al. [185] have studied the dependence of hydrophobic force on the temperature and on the hydrocarbon chain length by collecting force–displacement curves between a silicon nitride tip and mica in several surfactants. All the possible combinations were investigated, i.e., a bare tip and hydrophobic mica, a hydrophobic tip on bare mica, and both tip and mica coated with hydrophobic layers. The surfactants employed are in order of length: dihexadecyl-dimethyl-ammonium (DHDA), dioctadecyl-dimethyl-ammonium (DODA), dieicosyl-dimethyl-ammonium (DEDA), and didoeicosyl-dimethyl-ammonium (DDDA).

The authors show that, in water and at room temperature, the force is weaker for the shortest chain (DHDA), and that the force is stronger for the hydrophobic mica–bare tip system than for the bare mica–hydrophobic tip system, whereas for the symmetric situation the force is much weaker. These results are in contrast with the results of Rabinovich and Yoon, and these two latter authors believe that Tsao et al. have not accounted for DLVO forces.

When raising the temperature, both DHDA and DODA show only the Van der Waals attraction, while the force for DEDA is substantially the same. This result correlates well with the chain transition temperatures in water.

Hydrophobic forces are present also in ethylene glycol. In this solvent, the force is the same for DDDA and DEDA, but smaller for DODA. As a matter of fact, the melting temperature of DODA in ethylene glycol is comparable with the melting point of DHDA in water (34°C and 35°C). The fact that hydrophobic forces have been observed in solvents different from water indicates that this force cannot be attributed to the unique structural properties of water. Further, the force is associated with the solid phase of the surfactant, and disappears as the melting point is approached. No long-range attractive hydrophobic forces were observed when a bare Si_3N_4 tip approached either a Teflon or polyethylene substrate in either water or ethylene glycol, indicating that these two polymeric surfaces do not possess specific molecular structures that give rise to the hydrophobic force. Finally, the force depends on salt concentration.

Similar results were obtained in another work [187] measuring forces for DHDA, DEDA and DODA at 25°C, 40°C, and 50°C. The first derivative of the force can be fitted with Eq. (6.84). All parameters (i.e., both the force strength and the force decay length) decrease with increasing temperature for any surfactant. The correlation between the force and the chain order is studied by means of molecularly resolved AFM images.

Rabinovich et al. [184] have correlated the results of Tsao et al. with the order parameter S of the hydrocarbon chain defined as $S = (3\langle\cos^2\gamma\rangle - 1)/2$, where γ is the angle between the axis normal to the surface and the molecular axis. When $S = 1$, all molecules are parallel to each other and perpendicular to the surface, whereas when the molecules are randomly oriented, $S = 0$. They showed that the

parameters C_1, C_2, D_1 and D_2 found by Tsao et al. have a linear dependence on S and that C_2, D_1 and D_2 are proportional to S, while for C_1 there is a critical parameter $S_{cr} \cong 0.3$, below which the short range hydrophobic force ceases to exist. Also the parameter Γ shows a linear dependence on S for $S > 0.3$, and is zero for $S < 0.3$. The authors explain such a dependence as arising from the changes in water structure induced by the ordering of the hydrocarbon chains. The changes in water structure may in turn create dipole domains which are comparable in size with the observed decay length.

Forces also differ for a single-chain surfactant and a double-chain surfactant, in that single-chain surfactants have only the short-range term. This effect can be explained with ordering considerations. On the one hand, since the adsorption is controlled mainly by the Coulomb attraction between the polar head and the negative charge site on the mica substrate, the area occupied by each single-chain molecule is actually the area per charge site ($\cong 0.5$ nm^2). This area is approximately twice as large as the cross-sectional area of the hydrocarbon chain. As a result, the hydrocarbon chain are disordered and exhibit only the short-range hydrophobic force. On the other hand, the double-chain molecules give rise to large values of S and consequently to long-range forces.

Mantel et al. [188] have measured forces between a silanated glass colloidal particle and stainless steel. They found that hydrophobic forces are absent in the non-treated stainless steel that contains a certain amount of hydrophilic potassium salt (2%). When the stainless steel is treated with Ar plasma and then rinsed with water or simply rinsed with water, the potassium decreases and the hydrophobic force onsets. The authors argue that, when hydrophilic and hydrophobic groups are present in close proximity on a surface, the attractive hydrophobic force and the repulsive hydration force, both arising from changes in water structure, are not simply additive.

Several studies have addressed the interaction of an AFM tip with bubbles or droplets in water. Even if they are not directly related to hydrophobic force, these results are reviewed in this section, since some evidences exist that hydrophobic interactions could also arise from microbubbles in water.

Butt [189] has acquired force–displacement curves and force–time curves between a glass colloidal particle and an air bubble in water. When the glass particle is hydrophilic, force–displacement curves show a repulsive region when the tip and the bubble are in contact. Several oscillations are observed on such contact lines. These oscillations are reproducible when the force is kept below a certain threshold value and become hysteretic if the force exceeds the threshold value, because the particle snaps into the bubble. When the glass particle is hydrophobic the curve is completely different. A strong attractive force makes the tip snap into the bubble and a very high force is needed to pull it out of the bubble. Looking at the time-resolved analysis of the signal, an oscillatory behavior of the acceleration can be noted. The attractive force is calculated between 580 and 1000 nN. Also the forces between a glass particle and a water droplet in air are considered. The system hydrophilic tip–water droplet is analogous to the hydrophobic glass sphere–air bubble. The tip snaps in at a certain distance with a force between 230 and 406 nN, but the time-resolved analysis reveals that the process is 2–4 times faster, probably because of the lower effective mass of the cantilever in air. Also the hydrophobic glass snaps into the water droplet. The author has offered no explanation for this result.

Ducker et al. [190] have acquired force–displacement curves between a silica colloidal particle and an air bubble in water. When the silica particle was hydrophobic their results are in agreement with those of Butt. Also in the case of an hydrophilic silica particle an attractive force of about -0.2 mN/m is detected. After the tip has jumped into contact, the curves show a contact line from which the stiffness of the air bubble can be measured (0.065 ± 0.005 N/m). This contact line is probably due to the presence of a thin wetting film between the silica particle and the air bubble and the repulsive force is

associated with the high energy needed to squeeze it out. The attractive force cannot be accounted for by the sum of the force needed to squeeze out the wetting film and of the DLVO force. The sum of the jump distances due to these two forces is 26 nm, while the measured jump distance is 44 nm. By measuring jump-in distances at different salt concentrations, the authors ascertained that the force was not electrostatic. When sodium dodecylsulfate (SDS) is adsorbed at the air–water interface, forces become repulsive and are in good agreement with DLVO theory at all distances, with deviations only below 2 nm. The deviations are now repulsive. The measured forces are interpreted on the basis of capillary bridging forces. When the tip is pushed against the sample, the air bubble "wets" the tip surface and exerts an attractive force, even when the tip is hydrophobic. Also hydrophobic forces are interpreted as arising from the air microbubbles nucleation between the two surfaces.

6.7. Specific forces

Specific forces are non-covalent forces that generate very strong adhesion between molecular groups. The term "specific force" is somewhat ambiguous, but can refer to all forces that are present only between a specific pair of molecules. Most of the interactions between biological molecules are due to specific forces. The specific bond between a couple of molecules arises from the cooperation of several non-covalent bonds (e.g., hydrogen or ionic bonds) favored by the geometry of the interacting molecules. The two molecules may fit together by means of a "lock and key" mechanism. Specific bonds, like covalent bonds, have a precise stoichiometry.

In order to measure specific forces with the AFM, it is necessary to functionalize the tips by covering them with one of the two molecules under study. A typical withdrawal curve between a tip functionalized with odorant binding protein (OBP) and a sample functionalized with its antibody is shown in Fig. 33. At a distance of 7 nm from the contact point, there is a jump-off-contact of 230 pN due to

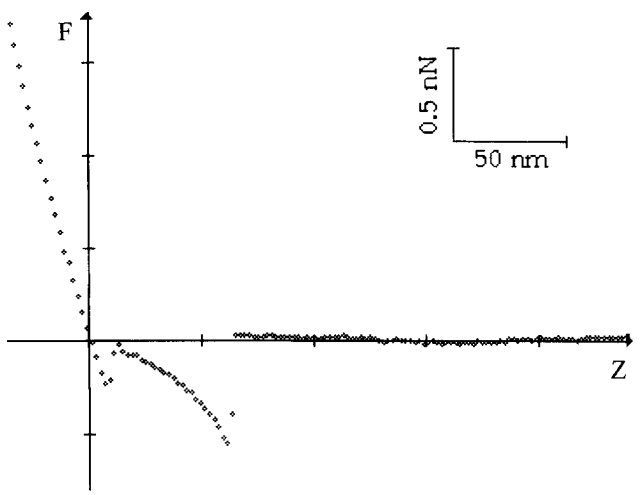

Fig. 33. Withdrawal force–displacement curve with specific adhesion between odorant binding protein (OBP) and anti-OBP. After the jump-off-contact, there is a non-linear attractive surge due to the stretching of a group of OBP molecules, that suddenly breaks at a distance of 65 nm.

aspecific adhesion (mainly Van der Waals force). After the jump-off-contact, the cantilever returns to the rest position (zero deflection). The tip and sample seem to be detached, but some OBP and antibody molecules are still bound by bonds which are stretched along the subsequent attractive surge until the force reaches a rupture value. The discontinuity of 550 pN at a distance of 65 nm marks the detachment due to the rupture of the specific bonds between the OBP and its antibody. Since the complementary molecules may be located at different points on the tip and on the sample, they may detach at different distances, and hence a specific force–displacement curve may present multiple detachments. The rupture occurs at a distance of 65 nm because the sample undergoes important deformations and because a whole group of OBP molecules is likely to be stretched.

In principle, the jump-off-contact and the specific detachment may overlap so that the specific force is hidden by the aspecific (Van der Waals) adhesion. In some works this problem is solved by acquiring curves in a particular liquid that has a small Van der Waals force. In some others, one or both of the interacting molecules are attached to the tip and/or to the sample via a spacer. The spacer is a molecule few nanometers long which is stretched during the detachment and makes the rupture of the bond occur at distances greater than those of the aspecific detachment. The curve in Fig. 33 is acquired with the antibody bound via a spacer.

In general, four different parameters can directly be extracted from specific force–displacement curves:

(1) the force of a single binding event;
(2) the rupture distance depending on the length of the molecules involved and on how they are immobilized;
(3) the adhesion probability, i.e., the ratio between the number of force–displacement curves with specific detachment and the total number of force–displacement curves, depending on surface coverage and experimental conditions; and
(4) the elasticity of the stretching region.

The first study on specific forces with the AFM is that of Florin et al. [20], who measured the forces between avidin and biotin molecules. They used Si_3N_4 commercial tips functionalized with avidin on agarose beads functionalized with biotin. The measured adhesion between the two surfaces is of about 20 nN. When blocking the surfaces with an excess of free avidin or biotin, the adhesion diminishes down to $\cong 200$ pN. The force–displacement curve displays both the jump-off-contact of about 1 nN and the specific detachment occurring at different distances. The forces do not diminish in presence of excess bovine serum albumin (BSA), which proves the specificity of the interactions. Histograms of the measured rupture forces show several regularly spaced peaks, that correspond to multiples of an elementary force of 160 ± 20 pN. This force is attributed to the interaction of a single avidin–biotin couple. In similar experiments carried out with quite hard substrates (silicon oxide instead of agarose beads) no quantized adhesion is found. A likely explanation is that the soft agarose bead allows the molecules to arrange parallel to each other, so that the force does not depend on the relative positions. This is not possible with hard substrates. As a matter of fact, the spacer is often employed also to make the molecules more mobile and to allow such a rearrangement. Measurements have been repeated with desthiobiotin and iminobiotin, leading to the identification of an elementary force of 125 ± 20 and 85 ± 15 pN, respectively.

In a later work [191], the same authors have showed that there is a meaningful correlation between the measured elementary forces and the enthalpy of the system.

Lee et al. [192] have measured the forces acting in the following three systems: biotin–biotin, biotin–streptavidin blocked with biotin, and biotin–streptavidin. The force between biotin and biotin is characterized by a repulsive steric or hydration force and no adhesion is present. Between biotin and blocked streptavidin there is an adhesion force of 60 ± 40 pN. This adhesion force may be due either to the increase of the Hamaker constant or to the decrease of the repulsive force. The interaction between biotin and streptavidin is dominated by an adhesion of 340 ± 120 pN. The authors note that, because of steric limitations due to the immobilization of molecules on the surfaces, not all the biotin molecules within the contact area (nearly 10 molecules) bind a streptavidin molecule. They observe that no specific forces can be measured with a sharper tip.

The same kind of measurements have been performed by Allen et al. [193]. No adhesion is observed when the streptavidin is blocked, and the specific force turns out to be 409 ± 166 pN.

Bowen et al. [194] have measured the forces between a tip and a sample both functionalized with bovine serum albumin (BSA). The forces are studied at different NaCl concentrations and at different pH.

Lee et al. [195] have measured specific interactions between DNA strands. All experiments are performed in a 0.1 M NaCl solution. In a first experiment the forces between two complementary strands, namely $(ACTG)_5$ and $(CAGT)_5$, are measured. The adhesion forces are found to be grouped in four categories. One of these (0.48 ± 0.1 nN) corresponds to the non-specific force between non-complementary strands, the other three correspond to interactions between DNA oligonucleotides of 12 (0.83 ± 0.11 nN), 16 (1.11 ± 0.13) or 20 (1.52 ± 0.19) base pairs. Since the oligonucleotides have different lengths, the bond breaks at different distances and forces. In a second experiment both the tip and the sample are functionalized with cytosine. On the tip, inosine polymers of 160 base pairs are bound to the cytosine. In withdrawal curves, retarded detachments at distances of about 240 nm can be observed with specific forces between 1 and 2 nN. These detachments are due to the bond between the inosine and the cytosine on the sample, and 240 nm is the length of the inosine polymer. Forces between couples of cytosine polymers also can be measured.

Boland and Ratner [196] have measured the hydrogen bonding between DNA complementary pairs (adenine–thymine and cytosine–guanine). The histograms of the attractive forces show in both cases quantized forces with an elementary force of 54 pN. The attractive and adhesive force turn out to be the sum of 12 and about 60 base pair interactions, respectively. Several control experiments with non-complementary base pairs and bare surfaces are performed.

Noy et al. [197] have measured the forces between two complementary DNA 14-mers fixed on a gold surface via $HS(CH_2)_{16}$ spacers. The force–displacement curve between DNA strands has the typical shape of the curve in Fig. 33. The specific adhesion is of 0.45 nN (one couple) or of 0.9 nN (two couples) and the detachment occurs at a distance of about 18 nm. When employing two non-complementary DNA strands, force–displacement curves show a jump-off-contact of about 100 pN at zero separation. The authors have also studied the stretching of the DNA duplex formed before the detachment. They observe that the part of the curve between the origin and the specific detachment, i.e., the part resulting from the stretching of the duplex, is characterized by three regions: a short elastic region, a pronounced flat region where the separation increases rapidly under almost constant force (indicative of a structural transformation), and a relatively stiff elastic region immediately prior to duplex separation. The elastic constant of the DNA duplex before and after the structural transformation is determined. The qualitative and quantitative results obtained by Noy et al. are in agreement with some theoretical predictions.

Nakagawa et al. [198] have measured the forces between trichlorosilanes of different length. The experiments are performed in ethanol in order to decrease the Van der Waals adhesion. The force is found to be proportional to the length of the chain for $n \geq 8$, whereas there is no specific force for $n < 8$, since the chains are randomly oriented and do not bind to each other.

Dammer et al. [199] have measured the specific forces between biotin and anti-biotin molecules. The adhesion force between the two functionalized surfaces is between 100 and 200 pN, while it is almost zero for the non-functionalized tip. The authors carry out several control experiments (non-functionalized tip, blocked tip or sample, low and high pH, and non-specific antibody) in order to ensure the measured forces to be specific. In these control experiments the measured adhesion is between 20% and 40% of the specific adhesion. The most interesting control is the one at low and high pH. When the pH of the solution is changed, the ionic and hydrogen bonds cooperating in the specific bond are affected, and the specific interaction may disappear. By blocking the biotin on the tip, it is possible to decrease the interaction force, and the histogram of the force values shows four peaks that are multiples of an elementary force of 60 ± 10 pN.

Antigen–antibody specific forces also have been measured by Hinterdorfer et al. [200] taking advantage of the complex human serum albumin (HSA)–anti-HSA. The authors solve the problem of distinguishing aspecific and specific adhesion by introducing a spacer (polyethylene glycol PEG, 8 nm long) between the tip and/or the sample and the molecules. The elementary force is about 240 pN and the rupture distance goes up to 30 nm, which is the sum of the lengths of one HSA molecule, one anti-HSA molecule and two PEG molecules. Both the values of the rupture force and distance indicate that individual molecule–molecule bonds have been measured. The distribution of the rupture lengths is bimodal. The two different distances correspond to the detachment of the two arms of the asymmetric antibody molecule.

Stuart and Hlady [201] have measured the forces between fluorescein and anti-fluorescyl IgG. They have observed that the strength of the specific force and the overall shape of the curve depend on the contact time between the tip and sample. When the tip and sample are allowed to stay in contact only for 2 s, no adhesion is observed. When the contact time is increased up to 1 or 2 min, the adhesion increases up to nearly 4 nN and the jump-off-contact distance is 200 nm (1 min) or 400 nm (2 min).

Allen et al. [202] have directly monitored specific interactions between ferritin and anti-ferritin in an immunoassay system. The measured forces are quantized with steps of 49 ± 10 pN. This elementary force is attributed to individual unbinding events.

Vinckier et al. [203] have measured specific forces between the chaperonin GroEL and several proteins (synthase, lactamase, bovine serum albumin, and peroxidase). Forces are measured with and without ATP in solution and both with native and denatured proteins. The authors have verified that, for all proteins, the forces are greater in the denatured form than in the native form. The forces in presence of ATP are greatly reduced, since the ATP modifies the GroEL structure. This happens both for native and denatured proteins. The non-hydrolyzable ATP analog, the ATPγS, does not affect the forces. The authors have shown that the specific interaction depends on the hydrophobicity of the tip. Hydrophilic functionalized tips do not interact with GroEL, while hydrophobic functionalized tips show the same interaction as tips functionalized with proteins. Finally the authors have studied the dependence of the measured force on the tip diameter. The force between GroEL and lactamase goes from 110 pN for a tip diameter of 35 nm up to 380 pN for a tip diameter of 160 nm.

Nakajima et al. [204] have studied the actin–heavy meromyosin (HMM) interaction, with a single HMM molecule bound onto the tip surface via a long chain made up of biotin, ultravidin, and

acrylamide. The force–displacement curves look like the curve in Fig. 33, but sometimes the jump-off-contact overlaps with the specific detachment. The histogram of the pull-off forces is bimodal with peaks at 14.8 and 24.7 pN. The two forces correspond to the binding of only one head or of both heads.

Dammer et al. [205] have measured the forces between proteoglycans which are involved in cell adhesion (AP). The pull-off is once again retarded due to the lifting and extending of string-like arms. In 10 mM Ca^{2+} the mean force is 125 pN and the probability of binding is 60%. The force and the probability are greatly reduced in 2 mM Ca^{2+} and 2 mM $Ca^{2-} + 10$ mM Mg^{2+} (40 pN and 12%), showing that the AFM measurement is able to assess the Ca^{2+}-selectivity of an interaction. Also control experiments with a blocking antibody have been performed. Subsequently, Fritz et al. [206] have studied the elasticity of the proteoglycans and have addressed the extension dependence of the force. These authors have found that the extension dependence of the force is non-linear and that two fundamental phenomena contribute to this non-linear response. At low force regimes (below some 10 pN) the response is dominated by entropic effects and the cantilever works against a random thermal motion, which tends to curl the molecule. At higher forces, the elasticity of single-chain segments has to be considered. The data of Fritz et al. are best fitted by an empirical formula which considers only the entropic elasticity [207]. If X is the extension of the molecule, the force due to entropic elasticity is described by

$$F(X) = \frac{k_B T}{\Xi}\left[\frac{1}{4}\left(1 - \frac{X}{\Sigma}\right)^{-2} - \frac{1}{4} + \frac{X}{\Sigma}\right], \tag{6.88}$$

in which Ξ is the persistence length and Σ is the contour length. If the chain molecule is represented as a chain of N freely joint rigid rods, the persistence length is defined as the length of each rod and the contour length as $N\Xi$.

Kikuchi et al. [208] have studied the stretching of polystyrene chains and have fitted the extension–force law with the extended Langevin equation:

$$X(F) = \left[\coth\left(\frac{lF}{k_B T}\right) - \frac{k_B T}{lF}\right]\left(n_m l + \frac{n_m F}{k_m}\right), \tag{7.89}$$

in which X is the extension, F the force, l the length of the monomer, n_m the number of monomers, and k_m is the elastic constant of the monomer.

Bowen et al. [209] have functionalized the tip with a cell, namely a yeast cell (*Saccharomices cerevisiae*). They have measured the adhesion of the cell onto a mica surface. After a first jump-off-contact, there is a long stretching region (about 200 nm) in which the attractive force increases slowly until the cell detaches from the surface. Such curves are contact time dependent. If the contact time is increased to 5 min, then the adhesion increases and the stretching region becomes longer (about 500 nm).

Another group of experiments deals with the determination of the single bond force for other kind of forces (mainly Van der Waals and hydrogen bond). In these experiments the tip is functionalized with a non-biological molecule. So, strictly speaking, the measured forces are not specific. This kind of AFM measurements is often called "chemical force microscopy", since the functionalized tip behaves as a chemical sensor.

Van der Vegte and Hadziannou [210] have measured the forces between the chemical groups listed in Table 8. All measurements have been performed in ethanol. Once the adhesion force is measured, the

Table 8
Measured mean adhesion in nN and single bond force in pN (bold) between the listed functional groups as determined in Ref. [210]. All measurements have been performed between functionalized tips and samples in ethanol.

	Substrate									
tip	CH_3		OH		NH_2		COOH		$CONH_2$	
CH_3	0.9	**81**	0.3	**57**	0.3	**59**	0.3	**61**	0.3	**60**
OH	0.1	**50**	0.9	**101**	1.2	**113**	1.2	**112**	1.4	**117**
NH_2	0.2	**54**	0.5	**88**	0.8	**98**	0.7	**95**	0.9	**100**
COOH	0.7	**95**	1.2	**109**	1.2	**105**	1.3	**114**	2.2	**137**
$CONH_2$	0.3	**62**	1.3	**110**	1.2	**102**	2.2	**125**	1.8	**120**

JKR theory is applied in order to determine the surface energy γ and the single bond force. The number of interacting molecules is given by the ratio between the contact area, determined by means of JKR theory, and the characteristic area of the molecules. The elementary force is the total adhesion divided by the number of molecules. The trend expected on the basis of the kind of interactions governing the adhesion is qualitatively observed. In the case of a CH_3-modified tip, for which only the Van der Waals interaction plays a role, small adhesive forces are found. The cohesive CH_3–CH_3 Van der Waals interaction is larger than the Van der Waals force for dissimilar pairs, e.g., CH_3–COOH. As regards OH, NH_2, COOH, or $CONH_2$ tips, again the pure Van der Waals interaction with a CH_3 surface gives the lowest adhesive force. The measured hydrogen bond forces are in qualitative agreement with hydrogen bond energies.

Williams et al. [211] have developed a method to calculate the single bond forces. This method is based on Poisson statistics. The distribution of adhesion forces in an AFM experiment can be modeled with the Poisson statistics provided the two following assumptions are satisfied:

(1) the total adhesion force is the sum of a finite number of discrete, independent chemical bonds;
(2) these bonds form randomly, and have similar force values. Accordingly, if the single bond force is F, the mean force $\bar{F}$ and the variance σ_F^2 are given by

$$\bar{F} = mF \quad \text{and} \quad \sigma_F^2 = mF^2, \tag{6.90}$$

in which m is the mean number of events, i.e., of bonds. The single bond force can be calculated as

$$F = \frac{\sigma_F^2}{\bar{F}}. \tag{6.91}$$

If an additional aspecific force F_0 is present, then

$$\bar{F} = mF + F_0 \quad \text{and} \quad \sigma_F^2 = mF^2 = F\bar{F} - FF_0. \tag{6.92}$$

Thus a plot of σ_F^2 versus $\bar{F}$ gives both the single bond force (the slope of the linear plot) and the aspecific force (the intercept of the line is $-FF_0$). The authors determine the single bond force for the Van der Waals force and for the hydrogen bond by measuring forces between a Si_3N_4 tip and gold or mica, respectively. Measurements are performed in water. Different values of the mean force are obtained with different tips of randomly varying R. The Van der Waals single bond force is 60 ± 3 pN

and the hydrogen bond force is 181 ± 35 pN. Van der Vegte and Hadziannou have compared their results with the one of Williams et al. verifying that the two are in good agreement. The same result for the Van der Waals single bond force had been previously found by Han et al. [212]. In this latter work, Van der Waals and hydrogen single bond forces have been measured in several liquids. The elementary Van der Waals force between an Si_3N_4 tip and a gold surface is 59.7 ± 4.2 pN in water and 29.2 ± 4.2 pN in propanol. As regards the COOH-functionalized tip and sample, only the measurement in hexane gives good results for the hydrogen bond elementary force. As a matter of fact, by analyzing the distance dependence of the force, the authors find a power law of -3 (i.e., the expected value for hydrogen bond interaction) only in hexane. The elementary force is 70.6 ± 2.4 pN. In water and propanol the interaction is repulsive, and is due to the double-layer force.

Subsequently, the hydrogen bond elementary force has been measured by functionalizing the tip and sample with SH- or OH-terminated silanes [213] or CH_2Br or CH_3 terminated silanes [214]. In the first experiment forces are measured in water, $(CH_3)_2SO$, and propanol. The OH–OH single bond force in water is 119 ± 16 pN. The single bond force is linearly dependent on the dielectric constant of the medium and the value in vacuum is extrapolated to 362 ± 10 pN for OH–OH and to 136 ± 6 pN for SH–SH. In the second experiment forces are measured in water, methanol, and propanol. The hydrogen bond elementary force between unmodified Si_3N_4 tips and unmodified SiO_2 substrates in water is 236 ± 20 pN. The Van der Waals single bond force between bromo-undecyl-trimethoxy-silanes is 31 ± 5 pN in water, 75 ± 11 pN in methanol, and 101 ± 3 pN in propanol. Finally, the force between octa-decyl-trimethoxy-silanes has a single bond force of 658 ± 68 pN in water and of 281 ± 35 pN in propanol. The authors have suggested that these rather high values of force are due to a hydrophobic interaction.

Thomas et al. [215] have measured the elementary forces for the systems CH_3–CH_3, NH_2–NH_2, COOH–COOH, and NH_2–COOH, taking advantage of their force feedback controlled AFM (see Section 3.2). Measurements are performed in an evacuated chamber successively filled with dry N_2. The force feedback method allows the authors to sample the whole curve and hence to work in dry N_2. The work of adhesion and the single bond energy are determined on the basis of DMT theory. As in the work of van der Vegte and Hadziannou, the CH_3–CH_3 interaction is a pure Van der Waals interaction and the calculated surface energy ($30\ mJ/m^2$) is in agreement with Lifshitz theory. All other interactions are interpreted as hydrogen bond interactions.

Van der Vegte and Hadziannou [216] have studied the pH dependence of the adhesion between a tip and a sample both functionalized with the same acidic or basic group. The curves depicting such a dependence resemble the solution titration curves for acids. Furthermore, the authors have deduced the degree of ionization and the effective pK from force–displacement curves. For COOH and PO_3H_2 the adhesion decreases for $pH > 4$ and reaches zero for $pH = 10$. The initially strong adhesion is due to hydrogen bonds, whereas the final zero adhesion is due to the double-layer force that increases as more and more COOH or PO_3H_2 groups become deprotonated. In the case of the diprotic acid PO_3H_2 the two steps in the ionization, i.e., $PO_3H_2 \rightarrow PO_3H^-$ and $PO_3H^- \rightarrow PO_3^{2-}$, are clearly observed. In the case of NH_2, the adhesion is zero for $pH < 4$ and then increases with pH. The initial zero adhesion is due to the fact that, at low pH, the NH_2 groups are positively charged (NH_3^+) and give rise to a double-layer repulsion. Finally, the adhesion is pH-independent for the CH_3 groups.

All the experiments dealing with the determination of specific forces have demonstrated the importance of the techniques based on functionalized tips. Functionalized tips have a chemical selectivity that greatly enhances the capabilities of the AFM in studying biological interactions and

mechanisms of molecular recognition. Specific forces, single bond forces, the stretching of molecules and acid–base interactions have been extensively investigated. A lot of work is still necessary, however, in order to clarify several details of such measurements and to make the technique reliable and simple to perform.

6.8. Steric, depletion, and bridge forces

Steric forces arise when the interacting surfaces are spatially diffuse, i.e., they have thermally mobile surface groups. A common type of thermally diffuse surface is a surface covered with chain molecules which dangle out into the solution, e.g., a polymer-covered surface. When another surface is approached confining these dangling chains in a well-defined volume, a repulsive entropic force known as "steric" or "overlap" force arises.

The extension of a polymer chain into the solution depends on three interactions: the solvent–solvent, the monomer–monomer, and the monomer–solvent interaction. If the solvent is a "θ" solvent, i.e., the polymer–solvent interaction is equivalent to the polymer–polymer interaction, the root mean square radius of the polymer coil R_g is given by $R_g = l\sqrt{n_m}/\sqrt{6}$ [217], where n_m is the number of monomers and l is the length of a monomer. In real solvents the effective size of the coil is referred to as Flory radius R_F [217]. In a "good" solvent there is a repulsion between the monomers and $R_F \cong l n_m^{3/5}$. In a poor solvent the polymer collapses to a globular shape. The thickness of the polymer layer T_L depends also on the coverage of surface. If N is the number of chains per unit area, in a good solvent T_L is given by [15]:

$$T_L = \sqrt[3]{N} R_F^{5/3}. \tag{6.93}$$

Once two polymer-covered surfaces are closer than $2T_L$, there is a repulsive pressure $P(D)$ given by [218]:

$$P(D) \cong k_B T N^{3/2}[(2T_L/D)^{9/4} - (D/2T_L)^{3/4}], \tag{6.94}$$

in which D is the distance between the surfaces.

Eq. (6.94) is the expression of the steric repulsion. The first term in Eq. (6.94) is the osmotic repulsion between the coils favoring their stretching, while the second term comes from the elastic energy of the chains acting against the stretching. The energy scales as $D^{-5/4}$ at short distances and as D^{-2} at large distances [218]. For $0.2 < D/2T_L < 0.9$ the pressure is adequately described by [218]:

$$P(D) \cong 100 k_B T N^{3/2} \exp\left(-\pi \frac{D}{T_L}\right). \tag{6.95}$$

When the surfaces are closer than R_g the coils are pushed out of the gap resulting in a reduced polymer concentration between the surfaces. Another kind of force arises, no longer due to the confining of the dangling chains which have now been pushed out. This new force is called the depletion force. If the polymer concentration is ρ, applying the contact value theorem, Eq. (6.56), yields the attractive depletion free energy per unit area [15]:

$$\lim_{D \to 0} W = -\rho R_g k_B T \tag{6.96}$$

Fleer et al. [219] have deduced the depletion force in the form:

$$F = \pi \frac{\mu}{V_m}(D + 2R)(D - 2T_L), \tag{6.97}$$

in which μ is the chemical potential of the solvent, V_m the solvent molecular volume, and R is the radius of the tip. The net interaction between two polymer-covered surfaces depends also on the polymer–surface interactions and on the availability of free binding sites on the opposite surface. If there are free binding sites on the opposite surface, some polymer coils will form bridges between the two surfaces and give rise to an attractive bridging force. The bridging force decays roughly exponentially with distance, with a decay length that is close to R_F.

Biggs [220] has measured the forces between a surface covered with polyacrilic acid (molecular weight $M_w = 750\,000$, $R_g = 56$ nm) and a zirconia colloidal probe of radius $\cong 300$ nm. After checking that the forces between the probe and a zirconia plate can be completely described by the DLVO theory, the forces between the probe and polymer-covered surface are measured. At high coverage, the measured force on approach increases approximately exponentially from 180 to 20 nm. From 20 nm down to contact a much steeper force is observed. Note that 180 nm corresponds to $3.5R_g$. The same features are observed in the withdrawal curve. However, between 0 and 20 nm, the withdrawal force is always lower than the approaching one. The non-exponential force at $D < 20$ nm is attributed to a severe restriction of the degrees of freedom of the polymer and/or to surface roughness. The interaction energy scales as $D^{-5/4}$ for $D < 20$ nm and as D^{-2} for $D > 20$ nm. At lower concentration there is a bridging force between the two surfaces that extends up to 2 μm.

Similar results have been obtained by Frank and Belfort [221] with extracellular polysaccharides (EPS) of varying molecular weight. Bridging forces are present both for anionic EPS and for anionic dextran and extend up to 1300 and 400 nm, respectively. No adhesion is observed. Bridging forces are absent in the case of neutral EPS. The authors have addressed also the effects of the ionic strength of the solution and have showed that bridging forces disappear in a 0.1 M KCl solution (see also Ref. [222]).

Braithwaite et al. [223] have studied the forces between a glass surface and a glass colloidal particle both covered with polyethylene oxide ($M_w = 56\,000$). The force–distance curves acquired after 35 min of incubation show a weak jump to contact at a distance of 45 nm ($5R_g$) and few bridging events due to some dangling polymers adsorbing to free binding sites onto the tip. The withdrawal curve has a slide-off-contact behavior. If sufficient time elapses (e.g., 24 h), the surface is fully covered by the polymer, and no bridging occurs. Only an exponential repulsion, beginning at 90 nm ($12R_g$), is present. If the time of incubation is very long, e.g., some days, force–distance curves are not reproducible. Their common features are an exponential repulsion beginning at very large distances (e.g., 1600 nm) and an irregular slide-off-contact with multiple stages of detachment. When covering only one of the surfaces, one would expect that the bridging events increase, since in this case one of the surfaces is entirely available for polymer adsorption. Measured curves do not support this supposition. The authors have attributed the discrepancy to the rather high scan rate. Finally, the authors have proved that the interactions between polymer-covered surfaces depend on repeated contacts. If the scan rate is high compared to the relaxation time of the polymer and the exerted loads are important, both attractive and adhesive forces change with repeated contacts. In particular, the adhesion diminishes.

Ducker and Clarke [224] have studied the forces between a silicon nitride tip and a silicon nitride flat surface in solutions containing a zwitterionic surfactant adsorbed on the surfaces. A steric repulsion of

about 2 nN is observed in approach and withdrawal curves from 5.2 down to 3.3 nm. The thickness of the two surfactant bilayers, measured by X-ray diffraction, is 4.6 nm. Repeating the contact on the same point of the sample for several times (300), the adhesion diminishes, and the range of the repulsive force extends a distance approximately equal to an additional bilayer. If the tip is moved to a new position, the shape of the curve returns to the previous one.

Steric and bridge forces depend not only on the repeated contacts, but also on the scan rate. Biggs [225] has acquired force–distance curves between a zirconia colloidal probe ($R = 2$–$3\,\mu m$) and a zirconia plate covered with polyvinyl pyrrolidone (PVP) ($M_w = 40\,000$). The curves show a steric repulsion on approaching and several bridging events on withdrawal. The bridging events occur at rather small distances (40–80 nm) and assume the shape of small attractive surges similar to those obtained with functionalized tips (see Fig. 33). The steric force begins at a distance of 70–80 nm ($\cong 5R_g$). Force–distance curves are acquired at different scan rates (9.8 – 0.1 Hz). Differences between the data at 1 Hz and below are insignificant, but, at higher scan rates, the steric force becomes steeper and steeper as the scan rate increases. These data indicate that there is a limiting collision velocity below which the response of the repulsive potential is rate independent. Also the bridge force depends on the scan rate. The jump-off-contact and the bridging events are present only at scan rates of 1 Hz or lower (see also Ref. [222]).

The weakness of the depletion force relative to the double-layer and the Van der Waals forces has made the measurement of this force particularly difficult. Milling and Biggs [226] have measured the depletion force between a silica colloidal particle ($R = 3.8\,\mu m$) and a silica plate, both covered with octadecyl alcohol (SiO_2–C_{18}). The Van der Waals force is minimized by performing the experiment in a solution of polydimethyl siloxane in cyclohexane. The curves show a short-range steric repulsion ($D = 3$–4 nm) followed by a strong attractive force, beginning at 20 nm of separation. The experimental data are in good agreement with Eq. (6.97).

Milling and Vincent [227] have studied the depletion force between silica surfaces in solutions of polyacrilic acid (PAA). The depletion force depends on the PAA concentration. In particular, the surface separation at which the depletion force reaches its maximum decreases with increasing PAA concentration. Also the effect of electrolytes ($NaNO_3$ and NaOH) is studied. The data are fitted with Eq. (6.97).

7. Imaging based on force–distance curves

Force–distance curves also may be acquired in all points throughout the scanned area in order to compare tip–sample interactions at different regions of the sample, i.e., in order to study the spatial variation of interactions.

In such a case, different scanning methods are employed and the quantities of interest (e.g., adhesion force) are drawn from the acquired curves and represented in two-dimensional maps. There are some common drawbacks of these imaging techniques. The acquisition of the force–distance curves on each point of the scanned surface can require some minutes, and almost all the information on the sample physico-chemical properties is drawn from maps obtained by data post-processing. An advantage of the use of force curves is the possibility of doing the lateral movement with the tip away from the surface, and hence the capability to avoid the dragging of the sample.

Two methods of acquisition are commonly used. In one method [228] force–displacement curves are acquired, irrespectively of sample topography, over a given distance range ΔZ beginning from a fixed

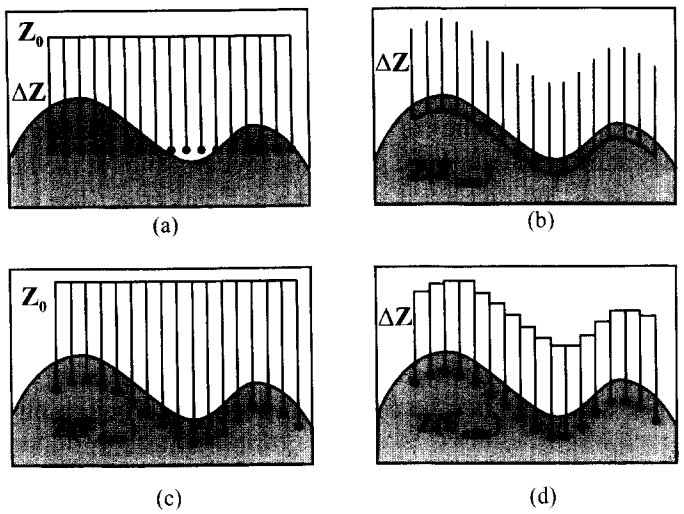

Fig. 34. The four main scanning methods proposed for the sequential acquisition of force–displacement curves on a surface, i.e. Radmacher's method (panel (a)), Baselt and Baldeschwieler method (panel (b)), Koleske et al. method (panel (c)), and Cappella et al. method (panel (d)). In Radmacher's method force–distance curves are acquired, irrespectively of sample topography, over a given distance range ΔZ beginning from a fixed distance at Z_0. In the other three methods, force–distance curves are acquired beginning from a point of maximum load $Z(F_{max})$. In the method of Baselt and Baldeschwieler the tip moves laterally in contact with the sample surface. The sampled distance ΔZ is fixed. In the method of Koleske et al. the height at which the tip is retracted is the same for all the points, so that the sampled distance varies for each curve. In Cappella et al. method the scanned volume follows the sample surface.

distance at Z_0 (panel (a), Fig. 34). The scanned volume does not follow the sample surface and there is no control on forces exerted on the cantilever by the sample. Therefore, the cantilever may bend excessively and break on protrusions or fail to contact the surface on depressions. With another method [229–231], force–displacement curves are acquired beginning from a point of maximum load $Z(F_{max})$. Thus the tip does not fail to contact the surface at each point and cantilever damage because of excessive load cannot occur. This method provides another advantage in that all force–displacement curves are related to the same value of force and can be compared directly. After Baselt and Baldeschwieler, the former method is referred to as "absolute mode" and the latter as "relative mode". In the relative mode different techniques are used to control the force on the cantilever so that it does not exceed the maximum load.

In Baselt and Baldeschwieler's work [229] a controller based on a digital signal processor is used and the tip moves laterally in contact with the sample surface. During this process the feedback loop is active and keeps the cantilever deflection, and hence the tip–sample force, constant. Then, at each point, the feedback is stopped and the tip is first withdrawn and then approached step by step. At each step the deflection is measured and stored. The sampled distance ΔZ is fixed, during both the withdrawal and the approaching ramp, as indicated in panel (b) of Fig. 34. In this technique part of the advantage of the force–distance curves method is lost because the tip is moved while it is in contact with the sample and so there is the risk of dragging the sample.

In the method of Koleske et al. [230] the computer stops the approach when the force reaches the maximum load and then the sample is retracted to a given height (see panel (c) in Fig. 34). This height

is the same for all the points so that the sampled distance varies for each curve. Therefore some acquisition time is wasted in sampling points too far from the surface, where there is no interaction.

Yet another method has been proposed by Cappella et al. [231], as illustrated in panel (d) of Fig. 34. At the beginning the tip is away from the surface. Then the sample is approached to the cantilever, acquiring deflection values at each pre-assigned step. This process stops at the height $Z(F_{max})$, when the force exerted on the tip reaches the pre-assigned maximum load F_{max}. The deflections in the last N_z approaching points are stored. Next the sample is retracted step by step for a distance ΔZ and the deflections in the next N_z withdrawal points are acquired and stored. After the acquisition of these N_z values, the sample is withdrawn for a further short distance in order to insure that the vertical distance between the cantilever and the subsequent XY point is never less than ΔZ. In this method lateral XY movements are done away from the surface, avoiding sample dragging. The scanned volume follows the sample surface so that no time is spent in acquiring points too far away from the surface.

The spatial variation of surface interactions may be represented in several ways. One of the most effective of these is constructed by plotting all the curves of one scanned line together. Even if the details of the interactions are sometimes lost, this kind of plot has the advantage of immediately comparing all the regions of the curve. Hence, differences in elasticity, attractive forces, and adhesion forces are simultaneously observable. A more refined analysis of the spatial variation of interactions can be performed by extracting several different parameters from the curves. Single parameters can be plotted on a gray scale as a function of the XY coordinates. In some works, such quantities, e.g., adhesion force, are directly acquired. Finally, a kind of image proposed by Cappella et al., namely the force-slice, has the advantage of showing the differences between different regions of the sample on line, i.e., during the acquisition and not in post-processing images.

7.1. Comparative curve plotting

A collection of withdrawal force–displacement curves acquired on a peroxidase deposit on silicon is showed in Fig. 35 [231]. All the curves belong to a scanning line. The peroxidase occupies the center of the scanned area. The curves are acquired in deionized water with an Si_3N_4 tip. The first and last curves of the scan line are on clean silicon. These curves have a jump-off-contact of approximately 3 nN. The adhesion on the peroxidase region (central curves) is smaller, allowing the two regions to be distinguished. Similar images have been obtained for a deposit of fluorescein iso-thiocianate (FITC) on silicon in air [231]. In this case, the differences in adhesion are due to the different degree of hydrophobicity of the two materials.

Radmacher et al. [228] have studied the spatial variation of interactions for a thin nickel film evaporated onto mica, a glass slide partially covered with chromium, and lysozyme adsorbed on mica. All measurements are performed in water. In all the three cases, large differences between the different regions of the sample are shown by plotting the curves of a scan line altogether. The presence of nickel islands on mica and of chromium regions on glass is revealed by higher attractive and adhesive forces, probably due to a hydrophobic meniscus exerted by contaminants adsorbed onto nickel or chromium. For the lysozyme, only the withdrawal curves show clear differences, since the adhesion is weaker on lysozyme than on mica.

Radmacher et al. [232] have mapped force–displacement curves on human platelets showing differences between the substrate and the cell mainly due to elasticity.

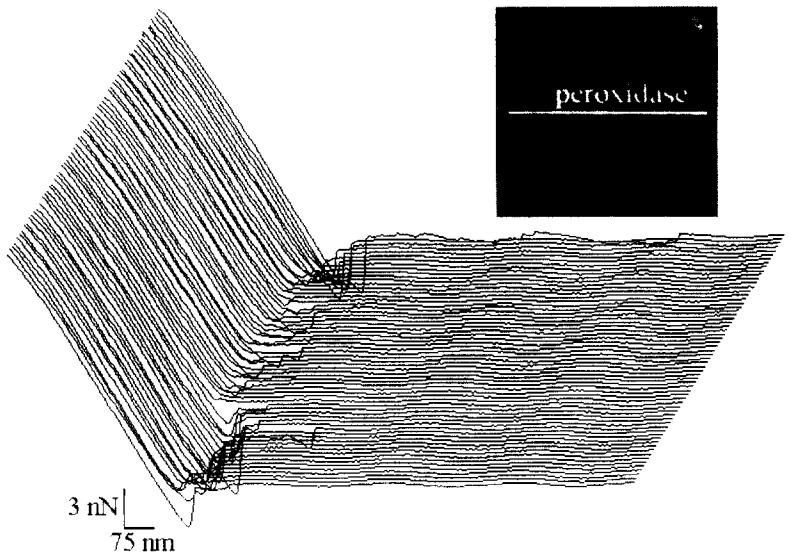

Fig. 35. Line of withdrawal force–displacement curves acquired on a peroxidase deposit on silicon. The inset is a lateral force image showing the area occupied by the peroxidase. The curves on silicon (first and last curves) have a rather large adhesion whereas the adhesion on the peroxidase region (central curves) is smaller, thereby allowing to be distinguished (adapted from [231]).

Rotsch and Radmacher [11] have studied the spatial variation of forces on a vesicle suspension of dimethyl dioctadecyl ammonium bromide (DODAB) on mica in pure water. Several kind of images are presented. The most effective images are the lines of force–displacement curves, in which all the regions of the curves can be immediately compared. In pure water, the DODAB is positively charged, while the mica is negatively charged. The silicon nitride tip is negatively charged. Hence the double-layer force is attractive between DODAB and silicon nitride and repulsive between mica and silicon nitride. Such a difference can be exploited to identify the DODAB vesicles in images collecting both the approach and the withdrawal force–distance curves. The lateral resolution is better than 25 nm.

7.2. Force-slices

A force-slice collects the deflections of the cantilever on each point of the scanned area at a given distance from the point of maximum load. The kind of information given by a force-slice depends on the considered distance. If the force-slice collects points on the contact line, then it provides information about the different stiffnesses of the regions of the sample. Force-slices collecting points near the jump-to-contact or the jump-off-contact give information about attractive or adhesive forces. Three force-slices at different distances from the deflection of maximum load (300, 350, and 440 nm) are shown in Fig. 36 for a sample of FITC on silicon. Two squares of FITC are partially evident. The lighter parts of the image indicate the larger value of deflection. In each of the three slice-forces, it is evident that the tip is still adhering to silicon, although it is already detached from the FITC deposit. Hence the points on silicon are black (negative deflections) and the points on FITC are white (zero deflection). The number of points on FITC at which the tip is already detached increases with the distance. Such differences in adhesion are due to capillary forces. Similar images have been presented for a deposit of

Fig. 36. Three force-slices at a distance of 300, 350, and 440 nm from the deflection of maximum load on a FITC deposit on silicon. The lighter parts of the image indicate the larger value of deflection. In each force-slice the tip is still adhering to silicon (black points), while it is already detached from the FITC deposit (white points). The number of points on FITC at which the tip is already detached increases with the distance (adapted from [231]).

peroxidase on silicon in water [228], where differences are mainly due to different Hamaker constants. Meaningful information can be drawn from force-slices only if they are acquired in a relative mode. Otherwise, the curves are not referred to the same maximal value of load and deflections cannot be compared.

Information obtained from force-slices is qualitative. A force-slice does not contain either the value of the pull-off force or the distance at which the tip pulls off the sample. It simply shows that, at a certain distance from sample surface, pull-off has already occurred in some regions of the scanned area, while in other regions it has still to occur.

7.3. Mapping parameters drawn from force–distance curves

Three maps obtained in air on a phosphatidyl choline (PC) deposit on silicon are shown in Fig. 37. The maps show the jump-off-contact force (panel (a)), the jump-off-contact distance (panel (b)), and the adhesion (panel (c)). The adhesion is calculated as the area below the zero line in the withdrawal

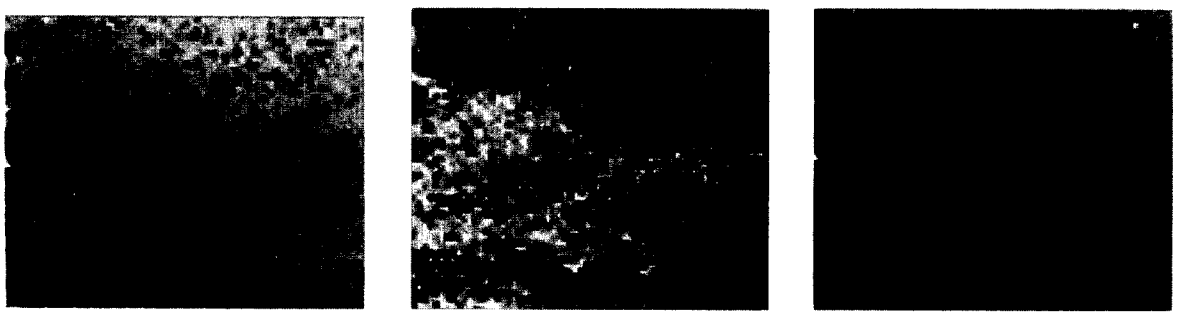

Fig. 37. Three maps obtained in air on a phosphatidilcoline deposit on silicon. The maps show the jump-off-contact (panel (a)), the jump-off-contact distance (panel (b)), and the adhesion (panel (c)).

curve. The PC regions show a smaller pull-off force (darker points), a smaller pull-off distance (lighter points) and a weaker adhesion (darker points). The different quantities are calculated off-line from the curves and mapped. Since curves are acquired in air, the differences between the two regions are due to differences in the thickness of the adsorbed water layer.

The first direct measurement showing the spatial dependence of adhesion is that of Mizes et al. [19]. These authors have performed adhesion studies on a sample of both doped and undoped polycarbonate in air. The adhesion is mainly due to meniscus force. First of all, the authors check that the adhesion is not affected by repeated contacts. Subsequently, they show that the adhesion depends on sample topography and on materials properties. As a matter of fact, three ridges are present on the sample. The adhesion is smaller on the edge of the ridges, since the contact area, and hence the meniscus force, is smaller. On the bottom of the ridge the adhesion is larger, since a larger portion of the tip is in contact with the sample surface, as indicated schematically in Fig. 38. Hence, adhesion maps are able to reveal differences in sample topography. Differences in sample materials can also be detected. The authors demonstrate the capability of adhesion maps to distinguish between doped and undoped polycarbonate. Since measurements are performed in air, the differences detected are probably differences in materials hydrophobicity.

Differences in materials hydrophobicity have been exploited also by Berger et al. [100]. These authors show adhesion maps acquired in air on a di-myristoyl-phosphatidyl-ethanolamine (DMPE) deposit. The thicker domains have a smaller adhesion.

The same kind of measurements has been performed by Sasaki et al. [233] on a Cr grating on glass. The authors show the topography dependence of adhesion and propose a method to draw pull-off and pull-on forces from the curves. Also pull-on maps are presented.

Dufrene et al. [234] have performed similar measurements on a mixed di-stearoyl-phosphatidyl-ethanol-amine (DSPE) and di-oleoyl-phosphatidyl-ethanol-amine (DOPE). Adhesion maps in air show that the microscopic domains of DSPE have a smaller adhesion (6.1 ± 0.2 nN) than the DOPE matrix

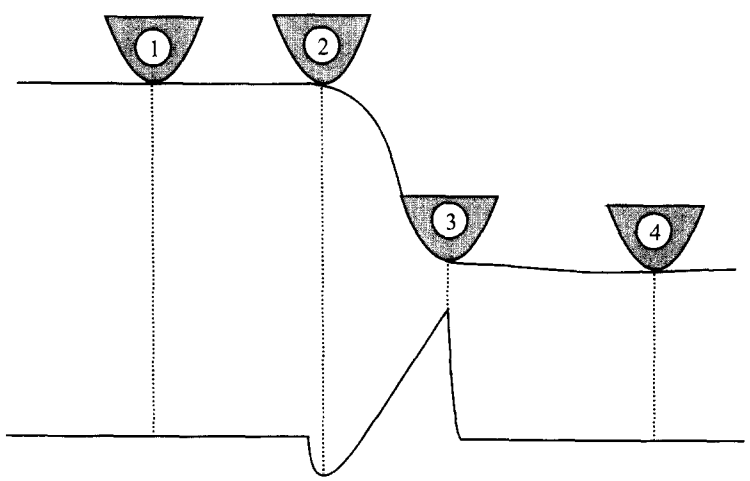

Fig. 38. Schematic representation of the dependence of the adhesion force on sample topography. The top line represents the sample and the tip in four different positions, the bottom line represents the corresponding adhesion. Various tip positions are indicated by the labels (1)–(4). In (2), a smaller fraction of the tip surface comes in contact with the sample surface than in (1) or in (4), whereas the contact area is larger in (3). The adhesion varies accordingly.

(10.5 ± 0.2 nN). Differences in adhesion are attributed to differences in materials elasticity and deformation. Adhesion maps also in water are presented. Once again the adhesion is larger on DOPE. The authors attribute such differences to the presence of repulsive hydration or steric forces acting only between DSPE and the Si_3N_4 tip.

Baselt and Baldeschwieler [229] have acquired force–displacement curves in air on collagen fibrils. These authors have used both the relative and the absolute mode of acquisition. Force-slices were considered too difficult to interpret. Hence, different parameters are drawn from the force curves and mapped. The authors have shown adhesion and hardness maps.

Koleske et al. [230] have shown maps of pull-on and pull-off force on a calibration grating in air.

Van der Werf et al. [125] have acquired on-line the pull-off force, the pull-off distance, and the adhesion on a mercaptopentadecane–gold layer on glass. The pull-off force is determined by means of a peak revelator. The pull-off distance and the adhesion are detected by means of two integrators. Several images of different samples obtained in air and in water are presented. The method proposed by the author presents some advantages when compared with usual mapping methods. However, it cannot be effectively used for every kind of sample and interaction.

Ishino et al. [235] have mapped forces on patterns of stearyl-mercaptan, stearic acid, stearyl alcohol, and stearylamine monolayers on SiO_2. All the patterns are well imaged in jump-in and jump-off maps. The stearyl-mercaptan is hydrophobic and uncharged in water at pH 5.6, whereas the silicon nitride tip and the bare silicon oxide surface are both negatively charged. In jump-in maps, forces on stearyl-mercaptan are about 1.5 nN greater than on SiO_2. The other three patterns are imaged in adhesion maps. In all the three cases, adhesion forces are greater on the monolayers than on the bare silicon oxide. Differences in attractive and adhesion forces are due mainly to the double-layer force (see also Ref. [12]).

7.4. Affinity imaging

The mapping of specific forces by means of functionalized tips has often been called "affinity imaging", since functionalized tips are able to single out the complementary molecule on a sample.

Hinterdorfer et al. [200] have localized single antigens on samples with a low density of molecules. These authors have performed a scanning of the sample along a given direction. In withdrawal curves, the specific detachments occur only at certain positions. A plot of the number of specific detachments vs. the position gives a gaussian distribution whose peak corresponds to the position of the molecule.

Ludwig et al. [236] have mapped the interaction between avidin and biotin. In their experiment, the tip is functionalized with biotin. The sample is a pattern of avidin lying between squares covered with bovine serum albumin (BSA). The authors show that the usual topographic images are not able to distinguish between the avidin and the BSA regions. On the contrary, the adhesion maps reveal the presence of avidin due to the different interactions. When free biotin is added in solution, the topographic image is always the same, but in the adhesion maps, the contrast disappears.

All the techniques designed to map surface forces have revealed the AFM as a useful tool for distinguishing different materials and for the imaging of materials that would be damaged by other imaging modes. Several technical problems are still unsolved, e.g., the long time needed for the acquisition. Nevertheless these new kinds of "surface spectroscopy" are very promising.

8. Synopsis

The AFM has been used to study surface forces and materials elasticity by means of force–distance curves since 1989. Since then, this technique has become a fundamental tool for several kinds of measurements.

In certain cases the technique gives satisfactory results and the interpretation of data no longer presents problems. Thus, AFM force–distance curves are the most used technique for measurements of the elasticity of materials, for the study of the wetting properties of lubricants, for the determination of the Hamaker constants in certain liquids, for the characterization of the double-layer force (determination of the Debye lengths, of the surface charges, and of the PZT of oxide-like materials), and for the study of solvation and hydrophobic forces. New applications are constantly being found. The technique is becoming increasingly reliable in the characterization of the degree of hydrophobicity, in the study of the adsorption of salts and polymer at liquid/solid or liquid/liquid interfaces, and in the characterization of steric and bridging forces.

The most promising results are the recent studies of forces at a liquid/liquid interface, the applications of functionalized tips for the study of specific forces and for the determination of single bond forces, and the development of techniques for the mapping of physico-chemical properties drawn from force–distance curves.

The main problems in the quantitative application of this technique are the uncertainties in the cantilever elastic constant and in the tip shape. Although procedures have been developed to calibrate the elastic constant of the cantilever, some cases, e.g., with functionalized tips, remain in which it is quite difficult to apply such techniques effectively. The main problem in AFM force–distance curve interpretation is, however, the lack of reliable methods to determine the tip shape and dimensions. The use of a big colloidal tip of known dimensions is not an effective solution to this problem, because one of the major advantages of the AFM, namely the capability of probing local interactions on a very little area, is lost. Only a better knowledge of the shape of the tip will increase the reliability of quantitative measurements of forces, above all the Van der Waals and the double-layer forces, and will permit the study of still uncharacterized forces such as hydrophobic or hydration forces.

Acknowledgements

We thank Dr. C. Ascoli for fruitful discussions and suggestions and Dr. N. Burnham for kindly providing several original figures.

We acknowledge Dr. C.B. Duke, Editor, for carefully proofreading and editing the manuscript and for suggesting a lot of corrections and improvements to our first draft. Despite his gigantic effort, this article remains imperfect.

List of acronyms

AFM	atomic force microscope
BSA	bovine serum albumin
cmc	critical micelle concentration
CTAB	hexadecyl trimethyl ammonium bromide

DDDA	didoeicosyl dimethyl ammonium
DEDA	dieicosyl dimethyl ammonium
DHDA	dihexadecyl dimethyl ammonium
DLVO	Derjaguin–Landau–Verwey–Overbeek
DMT	Derjaguin–Müller–Toporov theory
DODA	dioctadecyl dimethyl ammonium
DODAB	dimethyl dioctadecyl ammonium bromide
DMPE	dimyristoyl phosphatidyl ethanol amine
DOPE	dioleoyl phosphatidyl ethanol amine
DSPE	distearoyl phosphatidyl ethanol amine
EAM	embedded-atom method
EPS	extracellular polysaccharides
FEP	polytetrafluoroethylene-*co*-hexafluoropropylene
FITC	fluorescein iso-thiocianate
HMM	heavy meromyosin
HSA	human serum albumin
IEP	isoelectric point
JKR	Johnson–Kendall–Roberts theory
MD	molecular dynamics
OBP	odorant binding protein
OMCTS	octamethyl cyclotetrasiloxane
PAA	polyacrilic acid
PAN	polyacrilonitrile
PC	phosphatidyl choline
PDMS	polydimethylsiloxane
PEG	polyethylene glycol
PFD	perfluorodecalin
PFMCH	perfluoromethyl cyclohexane
PMMA	poly(methyl methacrylate)
PMN	lead magnesium niobate
PTFE	polytetrafluoroethylene
PVDF	polyvinylidene fluoride
PVP	polyvinyl pyrrolidone
PZC	point of zero charge
PZT	lead zirconate titanate
SDS	sodium dodecyl sulfate
SEM	scanning electron microscope
SFA	surface force apparatus
TEM	transmission electron microscope

List of symbols

a	contact radius
a_0	contact radius at zero load

A, B	coefficients of the attractive and repulsive Lennard-Jones terms
A	Hamaker constant
A_r	retarded Hamaker constant
A	amplitude of vibration
$\bar{A}$	dimensionless contact radius
α, α_{ij}	electronic polarizability
α_{exc}	excess polarizability
c	light speed
C	constant of the atom–atom pair potential
C_1, C_2	coefficients of the short- and long-range hydrophobic forces
C_K, C_D, C_L	Keesom, Debye, and London coefficients
γ	damping coefficient
γ_L	surface energy of liquids
γ_S	surface energy
γ_t, γ_s	tip and sample surface energies
d_{31}	proportionality factor between the voltage applied to the piezo and the displacement
ΔD, D	tip–sample distance
D_1, D_2	decay lengths of the short- and long-range hydrophobic forces
D_{jtc}	tip–sample distance at which the jump-to-contact occurs
$\Delta\delta_c$, δ_c	deflection of the cantilever
$(\delta_c)_{jtc}$	cantilever deflection at which the jump-to-contact occurs
δ, δ_s	sample deformation
$\bar{\delta}$	dimensionless deformation
e	electron charge
E	Young modulus
E	electric field
ε_0	vacuum dielectric constant
$\varepsilon, \varepsilon_i$	dielectric constant of the medium
f, F, ΔF	force
$F_0 \exp(i\omega t)$	exciting force exerted by the vibrating piezo
F_{ad}	adhesion force
F_{attr}	attractive force
F_∞^{sp}, F_0^{sp}	Coulomb force between a spherical tip and a flat sample at short and long distances
F^c	Coulomb force between a conical tip and a flat sample
$\bar{F}$	mean force
$\bar{F}$	dimensionless force
ϕ	phase
φ_P	Pashley parameter
φ_V	molecule volume fraction
g	gravitational acceleration
h	Planck constant
H	zero load elastic deformation

H'	zero load plastic indentation
H_r	relative humidity
k_B	Boltzmann constant
k_c	elastic constant of the cantilever
k_m	monomer elastic constant
K	reduced Young modulus
K_D	Debye length
l	monomer length
L	length of rectangular cantilevers
L_1, L_2	characteristic lengths of "V-shaped" cantilevers
L_p	length of the piezotube
λ	Maugis parameter
Λ	wavelength of the laser
m	mean number of bonds
m^*	effective mass of the cantilever
m_t	mass of the tip
M_w	molecular weight
μ	chemical potential
μ_M	Müller parameter
n, n_i	refractive index
n^*, n_i^*	low-frequency indices
n_m	number of monomers
N	number of polymer chains per unit area
ν	Poisson ratio
ν_e	absorption frequency
ν_i	ionization frequency
ν_n	frequency
ν_{rot}	average rotational relaxation frequency
P	pressure
Q_0, Q	quality factor of the cantilever
r	distance
R	tip radius
R_F	Flory radius
R_g	mean square radius of the polymer coil
R_m	molecular diameter
ρ, ρ_i	number density
S	order parameter
σ, σ_i	surface charge density
σ_A	Attard and Parker parameter
σ_F^2	variance
t	time
t_c	thickness of the cantilever
T	temperature
T_L	thickness of the polymer layer

θ_a, θ_r	advancing and receding contact angles
u_i	dipole moment
u_M	penetration depth in the liquid layer
U_c	Hooke's elastic potential of the cantilever
U_{cs}	tip–sample interaction potential
U_s	Hooke's elastic potential of the sample
U_{tot}	total tip–sample potential
v	vertical scan rate
$\Delta V, V$	voltage
V_m	molecular volume
w	width of rectangular cantilevers
w_p	wall thickness of the piezotube
w_K, w_D, w_L, w_{VdW}	Keesom, Debye, London, and total Van der Waals potentials
W	adhesion work at contact
W	width of V-shaped cantilevers
X	extension of the molecule
Ξ	persistence length
Σ	contour length
y	distance from the center of the contact circle
z	valence
$\Delta Z, Z$	distance between the sample surface and the rest position of the cantilever
ω_0, ω_0'	resonance frequency of the cantilever
Ω	proportionality factor between V and δ_c
ψ	electrostatic potential

References

[1] G. Binnig, C.F. Quate, Ch. Gerber, Phys. Rev. Lett. 56 (1986) 930.
[2] J. Akila, S.S. Wadhwa, Rev. Sci. Instrum. 66 (1995) 2517.
[3] J.E. Griffith, G.L. Miller, C.A. Green, D.A. Grigg, P.E. Russell, J. Vac. Sci. Technol. B 8 (1990) 2023.
[4] A.E. Holman, W.Ch. Heerens, F. Tuinstra, Sensors, Actuators 36 (1993) 37.
[5] E. Riis, H. Simonsen, T. Worm, U. Nielsen, F. Besenbacher, Appl. Phys. Lett. 54 (1989) 2530.
[6] S. Yoshida, Metrologia 28 (1992) 433.
[7] S.M. Hues, C.F. Draper, K.P. Lee, R.J. Colton, Rev. Sci. Instrum. 65 (1994) 1561.
[8] C.V. Newcomb, I. Flinn, Electron. Lett. 18 (1982) 443.
[9] H. Kaizuka, B. Siu, Jpn. J. Appl. Phys. 27 (1987) 2773.
[10] H. Kaizuka, Rev. Sci. Instrum. 60 (1989) 3119.
[11] Ch. Rotsch, M. Radmacher, Langmuir 13 (1997) 2825.
[12] T. Aoki, M. Hiroshima, K. Kitamura, M. Tokunaga, T. Yanagida, Ultramicroscopy 70 (1997) 45.
[13] V.S.J. Craig, Colloids and Surfaces A 129–130 (1997) 75.
[14] P.M. Claesson, T. Ederth, V. Bergeron, M.W. Rutland, Adv. Colloid Interface Sci. 67 (1996) 119.
[15] J.N. Israelachvili, Intermolecular and Surface Forces, Academic Press, London, 1992.
[16] J.L. Parker, Langmuir 8 (1992) 551.
[17] W.A. Ducker, T.J. Senden, R.M. Pashley, Langmuir 8 (1992) 1831.
[18] E. Meyer, H. Heinzelmann, P. Grütter, Th. Jung, Th. Weisskopf, H.-R. Hidber, R. Lapka, H. Rudin, J. Güntherodt, J. Microscopy 152 (1988) 269.

[19] H.A. Mizes, K.-G. Loh, R.J.D. Miller, S.K. Ahuja, E.F. Grabowski, Appl. Phys. Lett. 59 (1991) 2901.
[20] E.-L. Florin, V.T. Moy, H.E. Gaub, Science 264 (1994) 415.
[21] H.W. Hao, A.M. Barò, J.J. Saenz, J. Vac. Sci. Technol. B 9 (1991) 1323.
[22] Y. Martin, C.C. Williams, H.K. Wickramasinghe, J. Appl. Phys. 61 (1987) 4723.
[23] P. Fontaine, P. Guenoun, J. Daillant, Rev. Sci. Instrum. 68 (1997) 4145.
[24] J.P. Aimé, Z. Elkaakour, C. Odin, T. Bouhacina, D. Michel, J. Curely, A. Dautant, J. Appl. Phys. 76 (1994) 754
[25] H. Hertz, J. Reine, Angew. Math. 92 (1881) 156.
[26] M. Heuberger, G. Dietler, L. Schlapbach, J. Vac. Sci. Technol. B 14 (1996) 1250.
[27] J.N. Sneddon, Int. J. Eng. Sci. 3 (1965) 47.
[28] R.S. Bradley, Phil. Mag. 13 (1932) 853.
[29] B.V. Derjaguin, V.M. Müller, Yu.P. Toporov, J. Colloid Interface Sci. 53 (1975) 314.
[30] K.L. Johnson, K. Kendall, A.D. Roberts, Proc. Roy. Soc. London A 324 (1971) 301.
[31] P. Attard, J.L. Parker, Phys. Rev. A 46 (1992) 7959.
[32] V.M. Müller, V.S. Yushchenko, B.V. Derjaguin, J. Colloid Interface Sci. 77 (1980) 91.
[33] M.D. Pashley, J.B. Pethica, D. Tabor, Wear 100 (1984) 7.
[34] D. Maugis, J. Colloid Interface Sci. 150 (1992) 243.
[35] J.A. Greenwood, Proc. Roy Soc. London A 453 (1997) 1277.
[36] D.S. Dugdale, J. Mech. Phys. Solids 8 (1960) 100.
[37] K.L. Johnson, J.A. Greenwood, J. Colloid Interface Sci. 192 (1997) 326.
[38] M.A. Lantz, S.J. O'Shea, M.E. Welland, Phys. Rev. B 56 (1997) 15345.
[39] S.R. Cohen, Ultramicroscopy 42–44 (1992) 66.
[40] J.H. Hoh, A. Engel, Langmuir 9 (1993) 3310.
[41] G. Haugstad, W.L. Glaedfelter, Ultramicroscopy 54 (1994) 31.
[42] N.A. Burnham, R.J. Colton, J. Vac. Sci. Technol. A 7 (1989) 2096.
[43] S.R. Cohen, G. Neubauer, G.M. McClelland, J. Vac. Sci. Technol. A 8 (1990) 3449.
[44] G.S. Blackman, C.M. Mate, M.R. Philpott, Phys. Rev. Lett 65 (1990) 2270.
[45] R.C. Thomas, J.E. Houston, T.A. Michalske, R.M. Crooks, Science 259 (1993) 1883.
[46] A.L. Weisenhorn, M. Khorsandi, S. Kasas, V. Gotzos, H.-J. Butt, Nanotechnology 4 (1993) 106.
[47] N.J. Tao, S.M. Lindsay, S. Lees, Biophys. J. 63 (1992) 1165.
[48] M. Radmacher, M. Fritz, P.J. Cleveland, D.A. Walters, P.K. Hansma, Langmuir 10 (1994) 3809.
[49] M. Radmacher, M. Fritz, P.K. Hansma, Biophys. J. 69 (1995) 264.
[50] J. Domke, M. Radmacher, Langmuir 14 (1998) 3320.
[51] D. Ricci, M. Grattarola, J. Microscopy 176 (1994) 254.
[52] D. DeVecchio, B. Bhushan, Rev. Sci. Instrum. 68 (1997) 4498.
[53] D.H. Gracias, G.A. Somorjai, Macromolecules 31 (1998) 1269.
[54] J.B. Pethica, A.P. Sutton, J. Vac. Sci. Technol. A 6 (1988) 2400.
[55] U. Landman, W.D. Luedtke, N.A. Burnham, R.J. Colton, Science 248 (1990) 454.
[56] S.M. Foiles, M.I. Baskes, M.S. Daw, Phys. Rev. B. 33 (1986) 7893.
[57] A.L. Weisenhorn, P.K. Hansma, T.R. Albrecht, C.F. Quate, Appl. Phys. Lett. 54 (1989) 2651.
[58] R.M. Lynden-Bell, Science 263 (1994) 1704.
[59] N. Agraït, G. Rubio, S. Vieira, Phys. Rev. Lett. 74 (1995) 3995.
[60] C.A. Stafford, D. Baeriswyl, J. Bürki, Phys. Rev. Lett. 79 (1997) 2863.
[61] A.L. Weisenhorn, P. Maivald, H.-J. Butt, P.K. Hansma, Phys. Rev. B 45 (1992) 11226.
[62] G. Toikka, R.A. Hayes, J. Ralston, Langmuir 12 (1996) 3783.
[63] B. Gauthier-Manuel, Europhys. Lett. 17 (1992) 195.
[64] S.P. Jarvis, H. Yamada, S.-I. Yamamoto, H. Tokumoto, J.B. Pethica, Nature 384 (1996) 247.
[65] S.-I. Yamamoto, H. Yamada, H. Tokumoto, Rev. Sci. Instrum. 71 (1997) 3492.
[66] S.A. Joyce, J.E. Houston, Rev. Sci. Instrum. 62 (1991) 710.
[67] P.J. Bryant, H.S. Kim, R.H. Deeken, Y.C. Cheng, J. Vac. Sci. Technol. A 8 (1990) 3502.
[68] P. Siedle, H.-J. Butt, Langmuir 11 (1995) 1065.
[69] C.J. Drummond, T.J. Senden, Colloids and Surfaces A 87 (1994) 217.
[70] M. Tortonese, IEEE Eng. Med. Biol. 16 (1997) 28.

[71] T.R. Albrecht, S. Akamine, T.E. Carver, C.F. Quate, J. Vac. Sci. Technol. A 8 (1990) 3386.
[72] J.E. Sader, Rev. Sci. Instrum. 66 (1995) 4583.
[73] J.E. Sader, L. White, J. Appl. Phys. 74 (1993) 1.
[74] J.M. Neumeister, W.A. Ducker, Rev. Sci. Instrum. 65 (1994) 2527.
[75] K.E. Petersen, C.R. Guarnieri, J. Appl. Phys. 50 (1979) 6761.
[76] J.P. Cleveland, S. Manne, D. Bocek, P.K. Hansma, Rev. Sci. Instrum. 64 (1993) 403.
[77] T.J. Senden, W.A. Ducker, Langmuir 10 (1994) 1003.
[78] J.L. Hutter, J. Bechhoefer, Rev. Sci. Instrum. 64 (1993) 1868.
[79] Ya.I. Rabinovich, R.-H. Yoon, Langmuir 10 (1994) 1903.
[80] Ya.I. Rabinovich, R.-H. Yoon, Colloids and Surfaces A 93 (1994) 263.
[81] J.E. Sader, I. Larson, P. Mulvaney, L.R. White, Rev. Sci. Instrum. 66 (1995) 3789.
[82] J.A. DeRose, J.P. Revel, Micr. & Microanal. 3 (1997) 203.
[83] J.E. Griffith, D.A. Grigg, M.J. Vasile, P.E. Russell, E.A. Fitzgerald, J. Vac. Sci. Technol. A 10 (1992) 674.
[84] Y. Umehara, Y. Ogiso, K. Chihara, K. Mukasa, P.E. Russell, Rev. Sci. Instrum. 66 (1995) 269.
[85] P. Nagy, G.I. Márk, E. Balázs, Mikrochim. Acta 13 (1996) 425.
[86] P.M. Williams, K.M. Shakesheff, M.C. Davies, D.E. Jackson, C.J. Roberts, S.J.B. Tendler, J. Vac. Sci. Technol. B 14 (1996) 1557.
[87] S. Dongmo, M. Troyon, P. Vautrot, E. Delain, N. Bonnet, J. Vac. Sci. Technol. B 14 (1996) 1552.
[88] J.S. Villarrubia, J. Vac. Sci. Technol. B 14 (1996) 1518.
[89] J.S. Villarrubia, J. Res. Natl. Inst. Stand. Technol. 102 (1997) 425.
[90] M.W. Rutland, T.J. Senden, Langmuir 9 (1993) 412.
[91] I. Larson, C.J. Drummond, D.Y.C. Chan, F. Grieser, J. Am. Chem. Soc. 115 (1993) 11885.
[92] D.T. Atkins, R.M. Pashley, Langmuir 9 (1993) 2232.
[93] S. Biggs, P. Mulvaney, C.F. Zukovski, F. Grieser, J. Am. Chem. Soc. 116 (1994) 9150.
[94] Y.Q. Li, N.J. Tao, J. Pan, A.A. Garcia, S.M. Lindsay, Langmuir 9 (1993) 637.
[95] J.L. Hutter, J. Bechhoefer, J. Vac Sci. Technol. B 12 (1994) 2251.
[96] C. Gao, Appl. Phys. Lett. 71 (1997) 1801.
[97] C.M. Mate, M.R. Lorenz, V.J. Novotny, J. Chem. Phys. 90 (1989) 7550.
[98] T. Thundat, X.-Y. Zheng, G.Y. Chen, R.J. Warmack, Surf. Sci. Lett. 294 (1993) L939.
[99] T. Thundat, X.-Y. Zheng, G.Y. Chen, S.L. Sharp, R.J. Warmack, L.J. Schowalter, Appl. Phys. Lett. 63 (1993) 2150.
[100] C.E.H. Berger, K.O. van der Werf, R.P.H. Kooyman, B.G. de Grooth, J. Greve, Langmuir 11 (1995) 4188.
[101] A. Torii, M. Sasaki, K. Hane, S. Okuma, Sensors, Actuators A 40 (1994) 71.
[102] L. Xu, A. Lio, J. Hu, D.F. Ogletree, M. Salmeron, J. Phys. Chem. B 102 (1998) 540.
[103] L. Xu, M. Salmeron, Langmuir 14 (1998) 2187.
[104] T. Eastman, D.-M. Zhu, Langmuir 12 (1996) 2859.
[105] M. Fujihira, D. Aoki, Y. Okabe, H. Takano, H. Hokari, J. Frommer, Y. Nagatani, F. Sakai, Chem. Lett. 7 (1996) 499.
[106] M. Binggeli, C.M. Mate, Appl. Phys. Lett. 65 (1994) 415.
[107] L. Olsson, P. Tengvall, R. Wigren, R. Erlandsson, Ultramicroscopy 42–44 (1992) 73.
[108] M.C. Friedenberg, C.M. Mate, Langmuir 12 (1996) 6138.
[109] J. Colchero, A. Storch, M. Luna, J. Gomez Herrero, A.M. Baró, Langmuir 14 (1998) 2230.
[110] N.A. Burnham, R.J. Colton, H.M. Pollock, Phys. Rev. Lett. 69 (1992) 144.
[111] U. Hartmann, in: Theory of STM and Related Scanning Probe Methods, Springer, Berlin, 1993.
[112] L. Bergström, Adv. Colloid Interface Sci. 70 (1997) 125.
[113] D.B. Hough, L.R. White, Adv. Colloid Interface Sci. 14 (1980) 3.
[114] F. London, Trans. Faraday Soc., 33 (1937) 8.
[115] A.D. McLachlan, Proc. Roy. Soc. London Ser. A 202 (1963) 224.
[116] A.R. von Hippel, Dielectric Materials and Applications, Wiley, New York, 1958.
[117] B.W. Ninham, V.A. Parsegian, J. Chem. Phys. 52 (1970) 4578.
[118] L.D. Landau, E.M. Lifshitz, Electrodynamics of Continuous Media, Pergamon, Oxford, 1963.
[119] H.B.G. Casimir, Proc. Kon. Ned. Akad. Wetensch. 51 (1948) 753.
[120] B.V. Derjaguin, Kolloid Zeits. 69 (1934) 155.
[121] H.C. Hamaker, Physica 4 (1937) 1058.

[122] E.M. Lifshitz, Soviet Phys. JETP 2 (1956) 73.
[123] U. Hartmann, Phys. Rev. B 43 (1991) 2404.
[124] T.J. Senden, C.J. Drummond, Colloids and Surfaces A 94 (1995) 29.
[125] N.A. Burnham, D.D. Dominguez, R.L. Mowery, R.J. Colton, Phys. Rev. Lett. 64 (1990) 1931.
[126] K. van der Werf, C. Putman, B.G. de Grooth, J. Greve, Appl. Phys. Lett. 65 (1994) 1195.
[127] T. Ishino, H. Hieda, K. Tanaka, N. Gemma, Jpn. J. Appl. Phys. 33 (1994) 4718.
[128] B. Cappella, P. Baschieri, C. Frediani, P. Miccoli, C. Ascoli, IEEE Eng. Med. Biol. 16 (1997) 58.
[129] U. Hartmann, Phys. Rev. B 43 (1991) 2404.
[130] A. Meurk, P.F. Luckham, L. Bergström, Langmuir 13 (1997) 3896.
[131] A. Milling, P. Mulvaney, I. Larson, J. Colloid Interface Sci. 180 (1996) 460.
[132] K. Feldman, T. Tervoort, P. Smith, N.D. Spencer, Langmuir 14 (1998) 372.
[133] P. Mulvaney, J.M. Perera, S. Biggs, F. Grieser, G.W. Stevens, J. Colloid Interface Sci. 183 (1996) 614.
[134] M. Bordag, G.L. Klimchitskaya, V.M. Mostepanenko, Surf. Sci. 328 (1995) 129.
[135] V.A. Parsegian, D. Gingell, Biophys. J. 12 (1972) 1192.
[136] H.-J. Butt, Biophys. J. 60 (1991) 777.
[137] X.-Y. Lin, F. Creuzet, H. Arribart, J. Phys. Chem. 97 (1993) 7272.
[138] H.-J. Butt, Biophys. J. 60 (1991) 1438.
[139] L. Meagher, J. Colloid Interface Sci. 152 (1992) 293.
[140] P. Kékicheff, S. Marcelja, T.J. Senden, V.E. Shubin, J. Chem. Phys. 99 (1993) 6098.
[141] R. Raiteri, S. Martinoia, M. Grattarola, Biosens. Bioelectron. 11 (1996) 363.
[142] M.E. Karaman, R.M. Pashley, T.D. Waite, S.J. Hatch, H. Bustamante, Colloids and Surfaces A 129–130 (1997) 239.
[143] T.J. Senden, C.J. Drummond, P. Kékicheff, Langmuir 10 (1994) 358.
[144] T. Arai, D. Aoki, Y. Okabe, M. Fujihira, Thin Solid Films 273 (1996) 322.
[145] G. Hüttl, D. Beyer, E. Müller, Surf. Interface Anal. 25 (1997) 543.
[146] K. Hu, F.-R.F. Fan, A.J. Bard, A.C. Hillier, J. Phys. Chem. 101 (1997) 8298.
[147] I. Larson, C.J. Drummond, D.Y.C. Chan, F. Grieser, J. Am. Chem. Soc. 99 (1995) 2114.
[148] P.G. Hartley, I. Larson, P.J. Scales, Langmuir 13 (1997) 2207.
[149] S.B. Johnson, C.J. Drummond, P.J. Scales, S. Nishimura, Colloids and Surfaces A 103 (1995) 195.
[150] H.-J. Butt, Biophys. J. 63 (1992) 578.
[151] D.T. Atkins, B.W. Ninham, Colloids and Surfaces A 129–130 (1997) 23.
[152] C.J. Drummond, Z.R. Vasic, N. Geddes, M.C. Jurich, R.C. Chatelier, T.R. Gengenbach, H.J. Griesser, Colloids and Surfaces A 129–130 (1997) 117.
[153] S. Biggs, M.K. Chow, C.F. Zukowski, F. Grieser, J. Colloid Interface Sci. 160 (1993) 511.
[154] V. Kane, P. Mulvaney, Langmuir 14 (1998) 3303.
[155] K. Hu, A.J. Bard, Langmuir 13 (1997) 5418.
[156] S. Manne, J.P. Cleveland, H.E. Gaub, G.D. Stucky, P.K. Hansma, Langmuir 10 (1994) 4409.
[157] I. Larson, D.Y.C. Chan, C.J. Drummond, F. Grieser, Langmuir 13 (1997) 2429.
[158] K. Hu, M. Brust, A.J. Bard, Chem. Mater. 10 (1998) 1160.
[159] R. Raiteri, M. Grattarola, H.-J. Butt, J. Phys. Chem. 100 (1996) 16700.
[160] R. Raiteri, M. Preuss, M. Grattarola, H.-J. Butt, Colloids and Surfaces A 136 (1998) 191.
[161] T. Ishino, H. Hieda, K. Tanaka, N. Gemma, Jpn. J. Appl. Phys. 33 (1994) L1552.
[162] A.C. Hillier, S. Kim, A.J. Bard, J. Phys. Chem. 100 (1996) 18808.
[163] T. Arai, M. Fujihira, J. Electroanal. Chem. 374 (1994) 269.
[164] J.E. Sader, S.L. Carnie, D.Y.C. Chan, J. Colloid Interface Sci. 171 (1995) 46.
[165] B.V. Derjaguin, L.D. Landau, Acta Physicochim. URSS 14 (1941) 633.
[166] E.J.W. Verwey, J.Th.G. Overbeek, Theory of Stability of Lyophobic Colloids, Elsevier, Amsterdam, 1948.
[167] F.F. Abraham, J. Chem. Phys. 68 (1978) 3713.
[168] M. Rao, B.J. Berne, J.K. Percus, M.H. Kalos, J. Chem. Phys. 71 (1979) 3802.
[169] S.J. O'Shea, M.E. Welland, J.B. Pethica, Chem. Phys. Lett. 223 (1994) 336.
[170] P.A. Kralchevsky, N.A. Denkov, Chem. Phys. Lett. 240 (1995) 385.
[171] L.D. Gelb, R.M. Lynden-Bell, Phys. Rev. B 49 (1994) 2058.
[172] D.L. Patrick, R.M. Lynden-Bell, Surf. Sci. 380 (1997) 224.

[173] S.J. O'Shea, M.E. Welland, T. Rayment, Appl. Phys. Lett. 60 (1992) 2356.
[174] J.H. Hoh, J.P. Cleveland, C.B. Prater, J.P. Revel, P.K. Hansma, J. Am. Chem. Soc. 114 (1992) 4917.
[175] J.P. Cleveland, T.E. Schäffer, P.K. Hansma, Phys. Rev. B 52 (1995) R8693.
[176] W.A. Ducker, T.J. Senden, R.M. Pashley, Nature 353 (1991) 239.
[177] B.V. Derjaguin, N.V. Churaev, J. Colloid Interface Sci. 49 (1974) 249.
[178] J.C. Eriksson, S. Ljunggren, P.M. Claesson, J. Chem. Soc., Faraday Trans. 2 (1989) 163.
[179] V.S. Yushchenko, V.V. Yaminsky, E.D. Shchukin, J. Colloid Interface Sci. 96 (1983) 307.
[180] E. Ruckenstein, N.V. Churaev, J. Colloid Interface Sci. 147 (1991) 535.
[181] R. Podgornik, J. Chem. Phys. 91 (1989) 5840.
[182] P. Attard, J. Phys. Chem. 93 (1989) 6441.
[183] R. Podgornik, V.A. Parsegian, J. Chem. Phys. 154 (1991) 477.
[184] Ya.I. Rabinovich, D. Guzonas, R.-H. Yoon, Langmuir 9 (1993) 1168.
[185] Y.-H. Tsao, D.F. Evans, H. Wennerstrom, Langmuir 9 (1993) 779.
[186] E. Kokkoli, C.F. Zukoski, Langmuir 14 (1998) 1189.
[187] Y.-H. Tsao, S.X. Yang, D.F. Evans, H. Wennerstrom, Langmuir 7 (1991) 3154.
[188] M. Mantel, Ya.I. Rabinovich, J.P. Wightman, R.-H. Yoon, J. Colloid Interface Sci. 170 (1995) 203.
[189] H.-J. Butt, J. Colloid Interface Sci. 166 (1994) 109.
[190] W.A. Ducker, Z. Xu, J.N. Israelachvili, Langmuir 10 (1994) 3279.
[191] V.M. Moy, E.-L. Florin, H.E. Gaub, Science 266 (1994) 257.
[192] G.U. Lee, D.A. Kidwell, R.J. Colton, Langmuir 10 (1994) 354.
[193] S. Allen, J. Davies, A.C. Dawkes, M.C. Davies, J.C. Edwards, M.C. Parker, C.J. Roberts, J. Sefton, S.J.B. Tendler, P.M. Williams, FEBS Lett. 390 (1996) 161.
[194] W.R. Bowen, N. Hilal, R.W. Lovitt, C.J. Wright, J. Colloid Interface Sci. 197 (1998) 348.
[195] G.U. Lee, L.A. Chrisey, R.J. Colton, Science 266 (1994) 771.
[196] T. Boland, B.D. Ratner, Proc. Natl. Acad. Sci. U.S.A. 92 (1995) 5297.
[197] A. Noy, D.V. Vezenov, J.F. Kayyem, T.J. Meade, C. Lieber, Chem. Biol. 4 (1997) 519.
[198] T. Nakagawa, K. Ogawa, T. Kurumizawa, S. Ozaki, Jpn. J. Appl. Phys. 32 (1993) L294.
[199] U. Dammer, M. Hegner, D. Anselmetti, P. Wagner, M. Dreier, W. Huber, H.-J. Guntherodt, Biophys. J. 70 (1996) 2437.
[200] P. Hinterdorfer, W. Baumgartner, H.J. Gruber, K. Schilcher, H. Schindler, Proc. Natl. Acad. Sci. U.S.A. 93 (1996) 3477.
[201] J.K. Stuart, V. Hlady, Langmuir 11 (1995) 1368.
[202] S. Allen, X.Y. Chen, J. Davies, M.C. Davies, A.C. Dawkes, J.C. Edwards, C.J. Roberts, J. Sefton, S.J.B. Tendler, P.M. Williams, Biochemistry 36 (1997) 7457.
[203] A. Vinckier, P. Gervasoni, F. Zaugg, U. Ziegler, P. Lindner, P. Groscurth, A. Pluckthun, G. Semenza, Biophys. J. 74 (1998) 3256.
[204] H. Nakajima, Y. Kunioka, K. Nakano, K. Shimizu, M. Seto, T. Ando, Biochem. Biophys. Res. Comm. 234 (1997) 178.
[205] U. Dammer, O. Popescu, P. Wagner, D. Anselmetti, H.-J. Guntherodt, G.N. Misevic, Science 267 (1995) 1173.
[206] J. Fritz, D. Anselmetti, J. Jarchow, X. Fernàndez-Busquets, J. Struct. Biol. 119 (1997) 165.
[207] C. Bustamante, J.F. Marko, E.D. Siggia, S. Smith, Science 265 (1994) 1599.
[208] H. Kikuchi, N. Yokoyama, T. Kajiyama, Chem. Lett. 11 (1997) 1107.
[209] W.R. Bowen, N. Hilal, R.W. Lovitt, C.J. Wright, Colloids, Surfaces A 136 (1998) 231.
[210] E.W. Van der Vegte, G. Hadziannou, Langmuir 13 (1997) 4357.
[211] J.M. Williams, T. Han, T.P. Beebe Jr., Langmuir 12 (1996) 1291.
[212] T. Han, J.M. Williams, T.P. Beebe Jr., Anal. Chim. Acta 307 (1995) 365.
[213] L.A. Wenzler, G.L. Moyes, G.N. Raikar, R.L. Hansen, J.M. Harris, T.P. Beebe Jr., Langmuir 13 (1997) 3761.
[214] L.A. Wenzler, G.L. Moyes, L.G. Olson, J.M. Harris, T.P. Beebe Jr., Langmuir 69 (1997) 2855.
[215] R.C. Thomas, J.E. Houston, R.M. Crooks, T. Kim, T.A. Michalske, J. Am. Chem. Soc. 117 (1995) 3830.
[216] E.W. Van der Vegte, G. Hadziannou, J. Phys. Chem. B 101 (1997) 9563.
[217] P.J. Flory, Statistical Mechanics of Chain Molecules, Wiley, New York, 1969.
[218] P.G. de Gennes, Adv. Colloid Interface Sci. 27 (1987) 189.
[219] G.J. Fleer, J.M.H.M. Scheutjens, B. Vincent, ACS Symp. Ser. 240 (1984) 245.
[220] S. Biggs, Langmuir 11 (1995) 156.
[221] B.P. Frank, G. Belfort, Langmuir 13 (1997) 6234.

[222] S. Biggs, A.D. Proud, Langmuir 13 (1997) 7202.
[223] G.J.C. Braithwaite, A. Howe, P.F. Luckham, Langmuir 12 (1996) 4224.
[224] W.A. Ducker, D.R. Clarke, Colloids and Surfaces A 94 (1994) 275.
[225] S. Biggs, J. Chem. Soc., Faraday Trans. 92 (1996) 2783.
[226] A.J. Milling, S. Biggs, J. Colloid Interface Sci. 170 (1995) 604.
[227] A.J. Milling, B. Vincent, J. Chem. Soc., Faraday Trans. 93 (1997) 3179.
[228] M. Radmacher, J.P. Cleveland, M. Fritz, H.G. Hansma, P.K. Hansma, Biophys. J. 66 (1994) 2154.
[229] D.R. Baselt, J.D. Baldeschwieler, J. Appl. Phys. 76 (1994) 33.
[230] D.D. Koleske, G.U. Lee, B.I. Gans, K.P. Lee, D.P. DiLella, K.J. Wahl, W.R. Barger, L.J. Whitman, R.J. Colton, Rev. Sci Instrum. 66 (1995) 4566.
[231] B. Cappella, P. Baschieri, C. Frediani, P. Miccoli, C. Ascoli, Nanotechnology 8 (1997) 82.
[232] M. Radmacher, M. Fritz, C.M. Kacher, J.P. Cleveland, P.K. Hansma, Biophys. J. 70 (1995) 556.
[233] M. Sasaki, K. Hane, S. Okuma, A. Torii, J. Vac. Sci. Technol. B 13 (1995) 350.
[234] Y.F. Dufrene, W.R. Barger, J.-B.D. Green, G.U. Lee, Langmuir 13 (1997) 4779.
[235] T. Ishino, H. Hieda, K. Tanaka, N. Gemma, J. Electroanal. Chem. 438 (1997) 225.
[236] M. Ludwig, W. Dettmann, H.-J. Gaub, Biophys. J. 72 (1997) 445.